5-1-2008

Effects of ionizing radiation on nanomaterials and III-V semiconductor devices.

Cory Cress

EFFECTS OF IONIZING RADIATION ON NANOMATERIALS AND III-V SEMICONDUCTOR DEVICES

by

CORY D. CRESS

A DISSERTATION

Submitted in partial fulfillment of the requirements
For the degree of Doctor of Philosophy
in
Microsystems Engineering
at the
Rochester Institute of Technology

May 2008

Author: _____
Microsystems Engineering Program

Certified by: _____
Ryne P. Raffaelle
Professor of Physics

Approved by: _____
Mustafa A.G. Abushagur
Director of Microsystems Engineering Program

Certified by: _____
Harvey J. Palmer
Dean Kate Gleason College of Engineering

NOTICE OF COPYRIGHT

REPRODUCTION PERMISSION STATEMENT

Permission Granted

TITLE:

"Effects of ionizing radiation on nanomaterials and III-V semiconductor devices."

I, *Cory D. Cress*, hereby grant permission to the Wallace Library of the Rochester Institute of Technology to reproduce my dissertation in whole or in part. Any reproduction will not be for commercial use or profit.

Signature of Author: _____ Date: _____

Effects of ionizing radiation on nanomaterials and III-V semiconductor devices

By

Cory D. Cress

Submitted by (Cory D. Cress) in partial fulfillment of the requirements for the degree of Doctor of Philosophy in Microsystems Engineering and accepted on behalf of the Rochester Institute of Technology by the dissertation committee.

We, the undersigned members of the Faculty of the Rochester Institute of Technology, certify that we have advised and/or supervised the candidate on the work described in this dissertation. We further certify that we have reviewed the dissertation manuscript and approve it in partial fulfillment of the requirements of the degree of Doctor of Philosophy in Microsystems Engineering.

Approved by:

Dr. Ryne Raffaelle _____
(Committee Chair and Dissertation Advisor) Date

Dr. Lynn F. Fuller _____

Dr. James B. Taylor _____

Dr. Shanchieh Jay Yang _____

MICROSYSTEMS ENGINEERING PROGRAM
ROCHESTER INSTITUTE OF TECHNOLOGY

May 2008

ABSTRACT

Kate Gleason College of Engineering
Rochester Institute of Technology

Degree Doctor of Philosophy **Program** Microsystems Engineering

Name of Candidate Cory D. Cress

Title: Effects of ionizing radiation on nanomaterials and III-V semiconductor devices

Devices based on III-V semiconductors and nanomaterials are expected to be critical components of future microsystems as the demand for greater functionality, range of application, and robustness continue to increase. There currently is a need for small-scale power supplies which can be used to power microsystems thereby enabling autonomous functionalities. The use of III-V semiconductor-based solid state devices and nanomaterials to convert the radiant energy of a radioisotope source into electricity has been investigated as a viable option to fulfill this demand. The energy imparted to a material by incident alpha-particles, resulting in electron-hole pair formation and ionization, may be converted into usable electrical power by a radioisotope microbattery (RIMB). A model describing the spatially varying rate of ionizing energy deposited in an absorber material held in close proximity to an isotropic alpha-emitting radioisotope source has been developed. The alpha-particle energy deposition model (*ADEP*) allows the total energy exciting the RIMB devices to be calculated and thereby provides a means to determine the efficiency of the experimentally measured devices. Two RIMB designs are investigated including a direct conversion microbattery based on a *nipi*-diode structure and an indirect conversion microbattery employing radioluminescent nanophosphors.

The multi-functional nature of microsystems may best be exploited by deploying them in extreme environments, such as space, where a low power consumption, small volume, and superior functionality are required. Expanding microsystems into such environments requires a full understanding of the effects that ionizing radiation will have on the optoelectronic properties of the devices and the materials which they are composed of. Irradiating devices with an isotropic alpha-particle flux is a good method for simulating the radiation damage encountered by III-V devices or nanomaterials employed in space. The large mass of alpha particles, in comparison to beta particles, leads to higher momentum transfers in nuclear interactions corresponding to a larger displacement damage dose near the surface of a material for comparably lower fluences. The effects of such irradiation on the optoelectronic properties of III-V semiconductor devices and epitaxially grown InAs quantum dots arrays are investigated. A crystal binding model based on the Tersoff interatomic potentials is developed and used to explain the increased radiation tolerance observed in the InAs quantum dot material system.

Abstract Approval: Committee Chair _____

Program Director _____

Dean KGCOE _____

ACKNOWLEDGMENTS

I would like to thank my advisor Dr. Ryne Raffaelle, for providing me with such a great opportunity to conduct my dissertation research. From the modern facilities and instrumentation, to the breadth of research efforts I've had the opportunity to be exposed to, I truly believe I have had a first class research experience. These great opportunities have been afforded by his unrelenting enthusiasm in scientific research and his unsurpassed work ethic, two qualities I hope to emulate in the future.

I would also like to thank Dr. Brian Landi. As a colleague, Brian has helped me through the many trials and tribulations associated with research. He has helped to hone my research skills, and has provided me with great insight regarding publishing, presenting, and the ethics of scientific research. Socially, Brian has brought many things to my attention, like leadership skills, how to effectively influence others, and the bold and rich flavor of Excelsior 2004. It has been a pleasure to work with him over the past five years.

To my family, thank you for supporting me in all of my academic aspirations. My parents, David and Clarene Cress have been my biggest fans throughout my entire life. No issue has been too small for me to call home for advice, and no problem I've caused was too large for them to accept and forgive. Their belief in my abilities were expressed to me at an early age and instilled within me a desire to achieve greatness. The success that I've achieved until now is largely due this and to the freedom they've provided me in making my own decisions along the way. My enduring wife, Ania Cress has given the greatest support. Her patients during the past five years, for me to spend late nights in the laboratory or travel out of town, have been a blessing. Ania's strong values and sense of family have given me the necessary balance in my life and has helped me overcome many hard times. She makes me a better person and for that I am greatly indebted.

To the faculty and students of the NPRL and at the NASA Glen Research Center, I am grateful for the academic and social affairs in which we've interacted. To Dr. Sheila Bailey, thank you for serving as my technical advisor during my NASA Graduate Student Research Program Fellowship; I am very appreciative for the funding support which was provided. To Dr. John Andersen and Dr. Seth Hubbard, thank you for your willingness to answer my seemingly endless barrage of questions. I would like to thank Christopher Schauerman for accompanying me on many trips to the gym for the necessary stress-relieving games of racquetball or to the local fishing hole for a chance to enjoy the fresh air. I am very appreciative of my committee members: Dr. Shanchieh Jay Yang, Dr. Lynn Fuller, and Dr. James Taylor, and of the following people who interacted with me throughout my education either as a mentor or a colleague: Dr. Moses Sudit, Dr. Jacqueline Mozrall, Mr. David Wilt, Mr. Paul Stiebitz, Mr. Christopher Redino, Mr. Christopher Bailey, Dr. Herbert Ruff, and Mr. Chris Evans.

TABLE OF CONTENTS

LIST OF FIGURE CAPTIONS

LIST OF TABLE CAPTIONS

CHAPTER 1. INTRODUCTION

The accelerated development of microelectronics coupled with improved bulk and surface micromachining techniques have enabled the growth of economically feasible and highly functional microsystems [1]. Blanchard and Fabrycky define a system as "…a set of interrelated components working together toward some common objective or purpose" [2]. Therefore, a microsystem may be defined as a set of interrelated components *on the sub-millimeter* scale working together toward some common objective or purpose. Such "common objectives" may be accomplished, for example, by integrating one or many optical switches, pressure sensors, fluid valves, inertial sensors, etc., together with microprocessing and telemetry subcomponents [1, 3]. The net result is an integrated system with increased functionality and concomitant low power consumption, mass, and size.

To date, microsystems have been dominated by Si electronics and sensors; however, the integration of III-V based components could potentially extend the utility of microsystems to the expanding fields of high frequency communications along with a wide host of optoelectronic based technologies. For instance, the high electron mobility and velocity saturation limit in GaAs and InP have made them ideal for high-frequency and high-power satellite communications [4, 5]. III-V semiconductors are the basis of advanced multi-junction photovoltaics [6], which are the current standard for space power generation systems. Furthermore, III-V semiconductors are widely utilized in infrared sensing, light emitting diode, and lasing applications [7]. An additional class of materials which can expand the functionality of microsystems is nanomaterials. The novelty of these materials is their size dependent optical, electronic, magnetic, etc.,

properties, and the ability to functionally integrate them within existing III-V based devices.

The main applications requiring the advantages offered by microsystems are often associated with remote or harsh environments in which data cannot be easily extracted without extensive infrastructure. Remote locations including desert, oceanic, and mountainous regions can all be characterized as having constantly changing temperature, pressure, humidity, etc., which can effect the operation of microsystems. When employed in space satellite applications, the devices are repeatedly thermally cycled as the satellite moves into and out of eclipse. There are many terrestrial and space applications in which some or all of the microsystem's components are exposed to ionizing radiation. Ionizing radiation, including gamma rays and high-energy charged particles, can lead to failure in semiconductor-based electronic device due to rapid ionization events, or cause a slow continuous degradation in the performance of electronic devices resulting from trapped charges and a reduction in minority carrier lifetimes [8, 9].

The schematic in Figure 1.1a, is a simplified depiction of an atomic ionization process where an incident high energy particle loses energy through interactions with the electrons encountered while traversing through a material. This form of energy loss accounts for >99% of the energy loss of charged particles (*i.e.*, partially or fully ionized atoms) and likewise for electrons with energies < 0.5 MeV [10, 11]. These primary collisions create forward scattered electrons within the semiconductor, which subsequently participate in secondary collision events, and so on. This leads to a high concentration of excited electrons which can easily be acted upon by an external field. In

the case of transistors, the large field present can result in a dangerous current spike potentially leading to a damaging latch-up condition [9]. However, this process is not in all cases disadvantageous. In fact, it is the fundamental operating mechanism used in the detection of nuclear radiation from unstable elemental isotopes in gas-filled counters and semiconductor junctions; it is also the mechanism which allows smoke detectors to sense small amounts of smoke within the nearby environment [10, 12]. The ionization of atoms and generation of excited charge carriers is analogous to creating electron-hole pairs in a photovoltaic device excited by light. Therefore, with a properly designed semiconductor device structure, it is possible to capitalize on this form of radiant energy transfer and use it to generate power [13]. A better understanding of the interaction between ionizing radiation and nanomaterials or III-V devices will be critical to the development of novel materials and devices which can enhance the sensing or power generation efficiencies of today's technologies.

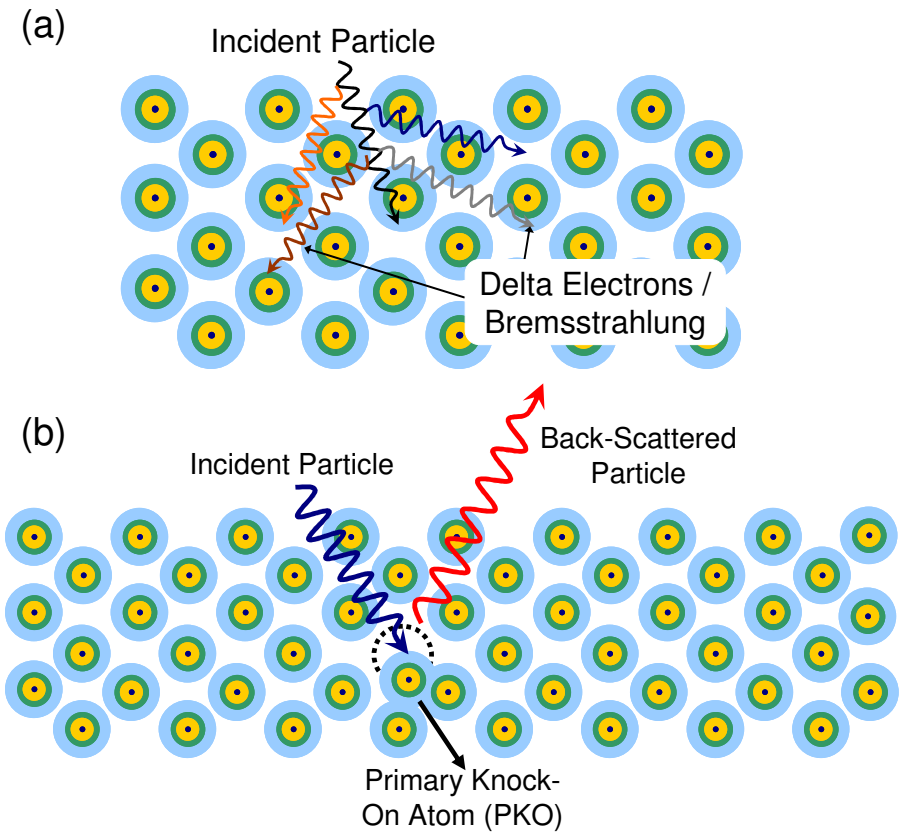

Figure 1.1 (a) Schematic depicting the loss of energy by an incident particle either through collisions with valence and core electrons or through Bremsstrahlung radiation which will be discussed in Chapter 2. (b) Schematic depicting the displacement of a lattice atom as a result of an incident particle collision. The trajectories of the Primary Knock-On (PKO) atom and the back-scattered particle are indicated.

The primary cause for the slow continuous degradation observed in the performance of semiconductor-based electronic devices is schematically depicted in Figure 1.1b. In this schematic, a high-energy particle is incident with, and transfers some or all of its energy to, a bonded atom within the semiconductor lattice causing it to become displaced. Following the collision, the primary knock-on (PKO) atom traverses the material, losing energy through electronic and nuclear collisions. Along the path of the PKO is a column of vacancies and near-by atoms occupying interstitial sites which disrupt the periodicity of the lattice. As a result, the behavior of the semiconductor device is affected, though only slightly, with each defect generated causing a slow

degradation in the device performance to be observed. Characteristic degradation equations, parameterized based on empirical data, are often used to describe the variation in the device performance with increasing defects [14-19]. Such equations have been shown to adequately describe the variation in III-V based photovoltaic devices under exposure to high-energy photon, electron, neutron, protons and other light charged particles. However, to better understand the degradation mechanisms, and to design new structures for reducing the rate of damage, a more fundamental investigation is necessary. Such information can then be utilized to increase the lifetime of microsystems employing III-V bulk and quantum confined semiconductors whether exposure is intentional, as in radioisotope power generation devices, or is an incidental result of the environment in which the system is utilized.

The organization of this dissertation is as follows, Chapter 2 contains background information on fundamental ionizing radiation – matter interactions and a historical review of solid state radioisotope batteries. Additionally, an overview of nanomaterials with an emphasis on epitaxially grown InAs quantum dots, and the use of these materials in GaAs solar cells is provided. To accomplish the goal of understanding the effects of ionizing radiation on nanomaterials and III-V semiconductor devices, a series of theoretical and experimental investigations have been conducted. The main experimental "tool" for this research is a ^{210}Po radioisotope source that emits ~ 5.4 MeV alpha particles. Such particles have a high rate of ionizing energy loss and are energetic enough to cause lattice dislocations. Theoretical models (referred to as *ADEP* and D^3P) are developed in Chapter 3 to understand how the alpha-particle flux emitted from an extended alpha-particle source spatially deposits both ionizing and non-ionizing (vacancy

generating) energy into a material. Also in Chapter 3 is an overview of a modeling approach developed to investigate the vacancy generation process in III-V semiconductors. This is accomplished by a molecular dynamics modeling approach for calculating the minimum energy necessary to create a lattice defect. Chapters 4-6 are applications of the theoretical and experiential results provided in the early chapters. Chapter 4 provides experimental validation for the *ADEP* modeling procedure and highlights the experimental and theoretical development of direct conversion radioisotope batteries. Chapter 5 pertains to the development of indirect conversion radioisotope batteries with an emphasis on the development of nanophosphor materials. In Chapter 6, the D^3P model and molecular dynamics model are utilized to investigate the effects of non-ionizing radiation on III-V-based solar cells in which nanomaterials are incorporated. Chapter 7 concludes this dissertation with a summary of the key findings and how they pertain to advancing the field of microsystems.

CHAPTER 2. BACKGROUND INFORMATION

2.1 RADIATION INTERACTIONS WITH MATTER

Radioactive isotopes, or radioisotopes for short, are elemental isotopes whose nuclei are unstable due to a lack or surplus of neutrons. This instability results in spontaneous nuclear decays which may be in the form of beta particles, alpha particles, or gamma rays. These decays are a primary source of radiation exposure for electronic devices employed in terrestrial applications. The rate at which a radioisotope decays is proportional to the number of radionuclides, N, present and the probability of decay, λ:

$$\frac{dN}{dt} = -\lambda N \,. \tag{2.1}$$

Using the activity, $A_o \equiv N_o \lambda$, where N_o is the initial number of radionuclides, the activity of a radioisotope sample as a function of time is given by:

$$A = A_o \exp(-\lambda t) \tag{2.2}$$

A commonly used unit of activity is the curie (Ci) which is equal to 37 billon decays per second. The parameter used to characterize the life time of a radioisotope is its half-life, $t_{1/2} = \ln(2)/\lambda$, which corresponds to the time it takes half of a given sample to decay.

A beta particle is a high energy electron created at the moment of neutron decay and emitted from the nucleus of the radioisotope. A portion of the energy lost in the neutron decay may also be imparted to a second subatomic particle called an antineutrino. Antineutrinos are neutral particles which weakly interact with matter and therefore their effect on matter is commonly ignored. The division of energy between the two particles causes beta-particles to be emitted with energies ranging over a continuous distribution

from nearly zero to a radionuclide-specific maximum energy. The maximum energy of a single beta particle emission equals the difference in rest energies between the parent and daughter atom ($E_{\beta,max} = m_p c^2 - m_d c^2 - m_e c^2$). In order to conserve momentum, most of this energy is imparted to the beta particle since its mass is much smaller than that of the nucleus. Obeying the law of conservation of electric charge the previously neutral neutron takes on a positive charge thereby forming a proton which leaves the daughter atom with an atomic number one greater than the parent. For some radioisotopes, the maximum energy of the emitted beta particle can exceed 1 MeV, however most maximum energy emissions are <500 keV.

An alpha particle is a high energy particle emitted from the nucleus of a radioisotope and consists of two protons and two neutrons (a double ionized helium atom). The energy of the emission is approximately equal to the rest energy of the parent atom minus the rest energies of both the daughter atom and the alpha particle. Again, most of this energy is imparted to the alpha particle because of the disparity in masses. As a result, the energy per alpha-particle decay for a given radioisotope is nearly constant; however, depending on the angular momentum of the emitted particle, different emission energies may result. The remaining energy is conserved by leaving the nucleus of the daughter atom in an excited energy state. An alpha decay results in a daughter atom which has an atomic number that is reduced by two and an atomic weight that is reduced by four. Most common alpha particle emissions energies range from 3 MeV to 7.5 MeV.

Gamma rays are nuclear emissions of high energy photons. These emissions do not result in a transmutation of the original atomic nucleus (they have zero mass) and can

occur spontaneously or in conjunction with beta and alpha radiation. Gamma rays result from energetic transitions of nuclei which have been left in an excited state after undergoing a radioactive decay, or as the result of a violent collision with another particle. They consist of extremely energetic emissions of electromagnetic radiation which can range from a few keV to hundreds of MeV.

An analysis of the interaction with matter for the different types of radioactive decay is necessary when considering each for power generation. Alpha and beta particles both carry charge and therefore interact Coulombically with the electrons and nuclei of the material traversed. The diameter of an atom is on the order of 10^{-10} m while the nuclear diameter is about 10^{-15} m. With 10^{15} times more volume occupied by electrons, elastic and inelastic electronic collisions with alpha and beta particles are much more probable making this the primary form of energy loss. Beta particles may also dissipate energy in the form of bremsstrahlung radiation which is the emission of light due to the (de-) acceleration of electrons in the electric field of the nucleus. The total rate of energy loss of the beta particle as it traverses matter is the sum of the Coulombic and radiative losses [13]:

$$\left(\frac{dE}{dx}\right) = \left(\frac{dE}{dx}\right)_{c} + \left(\frac{dE}{dx}\right)_{rad} \tag{2.3}$$

Accounting for relativistic velocities, the Coulombic and radiative energy loss portions can be modeled by [10]:

$$\left(\frac{dE}{dx}\right)_{c} = \left(\frac{e^2}{4\pi\varepsilon_0}\right)^2 \frac{2\pi Z N}{m c^2 \beta^2} \left[\begin{array}{l} \ln\left(\dfrac{T\left(T+mc^2\right)^2\beta^2}{2I^2 mc^2}\right) + \left(1-\beta^2\right) \\ -\left(2\sqrt{1-\beta^2}-1+\beta^2\right)\ln 2 + \dfrac{1}{8}\left(1-\sqrt{1-\beta^2}\right)^2 \end{array} \right] \tag{2.4}$$

and

$$\left(\frac{dE}{dx}\right)_{rad} = \left(\frac{e^2}{4\pi\varepsilon_0}\right)^2 \frac{Z^2 N\left(T + mc^2\right)}{137 mc^4}\left[4\ln\left(\frac{2\left(T + mc^2\right)}{mc^2}\right) - \frac{4}{3}\right] \tag{2.5}$$

where e is the electronic charge, Z is the atomic number of the absorber, N is the atomic density of the absorber, m is the electron rest mass, $v = \beta c$ is the velocity of the particle, c is the speed of light, T is the kinetic energy of the particle, I is the mean excitation energy of the atomic electrons, and ε_0 is the permittivity of free space. Equation (4) indicates that the rate of energy loss due to Coulombic interactions increases with decreasing particle velocity. It is also greater in materials with higher densities. The relative contributions of the two terms can be found by their ratios which is approximately:

$$\frac{\left(\frac{dE}{dx}\right)_{rad}}{\left(\frac{dE}{dx}\right)_{c}} = \frac{T + mc^2}{mc^2}\frac{Z}{1600} \tag{2.6}$$

This proportion shows that the radiative term is significant only at high energy and in heavy materials. In most semiconductor diodes (e.g., $Z \sim 28$ for $InGaP_2$) the radiative contribution is less than 2% for $T < 100$ keV.

A similar expression to (4) can be used to give the magnitude of the energy loss of alpha particles per unit length due to Coulombic interactions:

$$\left(\frac{dE}{dx}\right)_{c} = \left(\frac{e^2}{4\pi\varepsilon_0}\right)^2 \frac{4\pi z^2 Z N}{mc^2\beta^2}\left(\ln\left(\frac{2mc^2\beta^2}{I}\right) + \ln\left(1-\beta^2\right) - \beta^2\right) \tag{2.7}$$

where z is the charge on the alpha particle. Again, the rate of energy loss increases with decreasing particle velocity and for higher density materials. The last two terms account

for relativistic velocities and can be ignored for alpha particles with energies <10 MeV. For alpha-particles, the range of the particle can be found by integrating the inverse of the rate of energy loss with respect to the energy of the particle, and has been shown to provide similar results to those obtained experimentally. In contrast, the large degree of scattering for beta particles necessitates the use of an empirical relationship when determining their range in matter [10].

Gamma rays interact with matter primarily through three processes: photoelectric absorption, Compton scattering, and electron-positron pair production. In the photoelectric effect, an atom absorbs the gamma ray and an atomic electron (photoelectron) is released. The energy of the emitted photoelectron is equal to the kinetic energy of the gamma ray less the binding energy of the electron. The probability of photoelectric absorption is significant only for lower energy photons (<100 keV) and increases for materials with higher atomic numbers [10]. Compton scattering is the process by which a photon scatters from a nearly free electron resulting in a less energetic photon and a scattered electron that carries the energy lost by the photon. This process is more probable for lower energy photons and in materials which have greater free electron densities (e.g., Pb). In an electron-positron pair production process, the photon is annihilated causing all of its energy to be given to the two particles and its probability is significant for gamma rays with energies exceeding 5 MeV.

The total linear attenuation coefficient, μ, is used to describe the rate of photon (gamma ray) removal for a given thickness of material. The linear attenuation coefficient is simply the sum of the probabilities of photoelectron absorption, Compton scattering,

and pair production. Thus, the intensity of gamma rays after passing through an absorber with thickness, t, with an initial intensity, I_o, is:

$$\boldsymbol{I = I_o} \exp(-\boldsymbol{\mu t}) . \tag{2.8}$$

This equation is useful when determining the necessary shielding required to adequately attenuate the unwanted gamma rays associated with alpha- or beta-particle decay. The linear attenuation factors have been used to determine the specific gamma-ray dose constants for nearly all radionuclides by Oak Ridge National Laboratory [20].

The linear energy transfer of both alpha and beta particles is far greater than that of gamma particles thereby making the effective range of these particles much shorter. Additionally, the primary form of energy transfer of both alpha- and beta-particles is by electronic collisions thereby directly resulting in the formation of electron-hole pairs in semiconducting materials. The greater mass of the alpha particles, as compared to beta particles, and larger charge causes it to dissipate energy many times faster than beta particles. As a result, the maximum range in H_2O is approximately 50 μm for a 5 MeV alpha particle and it is approximately 2 cm for 5 MeV beta particles (200 μm for a 100 keV beta particle). Alpha-particles, therefore, are more attractive for power generation devices because less material is required to completely stop the particle. The long range and various modes of energy deposition make gamma particles the least attractive radioactive emission. However, it is still important to investigate the gamma emissions to ensure proper shielding is used.

2.2 SOLID STATE RADIOISOTOPE BATTERIES

Solid state radioisotope batteries are devices which utilize a semiconductor p/n junction to convert the radiant energy of a radioisotope into electricity. These devices may be categorized into two classes, a direct conversion radioisotope battery and an indirect conversion radioisotope battery. The former directly converts the kinetic energy of the sub-atomic particles emitted from a radioisotope into power in an analogous manner as that of a photovoltaic diode converting light into power. Indirect conversion devices make use of a two-stage energy conversion process whereby the radiant energy from the radioisotope is converted to light by a radioluminescent phosphor, the light from which is subsequently converted into electricity via a photovoltaic diode.

The concept of utilizing a solid state device to generate power dates back to 1951 when Ehrenberg *et al*. first demonstrated the so-called electron voltaic effect [21]. Also in that year, McKay *et al.*, reported the generation of electron hole pairs by alpha-particles [22]. In this report, a commonly used empirical formula was developed relating the energy required to create an electron hole pair E_{pair}, to that of the semiconductor bandgap E_g namely: $E_{pair} - E_g = 3 \pm 0.4$ [eV]. A second empirical result was also discussed in this report which was $E_{pair} = \sim 3E_g/2$ [eV], though this relationship was only valid in a few materials investigated.

There are three "efficiency" metrics which will be used to evaluate the performance of radioisotope batteries. The overall efficiency, $\eta_{tot} = P_e/P_n$ is referred to as the nuclear-to-electrical efficiency. This is a ratio between the electrical power output of the device P_e and the nuclear power emitted from the radioisotope source P_n. This corresponds to the overall efficiency of the battery. A second efficiency metric, which

will be the primary metric used to compare the different radioisotope batteries reported in the literature, is the semiconductor conversion efficiency $\eta_{semi} = P_e/P_{n,semi}$ which is the ratio of the output power to the nuclear power incident with the semiconductor device. This corrects η_{tot} to account for less-than-ideal coupling between the radiation source and the semiconductor device due to poor geometry matching. Poor geometry can be overcome by directly depositing the radioisotope source onto the semiconductor device; however, for conducting research it is more efficient to utilize a single radioisotope source, deposited onto a foil substrate, for measuring the efficiency of different devices and structures. The final efficiency metric η_x where $x = \alpha$ or β is similar to a quantum efficiency value and is defined as the ratio between the number of charge carriers extracted by the device and the total energy of the incident particle (in eV^{-1}).

The first betavoltaic battery study was performed by Rappaport [23], in 1954, and later that same year by Pfann and Van Roosbroeck [24] (see Figure 2.1). In both of these studies, sources comprised of ^{90}S - ^{90}Y were used to excite Si and Ge p/n junctions fabricated by thermal dopant diffusion. The wider bandgap, and correspondingly lower intrinsic carrier concentration and dark current, allowed the Si devices in both reports to generate nearly an order of magnitude more power than that of the Ge devices. The lower power output of the devices reported by Pfann *et al*., is due to a shield that was used to reduce the flux of high energy beta particles which had recently been shown to cause damage in Si and Ge semiconductor materials [23]. In 1965, the first alphavoltaic battery research was reported wherein an alpha-particle source was coupled to both Si and GaAs diodes [25]. At cryogenic temperatures, η_{semi} values of 2-3% were achieved, but at room temperature the efficiencies were well below 1%. In both devices, radiation

damage caused a significant drop in the power output, although the GaAs device withstood nearly an order or magnitude more fluence before degrading by the same extent [25].

A major breakthrough in betavoltaic technologies was the development of high purity promethium-147 radioisotope source. ^{147}Pm is a soft-beta emitter (β_{max} ~250 keV) and therefore is relatively benign to the semiconductor converters [26]. In 1964, Flicker *et al*. reported their 2-year study on a ^{147}Pm:Si betavoltaic battery which demonstrated a beginning-of-life power output of 9.1 μW/cm^2 and degraded with a half life only slightly shorter than that of the ^{147}Pm source itself ($t_{1/2}$ = 2.6 years for ^{147}Pm). It was suggested that trace amounts of ^{241}Am could have been present which emits 5.5 MeV alpha-particles. The η_{semi} for this device was 1.5% and it consisted of a 2π geometry and a total radioisotope source loading of 6.8 Ci. A 2π geometry means that only half of the radiant energy from the source is converted by the device; a 4π geometry utilizes the radiate energy emitted from both sides of a thin film radioisotope source material by sandwiching it between two semiconductors which are serially or parallelly connected depending on whether high voltage or high current is desired, respectively. A device with a 4π geometry was also tested by Flicker and co-workers but the performance suffered due to poor current matching through the serially connected stack and therefore had an efficiency of only 0.4% [26]. Barnes *et al.*, reported on a ^{147}Pm:Si betavoltaic battery with a 4π geometry which demonstrated a 10 μW/cm^2 peak power output with an η_{semi} of ~2% and a source loading of 4 Ci [27]. Olsen further improved upon this technology and demonstrated a promethium based betavoltaic battery which output 23 μW/cm^2 with an η_{semi} of ~2%[28]. This device was later tested as a potential long-life

battery to power implantable cardiac pacemakers. Many different radioisotope battery technologies, including direct conversion, direct charge, and thermoelectric devices, have been considered (and some have been tested) as long life pacemaker batteries; a good review of these technologies is provided by Huffman *et al*. in ref. [29].

Figure 2.1, referred to earlier, contains a timeline of the radioisotope devices reported in the literature since 1951. The rectangles indicate the semiconductor material, radioisotope source used, and the geometry of the device, *i.e.*, 2π vs. 4π. Down the center column is a chart depicting the power output (in log-scale) of the devices and the year in which they were reported. The markers on the chart are color coded to correspond with the device and the numbers on the marker indicate the reported (or calculated) η_{semi}. In most instances, the η_{semi} was not provided and was calculated based on the data provided in the manuscripts. Therefore, the power and efficiency values plotted in Figure 2.1 are accurate to ~15% relative (based on one's ability to extract data from graphs visually). There is a large gap in time, extending from the mid 1970s into the early 1990s, during which no reports on radioisotope batteries appear in the literature. Interestingly, the dates of the partial melt-down at the nuclear power generation station on Three Mile Island in Pennsylvania (1979) and the nuclear power generation station explosion in Chernobyl Ukraine (1986), the worst nuclear disaster in world history, occurred during this time period.

In the early 1990s the first demonstration of a radioluminescent light source coupled to a semiconductor diode was reported [30]. The novelty of this approach is the use of more radiation tolerance phosphor materials to serve as a shielding layer protecting the semiconductor diode from the radiation and converting the radiant energy of a

radioisotope source into light. In 1994 Sims *et al*., reported the results of simulated indirect conversion radioisotope devices using a GaP solar cell (E_g=2.26 eV) excited by a sealed ZnS:Ag / Tritium (^{3}H) light source [31]. The electron-to-light conversion efficiency of the phosphor was reported as 20.1% and the conversion efficiency of 6% was achieved by the GaP device under the low intensity ZnS:Ag light emission, which peaks at 450 nm. This device had good stability, but due to the low energy beta particles, self absorption was an issue limiting the power to 550 nW/cm^2.

In the mid 1990s Kosteski and co-workers reported their research on using ^{3}H to replace the H atoms typically used in amorphous Si to passivate the dangling Si bonds at grain boundaries [32]. Deus *et al.*, demonstrated an amorphous Si device with improved power output, and he, along with Andreev *et al.*, showed great improvements in power output, efficiency, and longevity, by employing a ^{3}H radioisotope source with a III-V semiconductor converter [33, 34]. The III-V device was comprised of AlGaAs, which is a wide bandgap material ranging between 1.4 eV – 2.2 eV depending on the concentration of Al. Deus's ^{3}H:AlGaAs device achieved a maximum power output of 259 nW/cm^2 with an efficiency of 2.3%. The device reported by Andreev *et al.* had comparable efficiencies under similar ^{3}H activity, though to increase the power output by a factor of 2 over that of device reported by Deus *et al.*, the ^{3}H loading had to be significantly increased. This large increase in loading was necessitated by the self shielding effects of the low energy beta particles emitted from ^{3}H. The AlGaAs material improved the efficiency greatly because the large bandgap increases the shunt resistance allowing for an open circuit voltage of ~0.9 V to be achieved with a generated current of 300 nA/cm^2 [34].

In 1996, Rybicki *et al.*, was the first to report on an alphavoltaic battery comprised of the newly developing SiC semiconductor material with a bandgap between 2.3-3.3 eV depending on the morphology. This device had a bandgap of 3 eV, generated 14 nW/cm^2 with a η_{semi} of 3.1% and η_{α} of 18% [35]. The low power output of the device was a consequence of the low activity ^{241}Am source; when tested at higher fluxes the increased power output was concomitant with a rapid rate of degradation. Fleurial *et al.* investigated an alphavoltaic battery employing ^{244}Cm and a GaAs diode. The device achieved a power output of 90 μW/cm^2 but this quickly degraded to 10 μW/cm^2 in only 10 minutes of operation [36]. In 2006, Cress *et al.*, demonstrated 50.6 nW/cm^2 with a 1 mCi ^{210}Po source coupled with an $InGaP_2$ p/n diode. The device had a η_{semi} of 3.2%, a η_{α} of 36% and had a half life of about 30 days [37]. This η_{α} value was consistent with the maximum monochromatic spectral responsivity measured for that device and was calculated using the *ADEP* modeling procedure which is discussed in Chapter 3 [38].

Increases in the efficiency were observed in betavoltaic devices employing soft beta particle sources, such as ^{3}H and ^{63}Ni, but suffer from self absorption because the energy of the emitted beta particles is insufficient for beta particles within the material to escape. Consequently, the maximum power output that can be achieved with these sources is severely limited. To mitigate these effects, novel techniques have been used to increase the active surface area of the semiconductor junction thereby maximizing the incident flux. Guo *et al*. fabricated inverted pyramids into a Si wafer and subsequently processed the wafer to form a p/n junction across the entire structured surface. The etching resulted in nearly a 2x increase in power output over that of a similar planar device, generating 1.14 nA/cm^2 with a η_{semi} of 0.36% under a 6.25 mCi/cm^2 ^{63}NiCl/HCl

liquid source solution [39]. With similar intentions, a 3D p/n diode fabricated from porous silicon was measured under ^{3}H irradiation [40]. This device only generated 0.17 nW/cm^2 with a η_{semi} of 0.2%; however, the ratio of the power generated within the pores to that of the power generated from the surface resulted in a 9x efficiency improvement.

In 2006, the use of soft-beta emitters, ^{63}Ni and ^{33}P used in conjunction with wide bandgap SiC diodes were investigated by Chandrashekhar, *et al.*[41], and Eiting, *et al.* [42], respectively. In the former, a SiC was excited by a 1 mCi ^{63}Ni source as well as by a scanning electron microscope (SEM) operated at ~17.5 kV (to simulate the average beta particle flux). This device is reported to have exceptionally high efficiency, η_{semi} = 6.3%, although the size of the device was only 2.5 mm^2. Moreover, the SEM-simulated beta particle flux will inflate the efficiency obtained because all of the electrons are normally incident with the diode and will stop very close to the surface. In a real betavoltaic, the higher energy betas (*i.e.*, E_{max} = 65 keV for ^{63}Ni) would penetrate much deeper into the device leading to less efficient conversion. The device reported by Eiting consisted of a SiC diode excited by a 225 mCi ^{33}P source which had very good efficiency, η_{semi} = 4.5%, and power output 2 μW/cm^2 however the ^{33}P has a half life of 25 days making this technology impractical.

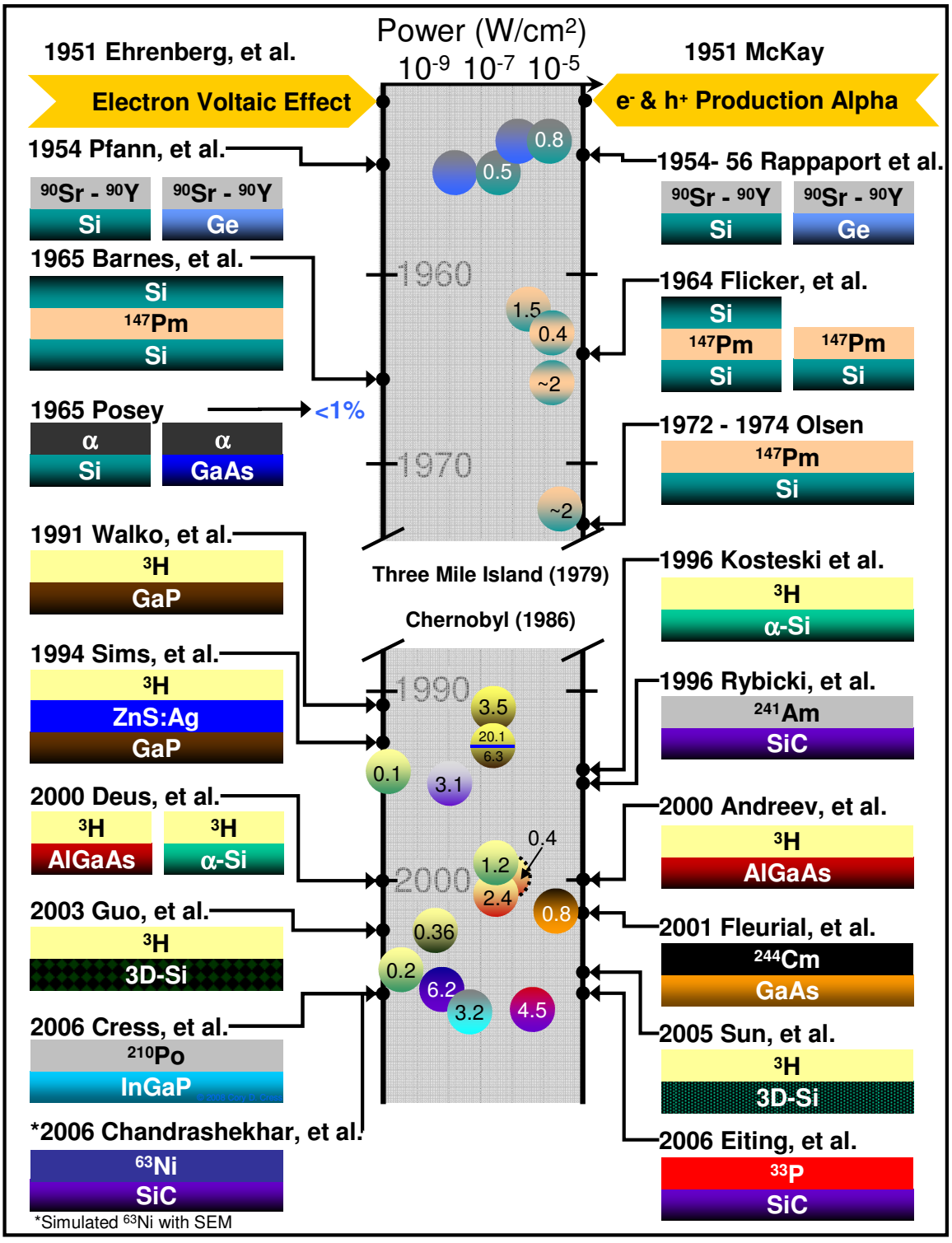

Figure 2.1. Timeline of radioisotope devices reported in the literature since 1951. The rectangles indicate the semiconductor material, radioisotope source used, and the geometry of the device, i.e., 2π vs. 4π. Down the center column is a chart (semi-log axes) depicting the power output of the device and the year in which it was reported. The markers on the chart are color coded to correspond with the device and the numbers on the marker indicate the reported (or calculated) η_{semi} of the device.

Based on this review of betavoltaic and alphavoltaic batteries, many conclusions may be drawn. The low current level of radioisotope batteries makes the shunt resistance the critical diode quality parameter, which is in contrast to photovoltaic applications where currents are high and therefore necessitate low series resistances. This in addition to low saturation currents and high diffusion lengths are the critical parameters for achieving high efficiencies at low levels of excitation. These requirements can all be met by using a wide bandgap semiconductor diode; the high efficiencies obtained by the AlGaAs, $InGaP_2$, and SiC devices provide experimental evidence supporting this conjecture (see Figure 2.1). Employing these materials in conjunction with 3-D device structures may prove effective at increasing the efficiencies further.

The choice of radioisotope is as important as the semiconductor diode utilized. The energy density, activity density, half life, emission energy, and decay type must all be considered. The transition from ^{90}Sr – ^{90}Y to the soft beta emitter, ^{147}Pm, had a profound effect on device performance including increased efficiency and lifetime. However this material is not favorable for long-term power supplies because the half life is only 2.6 years. ^{63}Ni and ^{3}H are both soft beta emitters (maximum beta particle energy is ~65 keV and ~19 keV, respectively), and have half lives in excess of 10 years. As observed in Figure 2.1, the low energy of these beta particles causes self absorption to become a problem. In fact the maximum power emitted per unit area of ^{3}H gas is 14 $\mu W/cm^2$ and only 0.21 $\mu W/cm^2$ from ^{63}Ni [13]. This is because the added material shields as many beta particles as it contributes. The modern devices employing alpha-particle irradiation all achieved good η_{semi} values because the alpha particles have a shorter range and deposit more energy near the junction of the devices. However, the

damage caused by alpha-particles is a major impediment. Based on simple conservation of momentum and energy arguments, the energy needed by an alpha-particle to cause a lattice displacement is about 4000 times less than that required by an electron [10]. To generate a defect in GaAs, a 225 keV beta-particle is needed [26]. This means that a 57 eV alpha-particle would have sufficient energy to generate defects in this material. Before alpha-particle emitters can be successfully utilized in direct conversion or indirect conversion radioisotope batteries, it is necessary for major developments in radiation-tolerant materials to be performed. However, the use of alpha-particle sources as an experimental tool is very useful for understanding the operation of novel device structures or materials, and to investigate the damaging effects of ionizing radiation.

2.3 NANOMATERIALS AND NANO-ENHANCED DEVICES

A nanomaterial can be broadly defined as a material which has at least one dimension that is measurable on the nanometer scale. With this broad definition, the components (*i.e.*, gate oxides, gate electrode, source-drain metal contacts, etc.,) comprised in integrated circuits from as far back as the 1990s could all be considered nanomaterials. However, there is nothing truly special with the materials used in these devices when compared with the properties of their corresponding bulk materials. Therefore, perhaps erroneously, the buzz words “nanomaterial” and “nanotechnology” imply that the size of these materials is the unique aspect of interest. In contrast, the interest in nanomaterials is based upon the unique and potentially tunable properties which can be obtained in certain materials when their size is reduced to the nanometer scale.

Generally speaking, unique properties that have been observed in nanomaterials include improved catalytic behavior, enhanced plasmonic absorption, increased or decreased optical absorption, enhanced magnetic properties, and the list goes on [43]. The existence of these unique properties may be attributed to several factors including [44]:

- The surface atom to interior atom ratio is on the order of one.
- The ratio of the surface energy to the total cohesive energy is on the order of one.
- The conduction and valence electrons are confined to small length or volume and therefore the minimum wavevector is longer than in the bulk.
- The observed increases in strength among nanometal clusters results from the difficulty to move dislocations in spatially confined regions.

Many of these properties are only observable at the nanometer scale and are not necessarily tunable. However, in III-V and other semiconductor systems, as the dimension of these materials becomes reduced, quantum size effects become apparent. In particular, the optical and electronic bandgap can be increased to many times the bulk bandgap depending on the fundamental materials properties and on the dimensionality of the size reduction. Such size dependent properties are typically referred to as quantum size effects and result from confinement of the electron motion within the lattice in one, two, or three dimensions.

Figure 2.2 is useful for illustrating the fundamental origination of quantum confinement (quantum size effects) in one, two, and three dimensions. On the left column of this figure are schematics depicting a bulk structure, a quantum well, quantum wires, and quantum dots. Each of these structures is made up of many atoms arranged in

a periodic crystalline lattice. The periodicity makes it useful to mathematically describe the lattice in reciprocal space thereby making Fourier analysis straightforward. Like the lattice, the propagation of an electron in the lattice can also be described in reciprocal space and is referred to as the wavevector $\vec{k} = 2\pi/\lambda$, where λ is the wavelength of the electron. This transformation results in possible $\vec{k}$ ranging from 0 to ~2π/*a*, where *a* is the lattice spacing, as opposed to using wavelengths which range from ~0 to infinity [44]. As the dimensionality of the semiconductor crystals is constricted, the set of allowable $\vec{k}$ become reduced, starting with a reduction in short $\vec{k}$ which correspond to long wavelengths. The schematics in the center column of Figure 2.2 illustrate how the allowable $\vec{k}$ states (in the conduction band) become reduced with 1, 2, and 3 dimensional size confinement.

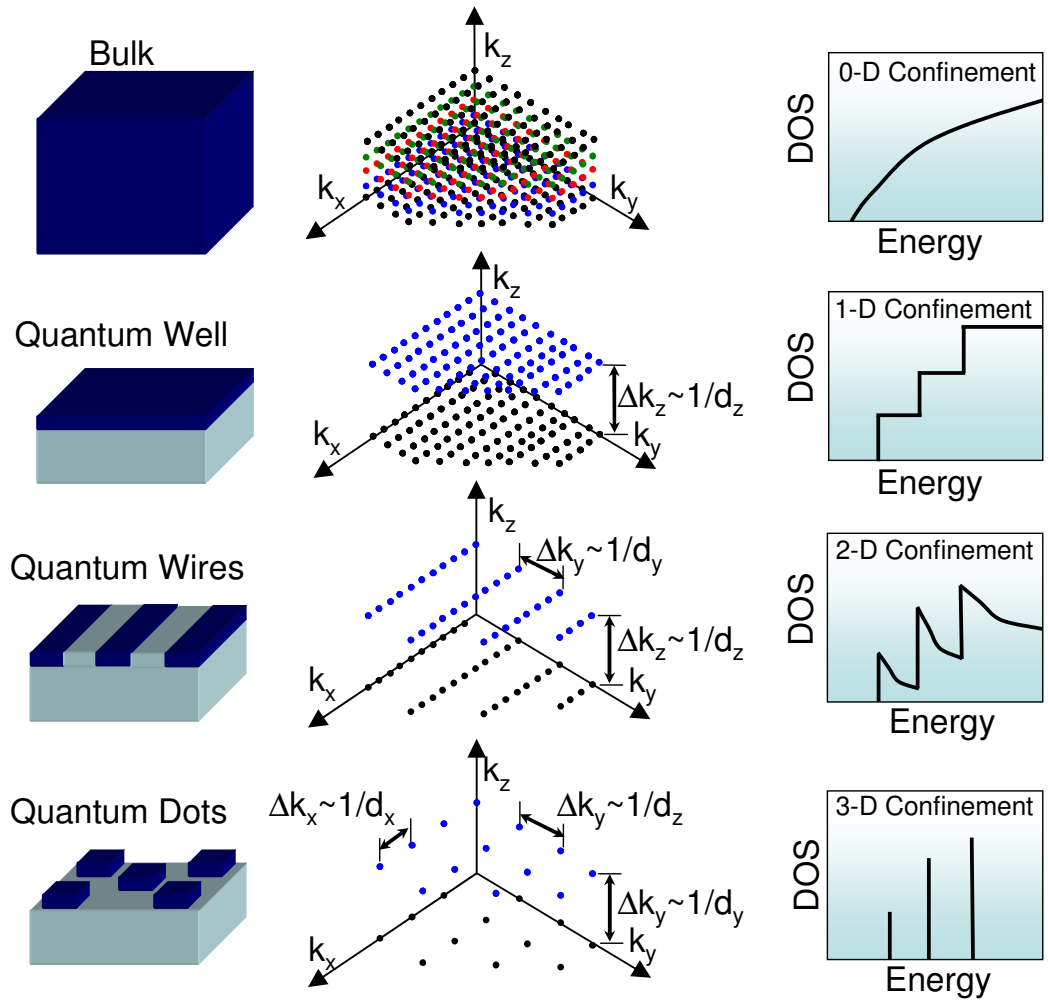

Figure 2.2. Moving from left to right the schematics depict the structure under consideration, the corresponding allowed electronic $\vec{k}$ in reciprocal space, and the density of states with respect to energy for electrons referenced from the top of the valence band. Increasing confinement is depicted from the top down beginning with no confinement, 1-D, 2-D, and 3-D.

The final column of this schematic depicts the resulting density of states (DOS) in the conduction band (after zone folding [44]) for the materials with the various dimensionalities of size confinement. The density of states is the number of states between $E_{\vec{k}}$ and $E_{\vec{k}} + dE_{\vec{k}}$. These relationships are determined by differentiating the total number of states up to energy $E_{\vec{k}}$ with respect to energy, where $E_{\vec{k}}$ is related to $\vec{k}$ by $E_{\vec{k}} = E_g + \frac{\hbar^2}{2m_e^*}\left(k_x^2 + k_y^2 + k_z^2\right)$ and E_g is the bandgap [44]. To better explain how the

DOS is obtained from the allowed $\vec{k}$ requires the use of an example. Consider a sphere centered at the origin on the reciprocal space state map for the bulk material in the figure above (the sphere having a radius of $\left|\vec{k}\right| = \sqrt{k_x^2 + k_y^2 + k_z^2}$). For a very small sphere, there are no states present indicating a bandgap; as the sphere increases in size, the number of states increases. The DOS of states corresponds to the rate of change in the number of states which are within this sphere[1]. In the case of the quantum well the density of states follows analogously; however, one degree of freedom has been lost so the states fill a circle in $\vec{k}$ -space. The rate of change in the number of states within the circle remains constant (after the first state is encountered) since only the "black" states are being included. A sudden increase in the density of states is observed at slightly higher energy which corresponds to a higher band of allowable states, the "blue" states. Similar descriptions can be applied to the quantum wire and quantum dot materials, wherein the states are counted along a line and at discrete points in $\vec{k}$ -space, respectively.

To estimate the length in which such quantum size effects become apparent, the Bohr model can be used. Using the equation [44]:

$$R_B = \frac{\varepsilon m_e}{m_e^* + m_h^*}\left(\frac{4\pi\varepsilon_o \hbar^2}{m_e e^2}\right) = \frac{\varepsilon m_e}{m_e^* + m_h^*} a_B \,, \tag{2.9}$$

where $m_{e,h}$, $m_{e,h}^*$ are the free electron (hole) mass and the effective mass of an electron (hole) in a material, ε_o, ε, are the permeability of free space and the relative permeability of a material, $\hbar$ is the Planck's constant divided by 2π, e is the charge on an

[1] It should be noted that the density of states is with respect to energy, and therefore, the radius of the sphere would increase linearly with energy, or as $\sqrt{\left\|\vec{k}\right\|}$.

electron, and a_B is the Bohr radius of a hydrogen atom. In Figure 2.3 the product of the bandgap and the Bohr exciton radius R_B found using (2.9) is plotted for several III-V materials, Si, and Ge. Plotting the data in this manner illustrates that the Bohr exciton radius is roughly $10/E_g$ - $20/E_g$ [nm], and therefore increases with decreasing bandgap. The Bohr exciton radii averaged over the many different possible electron and hole effective masses are labeled on each box, the bottom and top of which indicate the first and third quartile providing a sense of the range of effective masses. From Figure 2.3 it is apparent that quantum size effects will begin to be important for InAs structures when one of the dimensions is reduced to 42 nm where as the size of GaP structures must be reduced 4.2 nm or less. The large Bohr exciton radius of InAs allows for a large tuneablity and also control over the tuning since a reduction by one layer of atoms (or about 0.25 nm) is a small fraction of the total size. This control is not achievable in the materials with smaller Bohr exciton radii.

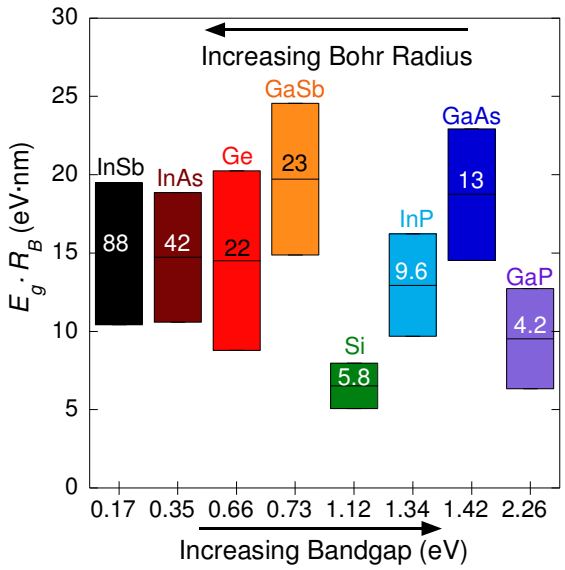

Figure 2.3. Product of the bandgap and the Bohr exciton radius for various III-V in addition to Si and Ge for reference. The materials are arranged in order of increasing bandgap.

Applications which utilize nanomaterials, such as quantum dot solar cells, are aimed at capitalizing on the unique properties associated with an ensemble of nanostructures. The delta function-like states associated with quantum dots resembles the discrete electronic orbital energy levels of individual atoms. Like atoms, when quantum dots are assembled into three dimensional structures, these discrete-like states overlap, and due to the Pauli exclusion principle, they must separate. This separation leads to the formation of narrow "mini-bands" of allowed energy states and is analogous to the electronic band structure associated with semiconductors. In the case of InAs quantum dots grown within a GaAs host lattice, these mini-bands create allowed energy states within the forbidden energy bandgap of the GaAs. These states are theoretically expected to be long-lived (long lifetime), have a high oscillator strength (optical absorption), and have a Fermi level which is independent from that of the bulk GaAs [45]. These enhanced properties make them ideal for use in optoelectronic devices including light emitting diodes, lasers, infrared photodetectors, and solar cells.

A pioneering theoretical study by A. Luque and A. Marti predicted that a device in which an intermediate electronic band within the forbidden energy bandgap of a host material and independent from the electronic levels could lead to a solar conversion efficiency of 63.2% under maximum solar concentration (46,050 suns) [46]. This greatly exceeds the thermodynamic maximum efficiency of standard single junction solar cell operation as calculated using detailed balance [47]. Furthermore, Brown *et al.*, recently presented a study that has extended the intermediate band theory to four intermediate bands wherein a theoretical limiting efficiency of 71.7% was computed. This is

approximately a factor of 2 better than current state-of-the-art (SOA) triple junction space solar cells and theoretically comparable to a 36 junction, multi-junction cell.

The presence of an ordered array of semiconducting quantum dots within the junction of a p-type / intrinsic / n-type cell may lead to the formation of an energy band or bands within the bandgap of the solar cell. These aforementioned quantum dot mini-bands could potentially serve as intermediate bands thereby enabling the physical development of intermediate band solar cells. The presence of these mini-band states allows for harvesting of lower energy (longer wavelength) photons that would normally be un-absorbed by the cell. The key to this device is that the low energy photons can be harvested without also having the unwanted effects of voltage and efficiency degradation, which is associated with using an ordinary narrow bandgap device for converting such photons. Devices comprised of InAs quantum dots within a GaAs host are currently under investigation for use as the middle junction in multijunction space solar cells [48-50]. In this device, the role of the quantum dots is also to extend the band edge of the middle junction device to longer wavelengths, thereby increasing the current of the middle junction and the entire current matched stack. In such a device, however, a small reduction in voltage could be tolerated. These quantum-dot "enhanced" multijunction solar cells have a theoretical one-sun limiting efficiencies of over 45% [48].

Quantum dot structures can be fabricated either by using photolithographic techniques, or by using a self-assembly technique called the Stranski-Krastanov growth mode [49, 50]. This technique takes advantage of the strain energy generated from the lattice mismatch between the host material and the quantum dot material to transition the growth from 2D layer-by-layer growth to 3D "island" growth. Thus, after a nucleation,

or wetting, a layer consisting of at least one monolayer of dot material is deposited onto the host material, quantum dots will form provided the dot formation is energetically favorable compared to the generation of a misfit dislocation. In addition, the increase in surface energy due to island formation must be smaller than the strain energy relieved. A series of quantum dot layers with intermediate cladding layers can be grown to produce three dimensional arrays. Self organization due to lattice strain leads to the columnar arrangement of dots [45].

In addition to the unique optical properties, the long lifetimes and the potential for increased mechanic strength lead to potential ancillary benefits associated with InAs quantum dot / GaAs *pin* solar cells in terms of improved radiation tolerance and improved thermal dependences. To date, there have been many reports in which InAs quantum dots demonstrate an order of magnitude greater resilience to ionizing radiation over that of bulk and quantum well structures used in optoelectronic devices such as light emitting diodes or lasers [51-55]. The ability to obtain similar results in InAs quantum dot / GaAs *pin* solar cells could potentially lead to longer operating lifetimes of solar cell-based space power systems and radiation tolerant devices which are capable of supporting long-life radioisotope battery operation employing high energy beta or alpha particle radiation sources.

CHAPTER 3. *ADEP* AND D^3P MODELING

3.1 ALPHA-PARTICLE ENERGY DEPOSITION PROFILE (*ADEP*)

In space, or when used in radioisotope batteries, the flux of ionizing radiation will be incident with a semiconductor uniformly from all direction. To experimentally simulate this flux one may use an extended radioisotope source from which particles are isotropically emitted. Colerico *et al.*, used a 1 mCi ^{241}Am source, which emits ~5.5 MeV alpha particles, to simulate the effects of electron, proton, and light-ion irradiation in space [56]. Furthermore, ^{90}Sr and ^{60}Co radioisotope sources are commonly used in the electronics industry to simulate the effects of high energy electrons and gamma-rays, respectively, in MOSFETs, DRAM, and CCDs [9]. To accurately utilize this approach, the flux of particles and the rate of ionizing and non-ionizing energy deposited spatially within the material must be determined. Since a ^{210}Po source has been used to experimentally investigate these effects, the following methodologies are developed for alpha-particles emitted from an extended source; however, the approach utilized here is completely general. To simulate electrons or gamma-rays the functional forms of the stopping curves for these particles need to be inserted in place of those used for alpha-particles.

It is well established that α-particles of a given initial energy will follow approximately linear paths of constant range as they traverse through matter [57]. As shown in Figure 3.1 the functional form of the energy loss along the alpha-particle path is independent of the material, although it is scaled or stretched depending on the material's density and effective atomic number. The data in Figure 3.1 was generated from 20,000 alpha particle histories simulated using a Monte Carlo simulation tool, SRIM-2003 [11,

57]. This software tool utilizes the functional form of Equation (2.7) and also accounts for the stochastic nature of the alpha-particle / matter interactions to arrive at a stopping curve. Similar Monte Carlo based code is available for electronic stopping such as monte CArlo SImulation of electroNs in sOlids (CASINO) programmed by Raynald Gauvin and co-workers, or electrons and photons such as PENELOPE offered by Francesc Salvat, Jose M.Fernandez-Varea [58]. The stopping curve can further be broken into the ionizing and non-ionizing energy loss of the particle while slowing down in the material. The ionizing portion or alpha-particle energy loss is plotted in Figure 3.1 below.

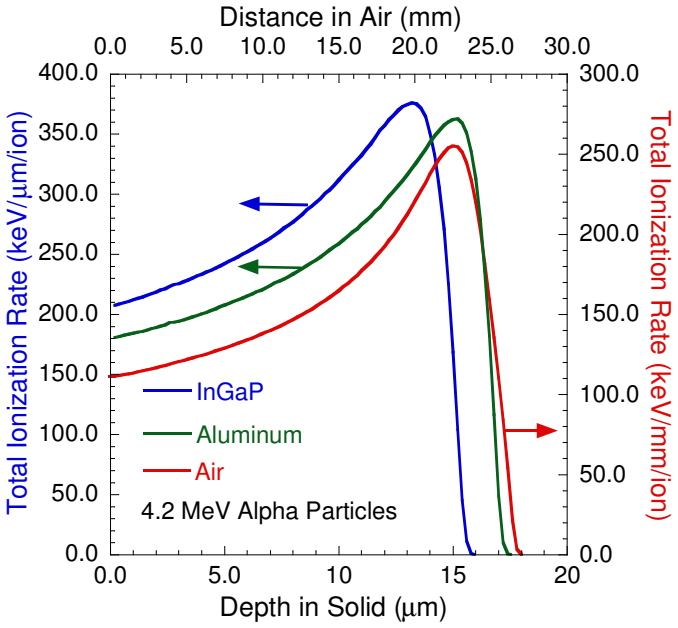

Figure 3.1. Total ionization rate per unit distance for alpha-particles in $InGaP_2$, Al, and Air. The bottom and left axis apply for the two solids, while the top and left axis are used for air.

Calculating the flux incident with a diode that is isotropically emitted from an extended alpha-particle source is analogous to the methodology used for calculating the amount of light incident with a detector after propagating through an imaging system. A good review of such radiometric calculations can be found in ref. [59]. In short, the

alpha-particle flux $d\Phi_c$ incident with a differential area dA_c on the surface of a photovoltaic cell is [59]:

$$\begin{aligned} d\Phi_c &= dA_c \frac{\varphi_s}{2\pi A_s} \int_0^{R_s} \int_0^{2\pi} \frac{dr_s \, d\theta_s \, r_s G_{air}^2}{\left|\vec{L}_1\right|^4} \\ &= dA_c \frac{\varphi_s}{2\pi A_s} \left[1 - \frac{r_c^2 + G_{air}^2 - R_s^2}{\sqrt{\left(r_c^2 + G_{air}^2 + R_s^2\right)^2 - 4 r_c^2 R_s^2}} \right], \end{aligned} \tag{3.1}$$

where the integration is taken over the entire surface area of the extended alpha-particle source of area A_s, radius R_s, and activity φ_s. The air gap between the source and device is G_{air}, and the vector extending from a point on the source to a differential area dA_c on the cell is[2] $\vec{L}_1 = [r_s\cos\theta_s - r_c\cos\theta_c,\ r_s\sin\theta_s - r_c\sin\theta_c,\ G_{air}]^T$, where r_s and θ_s define positions on the source and r_c, θ_c, and z_c, define the position of the differential volume (see Figure 3.2a). To arrive at (3.1) the alpha-particle source was assumed to obey Lambert's cosine law [59], and therefore the following was used as the radiance of the alpha-particle source:

$$\ell_s = \frac{\varphi_s}{2\pi A_s}. \tag{3.2}$$

The above calculation pertains only to the flux incident with the surface of the device. Within the device, the flux will continually reduce with increasing depth and radial distance from the center of the source. Furthermore, the rate of alpha-particle energy loss is inversely proportional to the instantaneous energy of the particle [57], thereby increasing as the particle penetrates into the material. To calculate the energy deposited by alpha particles spatially within a device, the alpha-particle flux and the rate

[2] This vector could equivalently be defined using a Cartesian coordinate system for cell locations where $x_c = r_c\cos\theta_c$, $y_c = r_c\sin\theta_c$, and the depth in the cell can be including by using $G_{air} + z_c$.

at which the alpha particles deposit energy upon reaching a differential volume *dv* must both be considered. This spatial alpha particle energy deposition profile (*ADEP*) can be calculated using:

$$ADEP(\varphi, v) = dv \frac{\varphi_s}{2\pi A_s} \int_0^{R_s} \int_0^{2\pi} \frac{(G_{air} + z_c) r_s}{\left|\vec{L}_1\right|^3} \frac{dE_c}{dx}\left(L_{c,eff}\right) d\theta_s \, dr_s \,. \tag{3.3}$$

The function dE_c/dx is the ionization energy loss rate of alpha particles in the material of the photovoltaic cell under investigation and is obtained by a cubic spline of the simulation results (Figure 3.1) of SRIM-2003. This function depends on the instantaneous energy of the alpha particle upon reaching the *dv*, which can be found by using the effective path length $L_{c,eff}$:

$$L_{c,eff} = L_c + \Re_c(E_0) - \Re_c(E_{air}) \tag{3.4}$$

with,

$$E_{air} = E_o - \int_0^{L_{air}} \frac{dE_{air}}{dL} dL \tag{3.5}$$

$$L_1 = \left(r_c^2 + r_s^2 - 2 r_s r_c \cos(\theta_s - \theta_c) + (G_{air} + z_c)^2\right)^{1/2} \tag{3.6}$$

$$L_{air} = \left(\frac{G_{air}}{G_{air} + z_c}\right) L_1 \tag{3.7}$$

$$L_c = L_1 - L_{air} \tag{3.8}$$

In (3.4) and (3.5), E_{air} is the energy of the alpha-particle as a function of the linear distance traversed in air L_{air} and starting with an initial energy E_0. It accounts for the slow-down of the alpha particle as it moves through air. The function $\Re_c(E)$ is the range of alpha particles in the diode material as a function of the energy of the alpha particle upon reaching the surface of the device. Furthermore, L_c is the linear distance traversed in the diode (*i.e.*, cell). Equation (3.5) was used to obtain a functional form for $E_{air}(x)$

which yields consistent results to that obtained by the procedure suggested by Messenger, *et al.* [60].

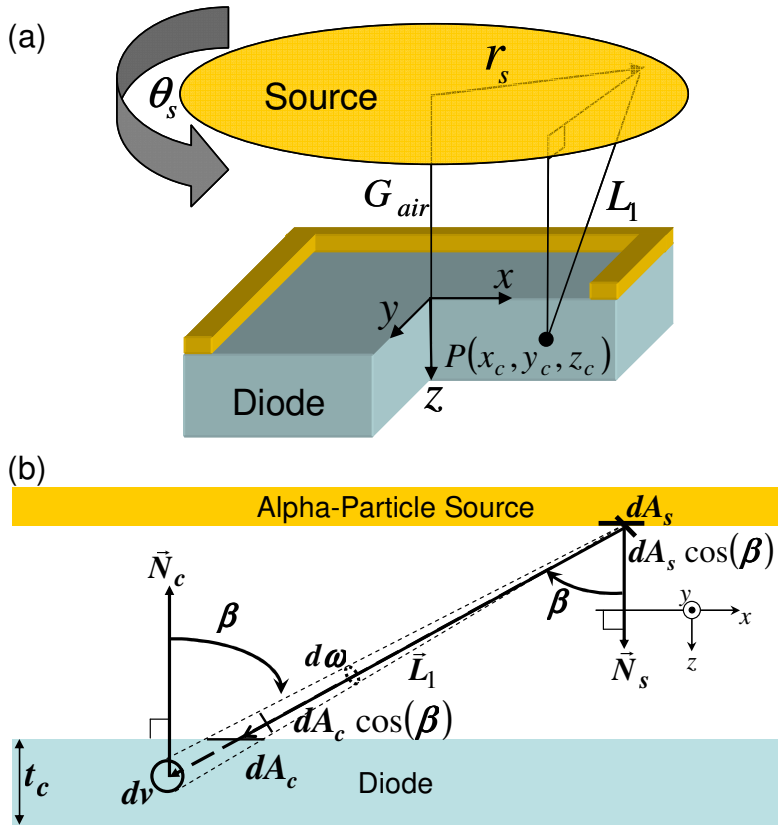

Figure 3.2. (a) Source – diode configuration used to measure radioisotope batteries and to simulate the space radiation environment. (b) A cross section of the geometry in (a) used to illustrate how the flux and *ADEP* is calculated.

To determine the *ADEP* in situations wherein alpha particles must traverse through additional surface coatings (*e.g.,* anti-reflective coatings, window layers, etc.,) before reaching the device, the energy lost in this material, in addition to that lost in air, must be accounted for. To accomplish this, the effective path length (3.4) becomes:

$$L_{c,eff} = L_c + \Re_c(E_0) - \Re_c(E_{abs}), \tag{3.9}$$

where E_{abs} is the energy of the particle as a function of distance traveled in the additional absorber, L_{abs}. The value of E_{abs} is found in a similar manner as the energy lost in air where:

$$E_{abs} = E_{air}(L_{air}) - \int_{L_0}^{L_{abs}} \frac{dE_{abs}}{dL} dL \,; \tag{3.10}$$

however, the limit of integration starts at a different value L_0 and the energy of the particle upon reaching the surface of the absorber is taken as E_{air} at $L = L_{air}$. These two corrections are used to account for the energy lost in air before reaching the absorber surface. Finally,

$$L_0 = \Re_{abs}(E_0) - \Re_{abs}(E_{air}). \tag{3.11}$$

To illustrate the effect of additional absorbers, the equations of $L_{c,eff}$ for energy lost in air and one absorber (3.12) and for energy loss in air and two absorbers (absorber two has length $L_{abs,2}$) (3.13) are explicitly provided below.

$$L_{c,eff}(E_0, L_c, L_{abs}, L_{air}) = L_c + \Re_c(E_0) - \Re_c\left(E_0 - \int_0^{L_{air}} \frac{dE_{air}}{dL} dL - \int_{L_0}^{L_{abs}} \frac{dE_{abs}}{dL} dL\right) \tag{3.12}$$

with,

$$L_0(E_0, L_{air}) = \Re_{abs}(E_0) - \Re_{abs}\left(E_{air}(E_0) - \int_0^{L_{air}} \frac{dE_{air}}{dL} dL\right).$$

$$L_{c,eff}(E_0, L_c, L_{abs,2}, L_{abs}, L_{air}) = L_c + \Re_c(E_0) - \Re_c\left(E_0 - \int_0^{L_{air}} \frac{dE_{air}}{dL} dL - \int_{L_0}^{L_{abs}} \frac{dE_{abs}}{dL} dL - \int_{L_{0,2}}^{L_{abs,2}} \frac{dE_{abs,2}}{dL} dL\right) \tag{3.13}$$

again with,

$$L_0(E_0, L_{air}) = \Re_{abs}(E_0) - \Re_{abs}\left(E_{air}(E_0) - \int_0^{L_{air}} \frac{dE_{air}}{dL} dL\right),$$

and

$$L_{0,2}(E_0, L_{abs}, L_{air}) = \Re_{abs,2}(E_0) - \Re_{abs,2}\left(E_0 - \int_0^{L_{air}} \frac{dE_{air}}{dL} dL - \int_{L_0}^{L_{abs}} \frac{dE_{abs}}{dL} dL\right).$$

It should be apparent how additional absorber layers can be included to this calculation following a similar procedure. The difference between each additional layer is an added energy loss integral term which has limits of integration that account for the energy lost by the alpha particle in all previous layers. Numerically solving for $L_{c,eff}$ with multiple absorbers becomes computationally time consuming because every possible set of air and absorber lengths that the alpha particle is likely to encounter needs to be solved. When doing so, first a 1-D array of length N is needed to determine the energy lost in air as a function of distance traversed. Accounting for air plus one absorber layer requires a 1-D array of length M to be solved for every incident alpha-particle energy yielding a 2-D matrix of size N × M. A 3-D matrix of size N × M × O is needed to calculate the *ADEP* for a two-absorber (plus air) case, and so-on. It is important to note that each point in these arrays (matrices) requires an integration of dE_x/dL to be preformed. This method for calculating the effective path length of a particle is made possible by the fact that the rate of energy loss depends only on the energy of the particle (current energy) and the material in which it is traversing. Therefore, the *ADEP* methodology uses the effective path length to determine the energy of the particle upon reaching a material and travels along the dE_x/dL curve from that point forward to determine the deposited energy at *dv*.

Figure 3.2b can be used to illustrate why different geometrical factors are used when calculating the flux and *ADEP*. When calculating the flux, the solid angle

subtended by the area dA_c as viewed from a point on the source is $d\omega = dA_c \cos\phi / |\vec{L}_1|^2$ where ϕ is the angle between the normal to the alpha-source source and the position vector $\vec{L}_1$. Clearly, as ϕ increases, the size of dA_c must appear to get smaller when viewed from the source; this is consistent with the above relation since $d\omega \rightarrow 0$ as $\phi \rightarrow 90°$. When considering the *ADEP*, the alpha-particle source is emitting into a differential volume. As the position of dA_s is moved along the surface of the source (*i.e.,* as ϕ is varied) the size of *dv* will "look" the same (albeit reduced in size due to the increased distance). Mathematically this difference corresponds to eliminating the cosine dependence on the solid angle. Physically, no projected area correction is required for the calculating the energy absorbed in the cell since the cell is divide into differential volume elements which have depth and therefore can accept radiation equally from all directions. The volume elements can be thought of as "point acceptors" the complement to that of a "point source."

3.2 NON-IONIZING ENERGY LOSS AND D^3P

The dependence of space power systems on solar energy conversion has motivated research aimed at understanding radiation damage and reducing its effects in the III-V semiconductor based photovoltaic arrays used in space. The displacement damage dose (D_d) methodology, developed by the Naval Research Laboratory (NRL), is the *de facto standard* for characterizing radiation damage in these devices [14-17, 60]. As previously discussed, the slow radiation-induced performance degradation observed in III-V semiconductor devices employed in radiation environments is associated with the

lattice displacements caused by the non-ionizing energy loss (*NIEL*) of the irradiating particles. *NIEL* can best be described by Walters *et al*. [15]:

> The rate at which an irradiating particle loses energy to nonionizing events is what is referred to as the nonionizing energy loss (*NIEL*). *NIEL* is a direct analog of the linear energy transfer (*LET*) or stopping power for ionization events. The units of *NIEL* are typically MeV/cm or MeVcm^2/g. The calculation of *NIEL* requires information regarding the differential scattering cross section for atomic displacements ($d\sigma/d\Omega$), the recoil energy of the target atoms (T), and a term which partitions the energy into ionizing and nonionizing events, called the Lindhard partition factor (*P*). *NIEL* can be written as an integral over the solid angle [61-63] *i.e.*,
>
> $$NIEL(E) = \frac{N_A}{A} \int_{\theta_{\min}}^{\pi} \frac{d\sigma(\theta, E)}{d\Omega} T(\theta, E) P(T(\theta, E)) d\Omega$$
>
> where N_A is Avogadro's number, A is the atomic mass, and t_{min} is the scattering angle for which the recoil energy equals the threshold for atomic displacement.

Messenger *et al*. described an equivalent method for calculating the *NIEL* (in terms of energy or depth) of heavy ions using the stopping curves provided by SRIM-2003 [60]. In summary, the number of vacancies produced as a function of depth by a particle and its PKO's are multiplied by a constant corresponding to the energy required to create a vacancy *M* (in eV/Vacancy):

$$M = \frac{E_{th}}{0.4} + E_{binding} \tag{3.14}$$

where E_{th} and $E_{binding}$ are the threshold energy for atomic displacement and the binding energy, respectfully [60]. Using this equation and the vacancy generation per unit path length supplied from SRIM-2003, a functional form for $NIEL(x)$ can be obtained for alpha-particles in the semiconductor material of choice. Combining (3.3) with (3.14) and replacing the alpha-particle flux φ_s with the total alpha-particle fluence ϕ_s allows the displacement damage dose profile (D^3P) to be calculated (in eV/μm^3):

$$D^3P(\phi_s, v) = dv \frac{\phi_s}{2\pi A_s} \int_0^{R_s} \int_0^{2\pi} \frac{(G_{air} + z_c) r_s}{\left|\vec{L}_1\right|^3} NIEL(L_{c,eff}) d\theta_s \, dr_s \tag{3.15}$$

With this equation, the spatial extent of the damaging energy deposited by alpha-particles emitted from an isotropic source can be determined. Finally, to obtain the D_d that will cause degradation in III-V semiconductor devices, D^3P is integrated over the active volume of the device. In a single junction III-V device the active volume corresponds to the region between the back surface field layer and the window layer.

The main utility of this methodology results from the independence of D_d on the type of irradiating particle. In theory, the effects of exposure to any type of irradiation (or combination thereof) can be determined from a single acquisition of experimental radiation damage data. Once the rate of degradation with respect to D_d is found for one particle type, the rate of damage caused by other particles can quickly be found using the characteristic damage equation from the Solar Cell Radiation Handbook [64]:

$$X(D_d) = X_0 - C_x \log\left(1 + \frac{D_d}{D_x}\right) \tag{3.16}$$

where X_0 is any solar cell parameter including V_{oc}, I_{sc}, P_{max}, etc., at beginning of life, and C_x and D_x are fitting parameters for each parameter and are specific to the solar cell structure and material. This allows one to use the results of proton irradiation to provide information regarding electron irradiation or alpha particle irradiation simply by using the theoretical *NIEL* values calculated from SRIM-2003.

3.3 Energy Thresholds with Tersoff Potentials

The probability and magnitude of the energy lost by irradiating particles to non-ionizing events is fundamentally dependent on the energy threshold for atomic

displacement E_{th}. Historically, the determination of E_{th} has been performed experimentally whereby the rate of change in various material properties (*e.g.,* resistivity, carrier lifetime, etc.) is monitored with respect to the energy of irradiating electrons [65, 66]. An alternative approach for investigating E_{th} has been through the use of molecular dynamic simulation. This technique dates back to the early 1960s when Vineyard and co-workers investigated the formation of defects in copper and iron [67, 68]. In general, the classical equations of motion are used to describe the behavior of hundreds of thousands of atoms. The interaction of the atoms is entirely dependent upon the lattice potential energy function; no assumptions are made regarding the structure of the material (except when initializing a simulation) or the nature of defects which may form by collision events. Initially all particles are at rest in a perfect lattice and the start of a radiation damage event is considered to be the sudden transfer of momentum to a PKO atom. The local potential energy then dictates the ability of an atom to be displaced as a result of the initial momentum transfer [67].

The accuracy of such simulations is entirely dependent upon the assumed potential energy function which dictates the magnitude and direction of forces controlling the motion of the PKO. The Lennard-Jones potential is a well known potential energy function consisting of 2-body pair potentials describing the attractive (ion-electron) and repulsive (ion-ion and electron-electron) forces associated with ionic materials [44]. This potential energy function favors the formation of close-packed structures, such as face centered cubic. To describe the diamond-like binding (*i.e.* zinc blend) associated with III-V semiconductors, three-body interactions terms are necessary. Potential energy functions which have been used to model III-V semiconductor bulk and nanomaterials

include the Keating potentials [69] , the valence force field method [70], the Stiller-Weber potentials [71], and the Tersoff potentials [72-74].

Tersoff interatomic potentials are analytically defined functions which describe 2-body and 3-body interactions of an N-body system. The inclusion of the 3-body interactions provides a means to stabilize more open structures such as diamond and zinc blend. The final component of the Tersoff model is a bond-order dependent attraction term which varies the strength per bond depending on the local environment of the atom. This results in a more realistic attractive potential (especially in partially ionic systems) and allows for non-equilibrium bonding (*e.g.*, bonds with atoms in interstitial sites) to be more accurately modeled. The Tersoff potentials have been used on many occasions to investigate the properties associated with GaAs and InAs materials. Some examples include the InGaAs/GaAs strained-layer relaxation process [75, 76] and the melting behavior of GaAs [77]. This set of potentials is ideal for investigating the effect that materials properties have on E_{th}.

The Tersoff potentials are defined by the following set of equations:

$$E_{eq} = \frac{1}{2}\sum_{j \neq i} f_c(r_{ij})\left(V_{ij}^{R}(r_{ij}) + b_{ij}V_{ij}^{A}(r_{ij})\right), \tag{3.17}$$

$$V^{R}(r_{ij}) = A_{ij}\exp(-\lambda_{ij}r_{ij}), \tag{3.18}$$

$$V^{A}(r_{ij}) = B_{ij}\exp(-\mu_{ij}r_{ij}), \tag{3.19}$$

$$b_{ij} = \left(1 + (\gamma_{ij}\zeta_{ij})^{n_i}\right)^{-n_i/2}, \tag{3.20}$$

$$\zeta_{ij} = \sum_{k \neq i,j} f_c(r_{ik})g(\theta_{jik})\exp\left(\lambda_o^3(r_{ij} - r_{ik})^3\right), \tag{3.21}$$

$$g(\theta_{jik}) = 1 + \frac{c_i^2}{d_i^2} - \frac{c_i^2}{d_i^2 + (h_i - \cos(\theta_{jik}))^2}, \tag{3.22}$$

$$f_c = \begin{cases} 1, r_{ij} < R_{ij}, \\ \frac{1}{2}\left(1 + \cos\left(\pi\left(r_{ij} - R_{ij}\right)/\left(S_{ij} - R_{ij}\right)\right)\right), R_{ij} < r_{ij} < S_{ij}, . \\ 0, r_{ij} > S_{ij}; \end{cases} \tag{3.23}$$

The total energy per atom, E_{eq} is found by summing the repulsive bond energy (3.18) and the attractive bond energy (3.19) between atoms i and j with interatomic spacing of r_{ij}. The cutoff function (3.23) is used to limit the neighbors j which affect the cohesive energy of atom i, the "focus" atom. Equations (3.20) – (3.22) are used to determine the aforementioned bond-order term which varies the level of the attractive potential depending on the number of atoms the focus atom is bonding with. The values of the variables used to parameterize the equations are free parameters which are obtained by fitting the equations to agree with empirical data.

Determining the full extent of damage caused by a particle-atom collision event requires the use of a fully dynamic simulation program to track the path of the PKO. In contrast, the determination of E_{th} can be performed using a static lattice since one is not concerned with the subsequent motion of the particle. However, for such a calculation to be physically meaningful, the movement of the PKO must be much faster than that of the thermal oscillations of the lattice. In other words, the PKO must be moving so fast that the lattice "appears" to be standing still. Provided this condition is met, the E_{th} can then be found by calculating the energy of the focus atom (PKO) at sites within the lattice at a distance dr from the equilibrium lattice location. The maximum energy encountered along a path prior to reaching a local energy minimum (interstitial site) is the E_{th} in that

direction. Performing this calculation along all (unique) paths allows one to find the true E_{th} for a material. This methodology is used in Chapter 6 to determine the E_{th} of In and As atoms within an InAs lattice. The effect of strain on these values is also investigated.

CHAPTER 4. DIRECT CONVERSION RADIOISOTOPE BATTERIES

Autonomous sensors, tags, tracking and location devices need to be self-powered and have a long operating lifetime to be effective. A strong need exists for new power sources that can provide very long term, reliable power under extreme conditions for such miniature devices. Small, radioisotope power sources that can provide long-lasting, high-density power are an attractive option for addressing this need. From the review of radioisotope battery technologies, provided in Chapter 2, successful radioisotope battery development requires many critical aspects associated with the solid-state power conversion device and radioisotope source to be considered. In particular, the solid-state power conversion devices should employ wide bandgap semiconductors since a high shunt resistance is required. Additionally, wide bandgap materials where shown to have improved radiation tolerance (*i.e.*, GaAs devices demonstrated a 10x lifetime improvement over Si devices). It was also suggested that novel designs, utilizing three-dimensional structures to improve the absorption cross section of the device, may be effective at increasing the power output and efficiency over that of planar devices. To that end, this chapter details the development of a solid-state power conversion device consisting of a three-dimensional repeating n-type / intrinsic / p-type / intrinsic … n-type / intrinsic *nipi*-diode structure.

4.1 *NIPI*-DIODE RADIOISOTOPE BATTERY OPERATION

One of the fundamental keys to a successful radioisotope battery design is to maximize the cross section for nuclear absorption thereby improving the efficiency and power output. The multi-layered *n-i-p-i-…-n-i-p-i* (*nipi*) structure depicted in (Figure

4.1) is a unique device structure that is designed to have a large capture cross section and may also demonstrate improved radiation tolerance. The device operates as follows: charge carriers are generated within the various *n*, *i*, and *p* players through primary and secondary scattering events with gamma, beta, or alpha-particles that are incident with the device. Excess holes in n-type regions (and likewise electrons in p-type regions) are minority carriers and diffuse within the device until they recombine or reach the edge of a depletion region. If the edge of the depletion region is reached the carriers are swept across the junction into the adjacent layer with opposite polarity. These charge carriers can then be considered "collected" since they are now majority carriers and have a long lifetime. Such carriers are analogous to those in a conventional solar cell which are swept from the emitter into the base and must traverse the entire substrate before reaching the back contact.

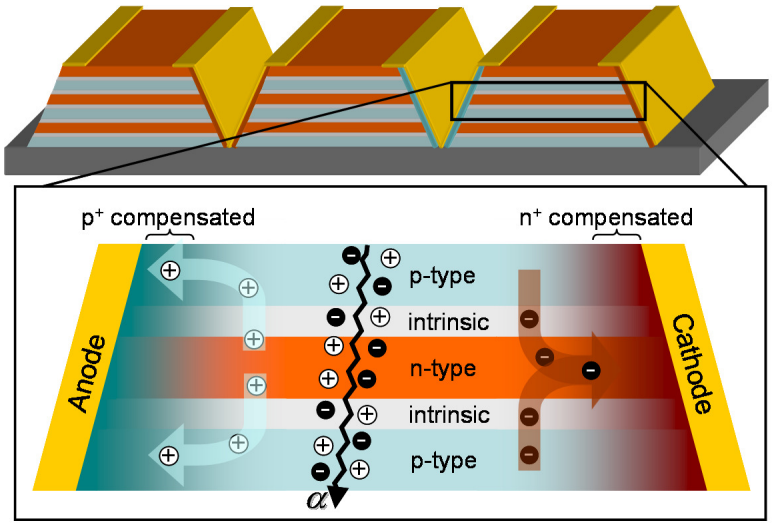

Figure 4.1: A diagram of a *nipi*-structured alpha voltaic battery.

The collection process in a *nipi*-diode is further enhanced by using narrow doped regions. This has the effect of eliminating all quasi-neutral regions within the device and therefore carriers are swept towards the junctions under the assistance of a drift field regardless where they are generated. The use of a drift field also mitigates the effects of

radiation-induced degradation of diffusion length. A drift field exists in regions were a concentration gradient of dopants exists (*e.g.*, at the interface between p-type and n-type layers, between n-type or p-type layers layers and *i*-regions, or within an n-type or p-type region which has a changing dopant concentration) and consists of an electric field that extends along the gradient of the dopant concentration variation. In a standard n-p solar cell, the drift field region is localized within the depletion region, which in $InGaP_2$ can be very small (68 nm was estimated for a n-p junction with constant doping concentrations of 10^{18} cm^{-3}). Therefore, most of the current collection occurs by diffusion of charge carriers through neutral material and therefore carriers are more likely to interact with radiation induced lattice defects. In a drift field, however, the charge carriers are swept away by the electric field resulting in carrier collection that is much faster making it much less probably that recombination occurs.

The final key aspect of the *nipi*-diode structure is to form electrical connection to each layer within the structure without creating a shunting path between adjacent layers. In theory, electrical contacts can be made to these layers by first exposing a region for contacting through chemical V-groove etching, and subsequently compensating two separated regions one with p-type and one with n-type dopants. This results in a rectifying junction with the oppositely poled regions and an ohmic contact with like-poled regions. In terms of fields, the heavily doped surface of the V-grooves will form a drift field which will assist in the collection of electrons in n-type material (and likewise for holes in p-type material) and act as a barrier for the complimentary charge carrier.

To confirm that these favorable conditions can be generated in an ideal theoretical device, a *nipi*-device comprised of 6-*nipi* repeats (6 *pin* and 5 *nip* junctions) was

simulated using the Silvaco Blaze 2-D solid-state device simulator. Figure 4.2a contains a schematic depicting the simulated structure onto which the net doping contour map is overlaid. The device structure was created directly using the *devedit* Silvaco tool. Figure 4.2b shows the total donor and acceptor concentrations as a function of depth into the device. The material used for this simulation was $In_{0.48}Ga_{0.52}P$ with a background doping concentration of 10^{12} cm^{-3} (*i.e.,* the charge carrier concentration in the *i*-regions).

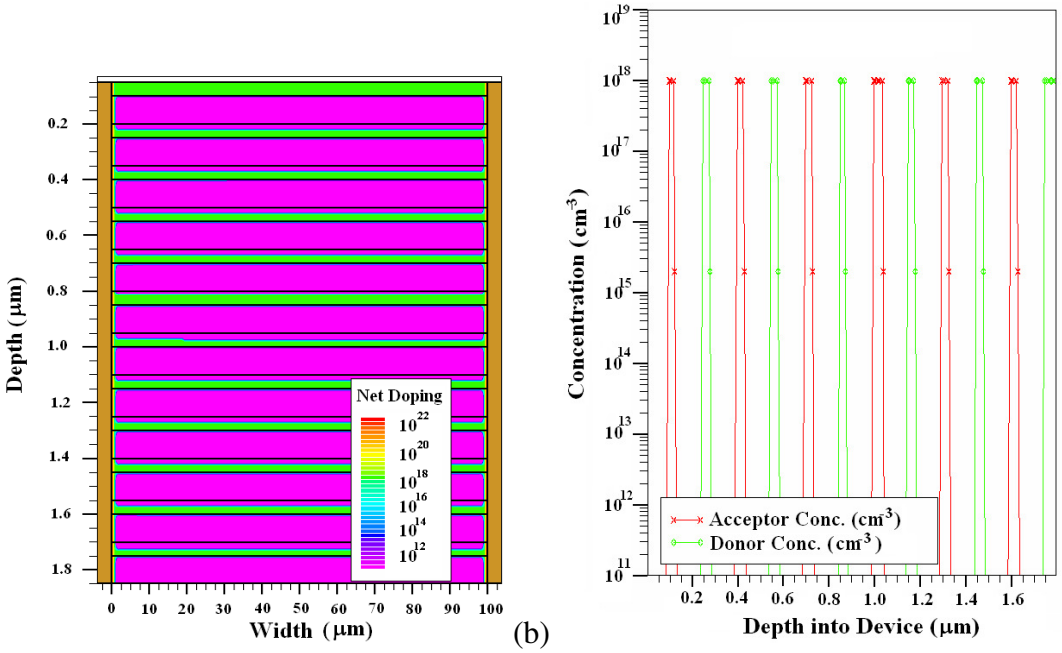

(a) (b)

Figure 4.2. (a) Device structure overlaid with a contour plot of the net doping in the structure, and (b) acceptor and donor doping concentration along a line directed perpendicularly into the device.

To simulate the compensating doping formed at the contacts, an error profile concentration profiled was assumed with a peak doping concentration of 10^{22} at the surface of the V-groove and a characteristic length of 1 μm. This is illustrated in the donor concentration contour plot which is overlaid on the device structure in Figure 4.3. Because of the large variation in device width to height (*i.e.,* 100 μm vs 2 μm), the meshing routine had difficulty forming the dopant profiles at the exact location of the

metallurgic boundaries as defined in *devedit*. However, the exact thickness of these layers is not critical because this simulation is intended to provide proof of concept evidence confirming the energy band structure is consistent with the predicted energy band structure.

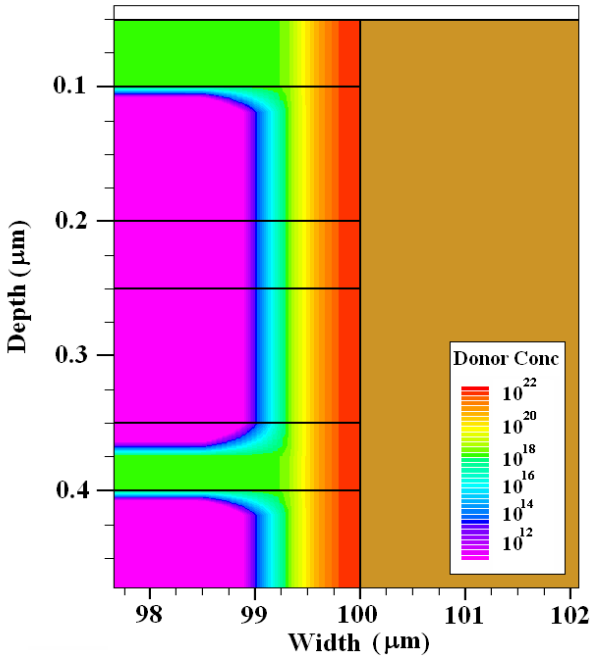

Figure 4.3. Contour plot depicting the donor dopant concentration near the cathode illustrating the high doping in this region which was used to simulate the selective metallization contacting scheme.

Confirmation of the desired drift-field profile within the *nipi*-diode structure is illustrated in Figure 4.4 wherein the simulated electric field profile near the anode is provided. Moving across the structure from left-to-right at a depth of just over 0.2 μm (*i.e.*, within a p-type layer), the following electric fields are encountered. From 0 - 0.7 μm little to no field is present which indicates that the semiconductor is degenerate and acting like a constant potential surface. From 0.7 μm to 0.8 μm a rotation and an increase in magnitude is observed in the field as it starts with low intensity directed towards the anode and rotates counterclockwise finally ending with it directed downward

with larger intensity. A similar variation in field lines is observed at a depth slightly less than 0.3 μm into the device. The variation in field intensity is nearly the same however; the field rotates in the clockwise direction. In this instance, the field is always directed towards a p-type layer, either the edge contact or the p-type layer in the *nipi* structure at a depth of ~0.2 μm. This field would act to force holes into the anode while opposing the passage of electrons.

The variation in electric field along an n-type layer can also be investigated by moving across the structure at a depth of 0.4 μm. Again little to no field is present from 0-0.6 μm, at which point a large increase in field is observed and directed toward the anode. This corresponds to the depletion region in the lateral diode formed between the p-type anode doping and the n-type *nipi* layer. Like before, this field is directed to assist holes to be collected and opposes the motion of electrons into the anode. Moving further across the structure the field lines again rotate however those above and below the 0.4 μm line rotate clockwise and counterclockwise which is opposite to what was observed in the p-type layer.

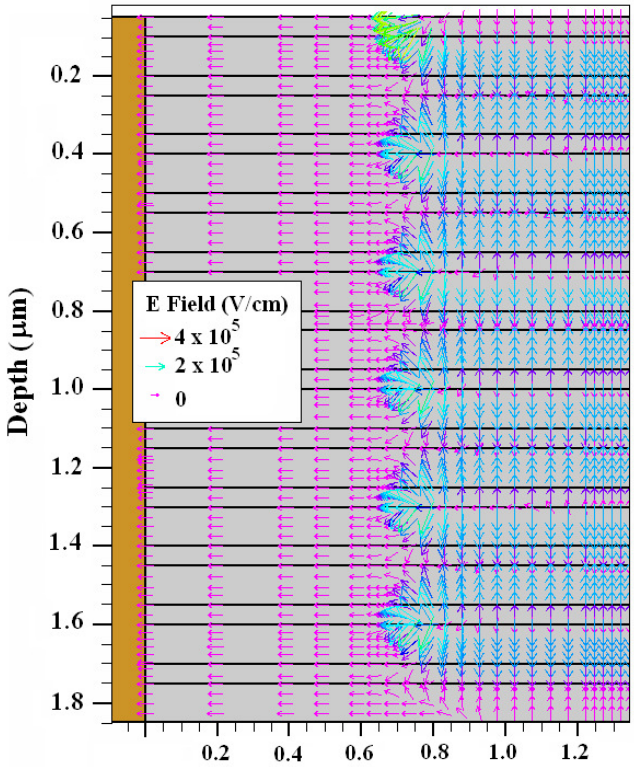

Figure 4.4. Electric field profile near the anode contact of the simulated $InGaP_2$ *nipi*-diode.

The above analysis provides strong evidence supporting that the expected electronic band structure is obtained in the *nipi*-diode. To proceed experimentally, the performance of the individual building blocks of the *nipi*-diode structure, namely various *nip* / *pin* diodes, were studied to better understand the roles of layer thickness, doping profiles, and junction characteristics on device performance. From this work, two independent device design enhancements –thinner *nip* cells and graded junctions – were identified as important steps for increasing the radiation tolerance and performance of *nip* (*pin*) devices. Many of these initial results have been in ref. [37]; in addition, the *ADEP* model is used in this paper to gain additional insight into the operation of the device. Additional results based upon single junction devices are provided below. Follow this, experimental progress towards the development of a *nipi*-diode fabricated using only

smart metallization is provided. These findings indicate a strong potential for *nipi*-diode based radioisotope batteries and radiation tolerant space solar cells, alike.

4.2 SINGLE JUNCTION DEVICE FABRICATION AND TESTING

4.2.1 Device Fabrication

In order to generate the data necessary to optimize the *nipi*-diode structure for radioisotope power generation, many single junction devices were fabricated and tested. Structures were chosen to better understand the roles of layer thickness, doping profiles, and junction characteristics on device performance. Devices were grown using the $In_{0.48}Ga_{0.52}P$ material systems since it is lattice matched to GaAs, has a wind bandgap (E_g = 1.85 eV) and has a strong space heritage as it is known for high radiation tolerance [14]. Devices were epitaxially grown in a Veeco D125LDM organo-metallic vapor phase epitaxy (OMVPE) system at the NASA Glenn Research Center (Figure 4.5). Trimethyl gallium, trimethyl Indium, and phosphine were used for the primary constituents, while disilane and diethyl zinc were used for the n-type and p-type dopants, respectively. Typical growth conditions include a V/III ratio (of gas precursor concentration) of 60, and the devices were grown on p-type (Zn doped) GaAs substrates oriented (100) and off-cut 6° toward the <111>, or n-type (Si doped) with the same orientation. The substrates were held at 620 °C, and a growth rate of 5 Å s^{-1} was used.

Figure 4.5. Veeco D125LDM OMVPE Reactor at NASA GRC used to fabricate the active layers on the in $InGaP_2$ devices.

Following OMVPE growth, front and back-side metallization is preformed. To begin, a layer of SC-1827 photo resist (PR), 3 μm thick, was spun onto the epitaxial layers for protection. Any residual deposits were removed from the back side of the wafers via alternating 30 second etches in concentrated HCl and a solution of peroxide, phosphoric acid, and water (4:3:1); each was performed 3 times. Contact to the now-exposed p-type substrate was made by evaporating 200 Å Au, 200 Å Zn, and ~2 μm Au. A new layer of PR was spun on the front side, patterned using a Carl Suss contact exposure tool, and subsequently developed using DC-26 developer. Following a 5 s HCl etch, the front side contacts were deposited by evaporation of 250 Å Ge, and ~2 um Au. PR lift-off was performed by gentle agitation in acetone. To enhance the contact-substrate adhesion and reduce contact resistance, the wafers were annealed at ~400º C for 5 minutes in Ar. The devices are isolated by etching the material in between the devices down to the substrate. This process consists of a second lithography step followed by wet etching in HCL and 4:3:1. Figure 4.6a is a digital photograph of a wafer just after the topside contacts were deposited. Figure 4.6b is a digital photograph of one of the devices

used in this study. The ring contacts were used to maximize alpha energy deposition within the cell.

(a) 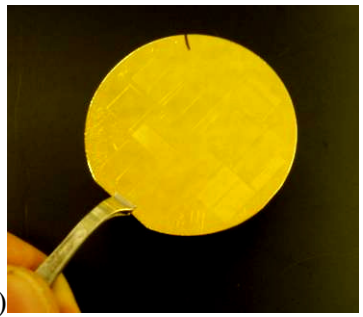 (b) 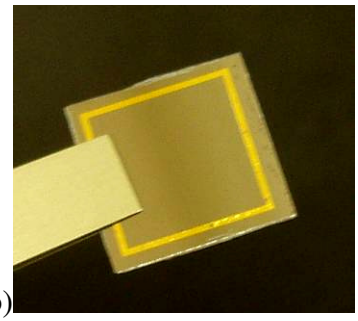

Figure 4.6. (a) A digital photograph of a wafer after topside metallization. (b) A digital photograph of one of the devices with ring contacts used in the study.

4.2.2 Alphavoltaic Battery Power Output Measurements

In an attempt to quantify the output power level of an alpha voltaic battery based on *nipi*-diode solar cells at their current level of development, the power output of the best performing devices were measured under low and high alpha-particle fluxes (Figure 4.7). Under a 1 μCi flux, the J_{sc} was approximately 0.5 nA/cm^2, while the V_{oc} equaled 390 mV (note, the actual flux impacting the cell was 0.506 mCi/cm^2 corresponding to half the total foil flux). Under a 1 mCi flux, the J_{sc} increased by almost 3 orders of magnitude. The increase in J_{sc} was somewhat less than the actual increase in flux. However, it must be noted that the energy per alpha particle was less (*i.e.*, ~4.2 MeV vs. 5.5 MeV) for the higher activity source due to the Au coating on the source as previously discussed. Under the increased level of alpha-particle flux the V_{oc} increased to 540 mV and therefore, the overall efficiency of the device actually increased with flux. This resulted in a maximum power output of 0.080 nW/cm^2 under 1 μCi and 0.0504 μW/cm^2 under 1 mCi with a η_{semi} of 3.2%.

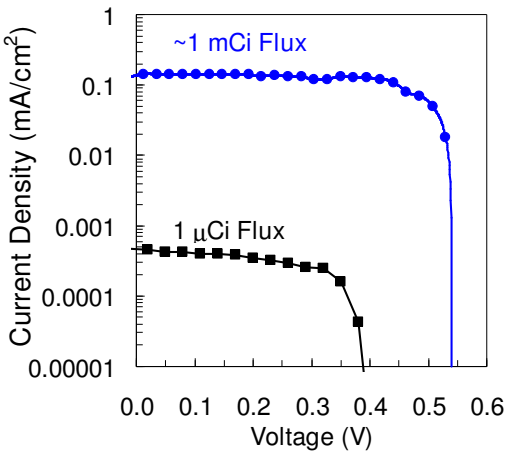

Figure 4.7. Current density vs. voltage for a 1 cm^2 cell under 1 µCi and 1 mCi alpha-particle flux.

An advantage of the *nipi*-device structure is that multiple devices (*pin* / *nip*) devices are stacked together on the same substrate in a very small volume. This allows for additional *nipi*-diodes to be stacked together in a 4π geometry to increase the power output further. Based on the dimensions provided for the bifacial *nipi*-diode stack in Figure 4.8, about 15 of these stacks can be assembled to form a 1 cm^3 battery (assuming a 1 cm^2 area).

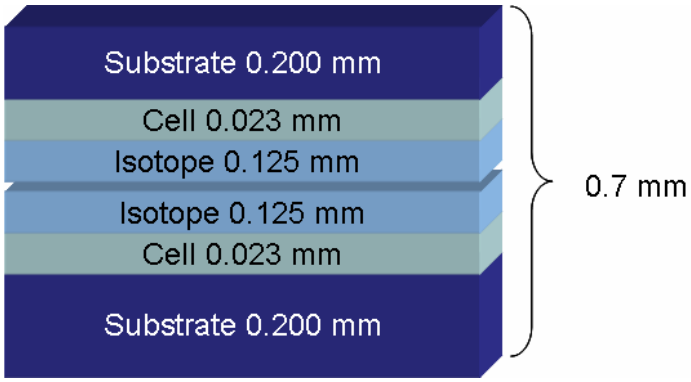

Figure 4.8. Thicknesses of the layers in a bifacial nipi cell.

To demonstrate the stacking ability, three $InGaP_2$ *nip* cells with three ^{210}Po alpha-particle sources were employed. The measured *I-V* characteristics of this stack (3 cells) connected in parallel, a two-cell stack, and a single cell are plotted in Figure 4.9. The V_{mp}

and J_{mp} of the three-cell stack are indicated by the dotted lines and were 0.5 V and 0.26 μA/cm^2, respectively yielding a power output of 0.130 μW. The efficiency is slightly less than reported above because each device was tested with a separate source, and the cells were not perfectly voltage matched because of non-ideal source-device geometry coupling.

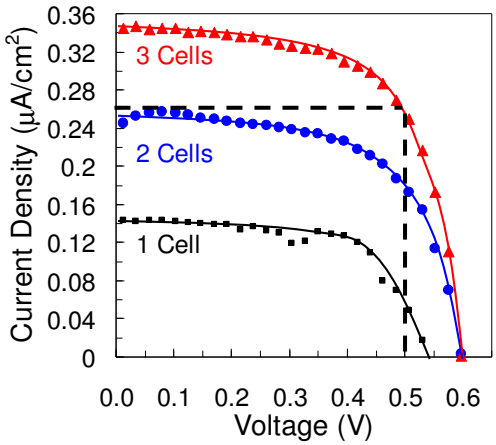

Figure 4.9. Current density verses voltage for a 1 cell, 2 cells and 3 cells under alpha-particle flux.

Determination of the η_{semi} for the devices tested under the ^{210}Po source required the use of the *ADEP* model to account for the non-ideal geometry matching. For accurate determination of this value, it is essential that valid assumptions are used to calculate the energy loss due to poor geometry and due to alpha-particle energy losses in air. In Ref. [38], a methodology for validating the accuracy of the *ADEP* model using a single junction $InGaP_2$ diode, is developed. In brief, the expected input power is calculated using the *ADEP* model and is compared to the actual current output measured from a single junction $InGaP_2$ device. Very good agreement is observed between the experimental and theoretical values confirming the validity of the model.

Ref. [38] also details a framework for modeling *nipi*-diodes and further justifies the approach for achieving high power output from a radioisotope battery using this

device structure. The framework utilizes the *ADEP* model and an equivalent circuit description of the *nipi*-device. The equivalent circuit can best be described using the schematic depicted in Figure 4.10. Each n-type and p-type region is separated with an intrinsic region forming a series of *nip* and *pin* devices connected in parallel. To simulate realistic devices, a current source (the magnitude of which is determined using the *ADEP* model) and a shunt resistor are also modeled in parallel with the diodes. The stacked planar structure of the *nipi*-diode makes contacting each layer a critical aspect dictating the device performance. The details of making such contact are the topic of the remainder of this chapter. In brief, the contacts are made using selective metallization where specifically chosen metal alloys are thermally deposited into groves etched through the entire *nipi*-diode structure. The metal alloys are designed to compensate and dope the semiconductor in the region near the contact. These "contact diodes" have also been included in the model and are depicted in Figure 4.10 below. To model these diodes, their current –voltage behavior was assumed to be identical to that of the vertical diodes with the current flow scaled according to the total surface area of these contacts which is derived from the area of each contacts and number of grid fingers.

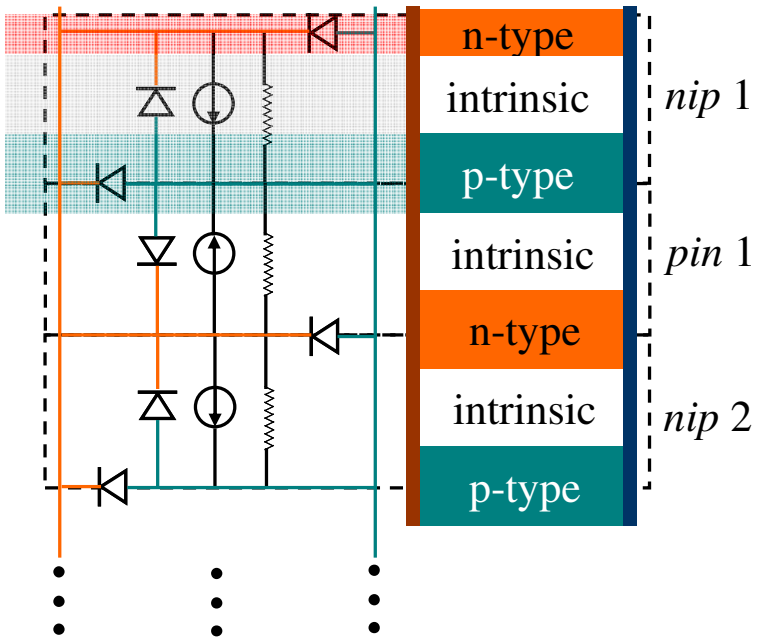

Figure 4.10. Equivalent circuit structure of *nipi*-diode.

4.3 Selective Contacting using Smart Metallization

The process of using smart metallization to achieve selective contacting of the various layers within a *nipi*-diode is critically dependent upon achieving rectifying behavior with layers of dislike polarity and high quality, low contact resistance behavior with layers of like polarity. Although $InGaP_2$ is the intended semiconductor to be used for *nipi*-diodes, the following selective contacting procedure has been performed using GaAs. GaAs is a well characterized semiconductor system and therefore is ideal for prototyping the metallization procedure as un-foreseen issues can more easily be identified and the growth of test structures can be performed more rapidly. Figure 4.11a,b depict the two test structures and metallization used to verify the p-type metallization procedure. As indicated by color, a p-type and an n-type epitaxial layer were grown, lithographically patterned, and metallized using the p-type metallization scheme discussed above (*e.g.*, Au, Zn, Au).

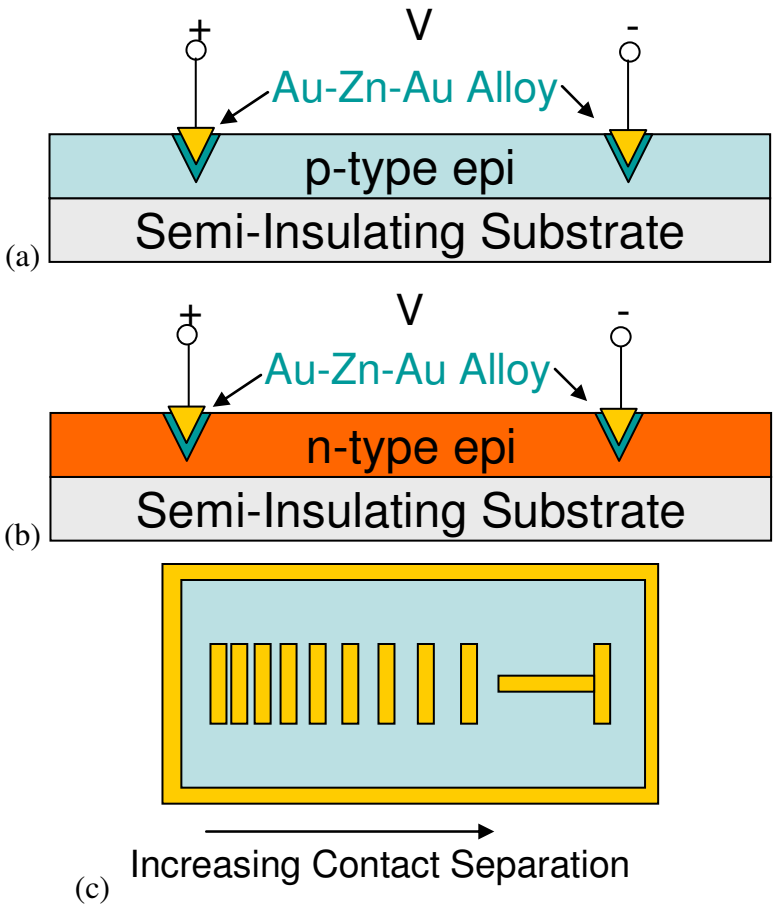

Figure 4.11. (a) Schematic depicting the structure used to test the contact resistance of p-type metallization on a p-type GaAs epitaxial layer, (b) p-type metallization deposited on an n-type epitaxial layer for rectifying contacts, and (c) transmission line measurement test structure used to determine the contact resistance for the p-type metallization on p-type epitaxial layers (and likewise for n-type metallization and n-type epitaxial layers).

As expected, high quality (low resistance) metal contacts were achieved for the p-type metal alloy deposited on the p-type epitaxial layer. Figure 4.12 contains a representative transmission line measurement (TLM) resistance vs. line spacing plot measured for this structure. As the separation between contacts (see Figure 4.11c) is increased, the resistance due to the semiconductor ohmic drop is observed but the contact resistance should remain contestant [78]. A linear fit of the TLM data can be used to determine the contact resistance which is ½ of the y-intercept of the fitted trend line.

From this procedure a contact resistance of about 0.16 Ω was obtained. This result was consistent across the wafer.

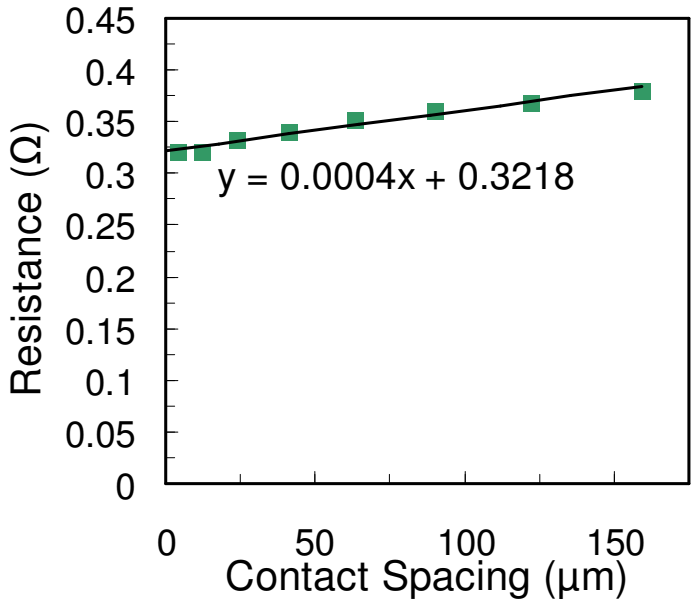

Figure 4.12. Resistance vs. contact spacing for p-type metallization on p-type epitaxial layer measured on TLM structure. The contract resistance was found to be about 0.16 Ω.

The measured current vs. voltage results for one pair of TLM contact pads (junctions) is shown in Figure 4.13. Good rectification is observed in the plot and indicates a high degree of selectivity in the smart metallization approach. The bi-polar nature of the curve results from the dual junctions in series, one formed at each test pad junction (see Figure 4.11b). The results shown here are similar to those obtained for n-type metallization (Ge, Au) on both n-type and p-type epitaxial layers.

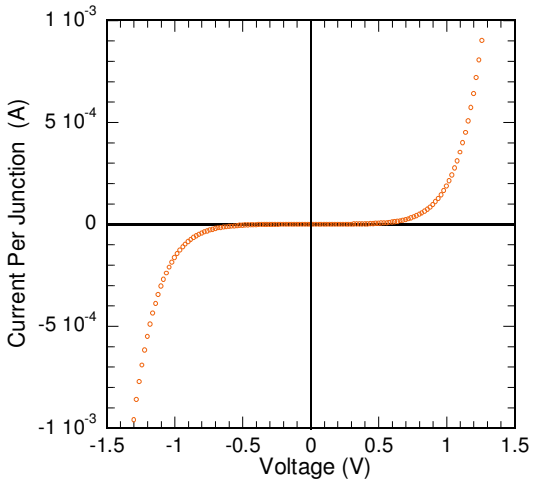

Figure 4.13. (a) First quadrant semi-log plot of the current vs. voltage characterizes for the p-type metallization contacts on n-type epitaxial layer post annealing at 400 °C; (b) contains the full I-V characteristics.

The second major study performed was to determine the proper chemical etching procedure to obtain high quality V-groove trenches within the GaAs epitaxy layers. To accomplish this, a semi-insulating GaAs wafer was lithographically patterned using a grid finger mask. The wafer was then cleaved across the grid fingers and exposed to the selected etching solution for times varying between 1 s and 30 s. The selected etching solution was based on a procedure used by Bailey *et al*. to form three-dimensional GaAs space solar cells [79]. The etching solution consists of sulfuric acid, hydrogen peroxide, and deionized water in a ratio of 4:1:5. When being prepared, the solution rapidly heats to a temperature in excess of 70 °C. This high temperature can potentially cause a rapid increase in etch rate, thereby causing etchant to become diffusion rate limited and no longer form anisotropic trenches. Therefore, the solution was allowed to cool to room temperature before beginning to etch the GaAs.

Figure 4.14a contains cross sectional scanning electron microscope images of the etched V-grooves in GaAs for 1 s, 10 s, and 30 s etch times. The formation of the V-groove is apparent in these images, wherein rapid downward etching is observed in

addition to some undercutting of the photoresist. The orientation of the wafer (*i.e.*, its termination plane or growth direction) and the orientation of the patterned lines are critical in achieving V-grooves structures. The orientation used here is (100) with the grid lines perpendicular to the major flat, or along the <01 $\bar{1}$>. This orientation is critical because anisotropic etching results from the different reactivity of the acid solution between the anion (As) and the cation (Ga). Since the solution reacts faster with As, the Ga terminated (111) and (1 $\bar{1}$ $\bar{1}$) etch at slower than the (100) resulting in the slanted sidewalls observed in the SEM images [80]. The downward etch depth and undercut depth were measured from the SEM images and plotted with respect to time in Figure 4.14b. From the slopes of the line, a ratio of etch depth to undercut depth of approximately 3.3 was obtained.

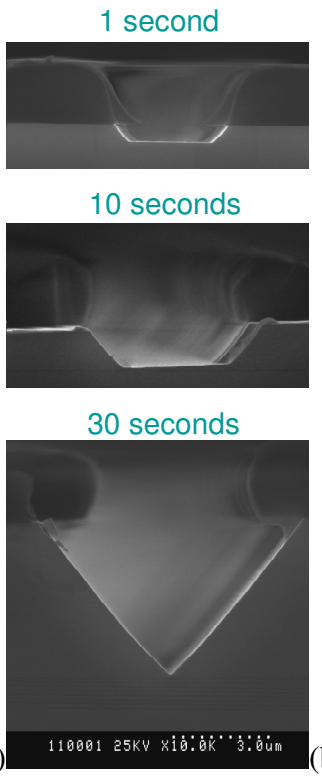

(a)

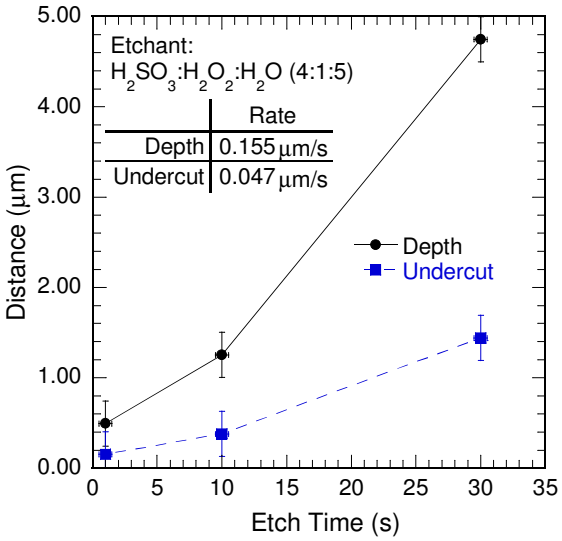

(b)

Figure 4.14. (a) SEM images depicting the formation of the V-grooves with increased chemical etching from 1 s to 30 s. (b) A graph illustrating the total vertical etching depth (black line) and the resist under cutting with increasing etching time.

The mask set design consists of five layers; the general layout is shown in Figure 4.15a. As shown in the figure, twelve 1 cm^2 devices are distributed across the two inch wafer with three sets of etch depth verniers (Figure 4.15b) and contact test pads (Figure 4.15c) in each corner. The etch depth vernier consists of metal layers deposited onto the surface of the wafer during the alignment layer metallization. These pads are left exposed during the V-groove etching process and therefore will peel off once they have been fully undercut. By incrementing the width of the bars in 0.5 μm increments, the number of bars removed provides a rapid means for estimating the etch depth with an accuracy of ~ 1 μm. More importantly, it provides a means for determining if the undercutting exceeds the width of the metal grid lines. The contact test pads contain p-type / p-type, n-type / n-type, and n-type / p-type contacts. These are used to investigate the contact resistance and whether selective contacts have been made to the various layers.

Figure 4.15d contains schematics illustrating the interdigitated fingers of the devices and indicates the spacing used between each layer. The V-groove etching step is the first process after alignment, and then is followed by each metal layer. The V-groove etching cannot be performed during the same lithographic layer (as typically done with single junction solar cells – the etch is used to remove oxides) because the undercutting would shadow the slanting walls of the V-grooves. The width between each layer dictates the distance that majority carriers must diffuse before reaching the contact. Under excitation, charge carrier diffusion in this layer is a result of a majority carrier concentration gradient occurring along the layer since near the contact carriers are swept into the contact by the lateral drift field. There is a tradeoff between grid finger spacing

(concentration gradient) and active surface area which must be optimized to improve performance. In an attempt to investigate this tradeoff, four different grid finger spacing were designed which include separations of 40 µm, 90 µm, 240 µm, and 490 µm.

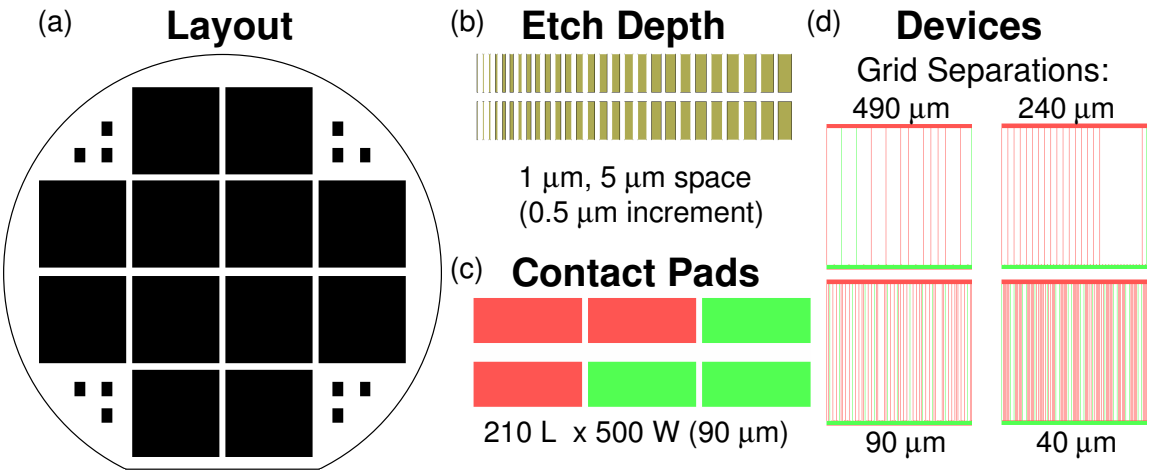

Figure 4.15. Schematics indicating (a) the die layout, (b) the rapid etch-depth vernier, (c) the contact measurement test pads, and (d) the interdigitated metal grid fingers of the 1x1 cm^2 device structures with grid finger spacing ranging from 490 µm to 40 µm.

To validate the *nipi*-diode structure, a triple junction GaAs *nipi*-diode was grown. The layer thicknesses were chosen such that each *nip* and *pin* sub-device was comparable to that of the single junction $InGaP_2$ device measured previously. A schematic depicting the structure of the device, the layer thicknesses, and doping concentration is provided in Figure 4.16. As shown in the figure, the device was grown on semi-insulating GaAs (001) and isolated from the substrate using an $InGaP_2$ back surface field layer which also acts as an etch stop. The first p-type layer and the last n-type layer were 500 nm thick since they are adjacent to only a single layer, while the rest of the doped regions were 1000 nm thick. All intrinsic regions were grown 200 nm thick. Finally, the surface of the device is capped with an $InGaP_2$ "window" layer to passivate surface states thereby reducing the surface recombination velocity in the top n-type layer.

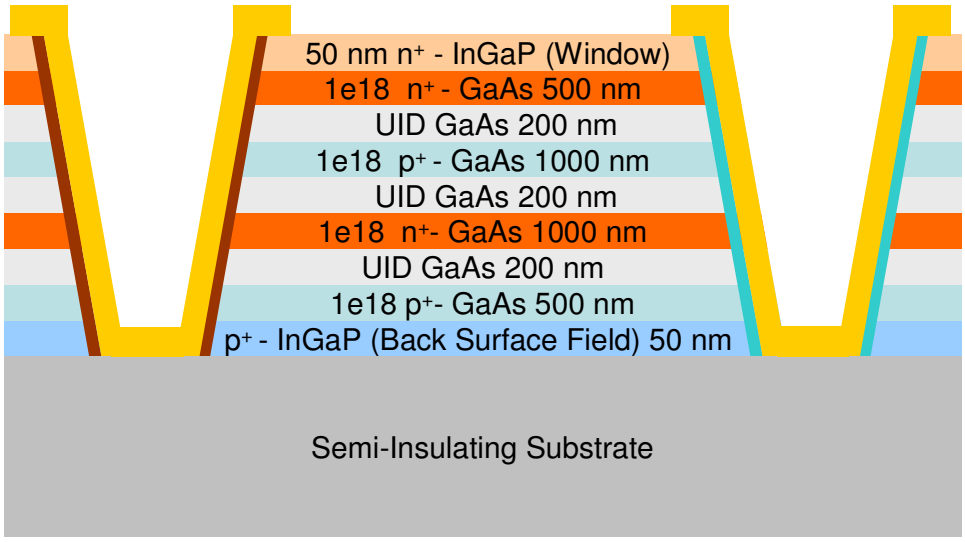

Figure 4.16. Triple junction *nipi*-diode schematic indicating the various layers, doping concentration, and thickness.

Current voltage characterization of the device pre- and post-annealing is provided in Figure 4.17. The plot provided in this figure is for the best device measured which has a grid finger spacing of 90 μm. Prior to annealing, the contact metallization has not been driven-in and therefore at best is providing a Schottky type rectification. However, a very high current (I_{sc} = 19.3 mA/cm^2) and an open circuit voltage of 0.28 V was achieved. Annealing of the device shows evidence of localized compensation as the ideality of the device is increased significantly, the I_{sc} increased to 20.7 mA/cm^2 and the V_{oc} increased to 0.35 V. An AM0 efficiency of 3.17 % was achieved which is significant considering the top-most junction absorbs most of the light. As a result, the photogenerated current by the device must compete against the leakage current at the contacts in addition to the dark current generated in all three diodes.

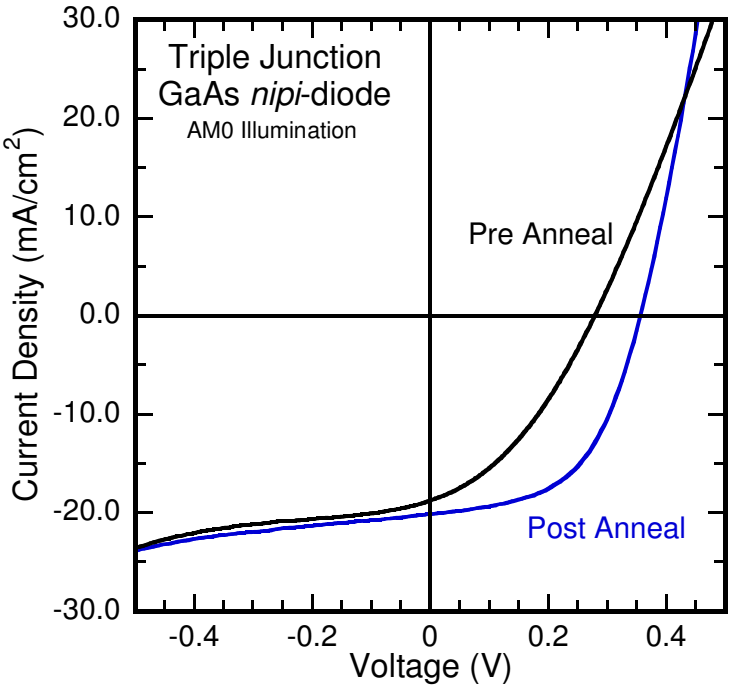

Figure 4.17. Effect of annealing on a *nipi*-diode with 90 µm grid finger spacing AM0 illuminated current vs. voltage characteristics.

The effects of grid finger separation on the illuminated current vs. voltage characteristics can be quickly evidenced in Figure 4.18. In this figure, the best performing device current vs. voltage characteristics for each grid finger separation are overlaid. As the separation is increased from 40 µm to 490 µm, the short circuit current increases as expected (see Figure 4.19). In contrast, the ideality of the devices has the reverse trend, wherein the ideality decreases (*n* increases) with increasing grid finger separation. Based on the slopes of the curves, it is apparent that the ideality loss is a result of series resistance, as large amounts of current is being conducted laterally in the thin layers to the grid fingers. The best performing device has grid finger separations of 90 µm which appears to be balancing these two competing effects. It is important to note that series resistance should not be as large of a problem under excitation by a

radioisotope source since the level of excitation, and hence current output, is much lower. However, shunt resistance is the critical parameter under those conditions.

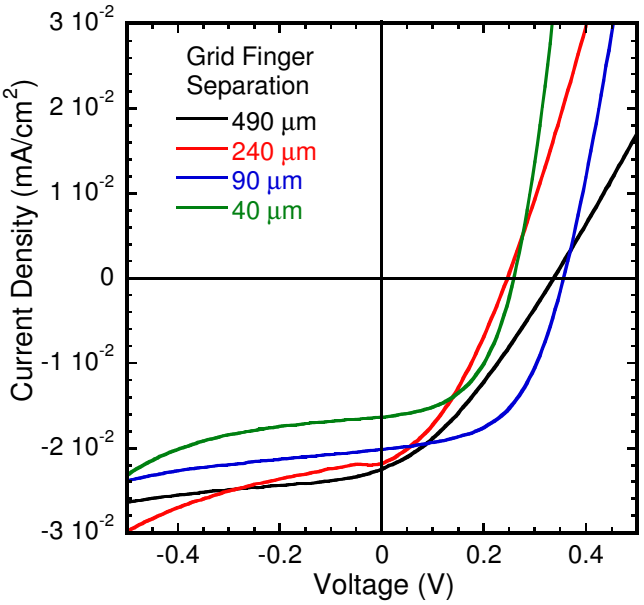

Figure 4.18. Current vs. voltage characteristics for *nipi*-diodes with varying grid finger separations; devices were excited with simulated AM0 illumination.

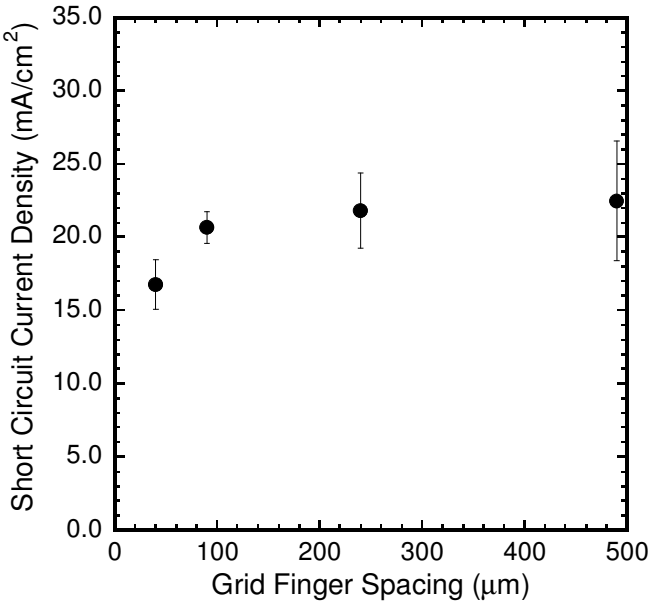

Figure 4.19. Short circuit current density dependence on *nipi*-diode grid finger separation.

When tested under a low intensity alpha-particle source (~0.2 mCi) a short circuit of nearly 1 µA/cm^2 was achieved. However the larger dark current of the GaAs material

(in comparison to $InGaP_2$) resulted in no appreciable open circuit voltage to be obtained. This reinforces the need for a wide bandgap solid-state converter for radioisotope batteries. However, the results presented here clearly demonstrate the potential for achieving power generation from a *nipi*-diode solid state converter.

CHAPTER 5. INDIRECT CONVERSION RADIOISOTOPE BATTERIES

Indirect-drive radioisotope batteries utilize a two state energy conversion process: (1) the kinetic energy of an emitted high energy particle is converted into light via a radioluminescent phosphor; (2) the emitted light is absorbed and converted into electricity by a photodiode. Radioluminescent phosphors, often called intermediate absorbers, may be comprised of semiconducting or insulating materials which emit visible light upon excitation by high energy photons or ionizing radiation. After being exposed to an excitation source (light or nuclear), materials with an electronic bandgap will emit light resulting from the relaxation of excited electrons, *i.e.*, radiative recombination. There are many alternative relaxation pathways that do not result in the emission of light, *i.e.*, non-radiative recombination, typically consisting of lattice vibrations or carrier thermalization. To increase the probability of radiative recombination, dopant ions are incorporated into the lattice of the material. These ions, commonly transition metals or rare-earth elements, have energy states that lie within the bandgap of the material. Upon excitation, electrons of the host material are excited beyond their bandgap and subsequently relax down into one of the excited states of the dopant atom. Radiative recombination then occurs when the excited electron relaxes further to a lower energy state associated with the dopant, emitting a photon in the process.

The photodiode in indirect conversion devices is shielded from the radiation thereby alleviating the radiation-induced degradation; this is the main advantage of the indirect-drive approach. However, damage may still occur in the phosphor material

resulting in lower photon output although this rate of damage is typically much lower [13]. The reduction in degradation rate comes at the price of reduced efficiency since an additional energy conversion process is required. Proper energy matching between the emission energy of the radioluminescent phosphor and the bandgap energy of the photovoltaic converter can minimize this loss. Monochromatic external quantum efficiencies of >60% can be achieved in $InGaP_2$ photovoltaic devices, making the radioluminescent efficiency of the phosphor the limiting component of the device.

In general, bulk phosphors and semiconducting materials have demonstrated the ability to photo- and radioluminesce with good efficiency (e.g., 20%-25%); however, the radiation tolerance of these materials is inadequate for long-life radioisotope battery operation [13]. To achieve both enhanced radioluminescent output and radiation tolerance, the strategic approach of this research has been the development of rad-hard radioluminescent quantum dots (QD), also referred to as nanophosphors or nanomaterials, to serve as the intermediate absorber (see Figure 5.1) [81]. The use of these materials has been motivated by recent reports demonstrating a greater radiation tolerance by nanomaterials as compared to their bulk counterpart [82-84]. The nanomaterials that have been investigated include inorganic nanophosphors and doped colloidal QDs which are nanocrystalline semiconductor particles.

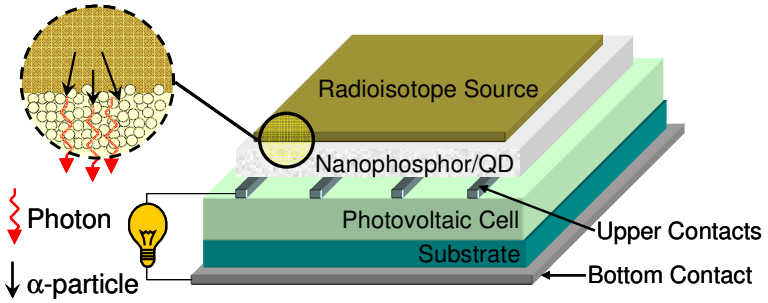

Figure 5.1. Schematic depicting the structure of an indirect-drive radioisotope battery.

5.1 DEVICE COMPONENT OVERVIEW

As indicated above the radioisotope battery may be sectioned into two primary components, the radioluminescent QD thin film, and the photovoltaic cell. The key aspects of the radioluminescent QD thin film include the elemental constituents of the nanomaterials, the dopant incorporated into the nanomaterials, and the physical properties of the deposited thin film (e.g., particle size, thickness, uniformity, etc.). In regards to the photovoltaic cell, the key features which have been considered include the bandgap, efficiency, spectral responsivity, low-intensity light response, and radiation tolerance. The following two subsections provide an overview of these key component characteristics.

5.1.1 Radioluminescent Nanomaterials

Bulk phosphors, comprised of mainly doped inorganic crystals, have been extensively used in radiation detection, fluorescent lighting, cathode ray tube displays, etc., and have demonstrated nuclear-to-light efficiencies approaching 25% for select materials [85]. The rate of degradation of these materials is expected to be slower than that of the photovoltaic cells used to convert the radioluminescent emission. It has been the goal of this research to investigate the effect size has on both the radiation tolerance and the radioluminescent efficiency of the nanophosphors.

Radioluminescence in inorganic crystalline phosphor materials occurs via donor-acceptor pair recombination or rare-earth dopant ion-center recombination. In the latter, rare-earth dopant ions are incorporated into the inorganic crystal thereby introducing electronic energy levels that are situated within the large bandgap (typically 3.5 – 6.5 eV) of the inorganic crystal. Luminescence occurs when excited electrons transition between

these dopant energy levels. Figure 5.2 depicts the energy levels of 13 rare-earth elements [86]. The energy of the levels (in cm^{-1}) is plotted with respect to the ground state which is dependent on the crystal structure of the matrix material ($LaCl_3$ in Figure 5.2). In contrast, the energy of the emission depends on the energy difference between the two states that the excited electron transitions between. This transition is nearly independent of the environment provided the site symmetry of dopant ion is preserved, and therefore similar emission spectra may be obtained from the same dopant ion situated in different hosts [87].

The commonality between the rare-earth elements depicted above is their partially filled 4f electronic orbitals. Long-lived excited states are a consequence of shielding by the electrons occupying the 5p, 6s, and 6p orbits, which exist at slightly lower energies than the 4f electrons but have larger average orbital radii [88]. Though many excited states may be populated, electronic transitions are predominately due to electric dipole or magnetic dipole interactions [87]. Moreover, many transitions, such as 4f-4f electric dipole transitions, are parity forbidden and therefore will not occur unless there is substantial interaction with the host material.

Not all transitions result in the emission of light, non-radiative transitions may occur in which phonons are generated. The energy levels which have the greatest probability of a radiative transition contain a semi-circle in Figure 5.2. To model the energy levels and radiative transition probabilities, ligand field theory and Judd-Ofelt theory have been used, respectively [87]. The maximum efficiency of a phosphor under irradiation is dictated by the probability of photon emission and the difference in energy between the bandgap of the matrix material and the energy of the transition.

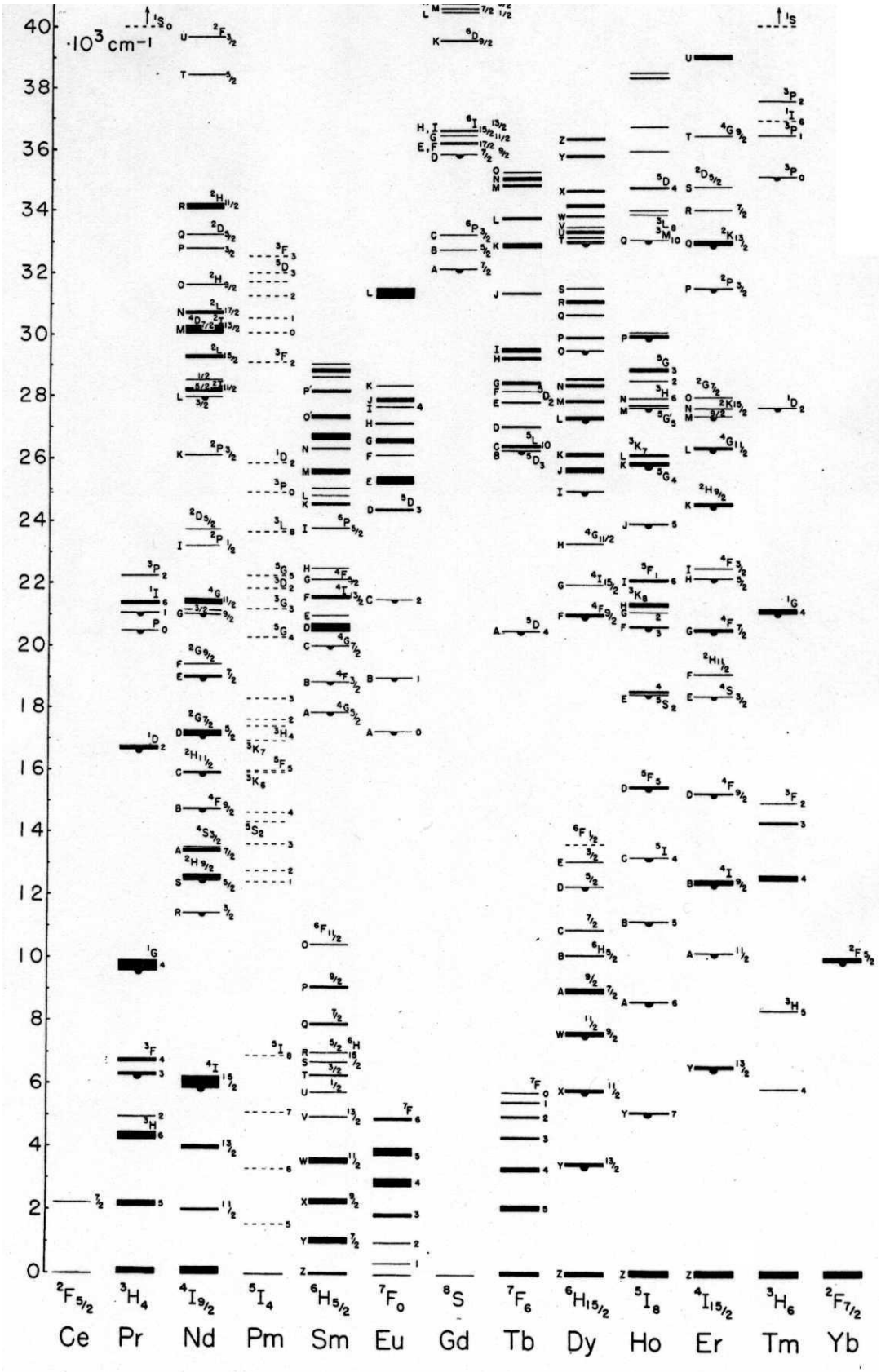

Figure 5.2. Dieke diagram depicting the energy levels of trivalent lanthanide ions [86].

In the case of $Y_2O_3:Eu^{3+}$ the bandgap of yttria is ~6 eV while the emission energy peaks at approximately 2 eV. Even with a 100% probability of radiative recombination, the maximum efficiency of the material is limited to 33% due to the large down-shift in energy from 6 eV to 2 eV. Increasing the efficiency of the phosphor materials may be achieved by using alternative host matrices that have a narrower bandgap (*i.e.*, semiconductors).

Donor-acceptor pair recombination is the primary form of radiative recombination in ZnS based phosphors. In this material system, the ionized levels of the Zn^{2+} atom form the conduction band while the valence band is formed by the S^{2-} atoms. Excited electrons associated with the Zn^{2+} atom (donor) recombine with a hole in the valence band associated with the S^{2-} atom (acceptor), emitting light in the process. To increase the efficiency of this process, dopant atoms (e.g., Ag^{2+}) which have energy levels slightly below the Zn^{2+} conduction band level can be incorporated into the crystal. The incorporated dopant will trap the conduction electrons and recombination will result between the electron occupying this state and a hole in the valence band. This process is illustrated in Figure 5.3. In order for an interaction to occur, the wavevectors of both the electron and hole need to align to conserve momentum. However, electrons and holes can migrate throughout their respective bands and interactions between donors and acceptors over 500 Å apart have been reported [85].

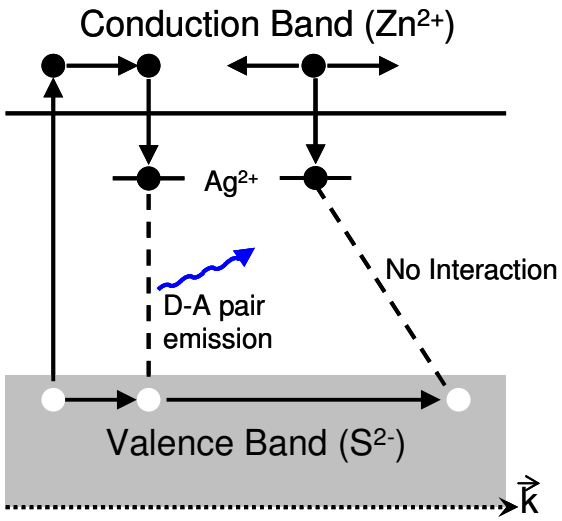

Figure 5.3. Schematic of a D-A pair recombination center and a non-interaction D and A center.

In the development of an indirect conversion radioisotope battery, nanophosphors comprised of various bulk matrices and dopants have been fabricated. Figure 5.4 contains a digital photograph of four such inorganic nanophosphors including, ZnS:Ag^{2+}, Y_2O_3:Tb^{3+}, YAG:Ce^{3+} (yttrium aluminum garnet), and Y_2O_3:Eu^{3+} under excitation by a 254 nm light source along with their radioluminescence spectra under irradiation with a 0.5 mCi ^{210}Po source which emits ~4.2 MeV alpha particles. The narrow emission lines in the rare-earth doped phosphors are indicative of the discrete electronic transitions of the associated dopant. In contrast, the ZnS:Ag^{2+} has a broader emission which is related to the donor-acceptor mechanism wherein the slight mismatch in wavevectors requires a phonon to be generated in the process to conserve momentum [85]. This figure illustrates the wide range of emission energies that are obtainable through the use of different crystalline moieties and dopants.

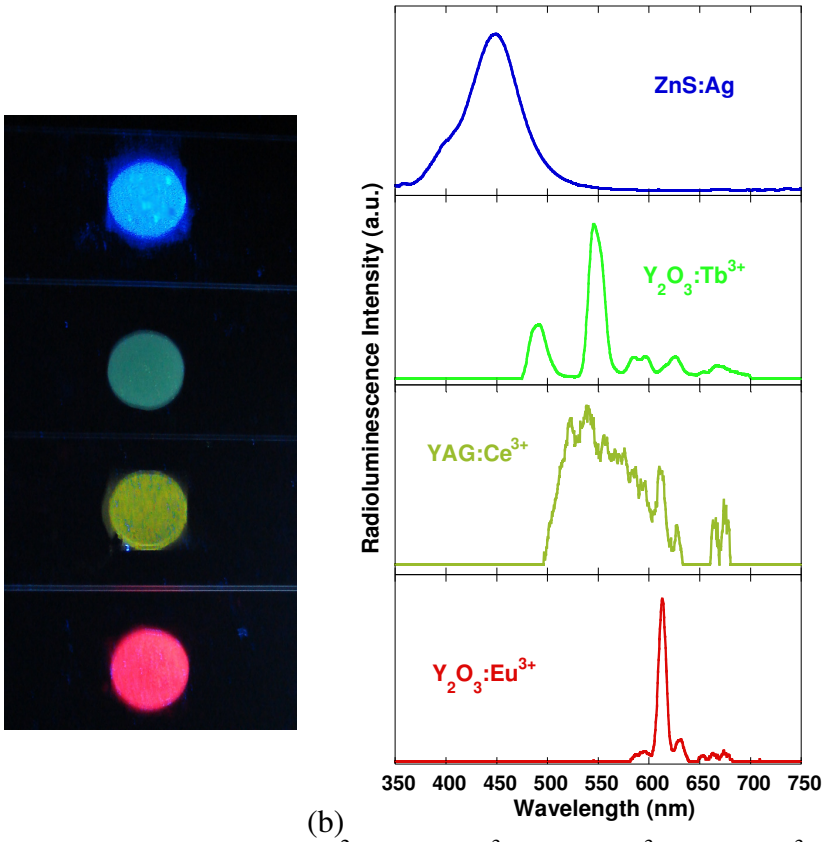

(a) (b)

Figure 5.4. (a) Digital image of ZnS:Ag^{2+}, Y_2O_3:Tb^{3+}, YAG:Ce^{3+}, Y_2O_3:Eu^{3+}, under 254 nm excitation, and (b) radioluminescence spectra of the associated phosphors under irradiation by a 0.1 mCi ^{210}Po alpha-particle source.

The other material systems that have been investigated for use as the intermediate absorber are colloidally synthesized quantum dots. As shown in Figure 5.5, the energy levels of QDs can be approximated using the quantum mechanical particle-in-a-box model. As discussed in Chapter 2, once the size of the nanocrystalline semiconductor material becomes equal to or smaller than the Bohr exciton radius, the electron and hole wavefunctions begin to overlap resulting in an increased electronic bandgap. This property enables the bandgap of a single material to vary from the bulk bandgap throughout most of the visible spectrum (Figure 5.5b). The photon quantum yield of colloidal QDs has been shown to be extremely high (e.g., 85% [89]). The primary

mechanism of luminescence is similar to the donor-acceptor model wherein the excited electron in the conduction band recombines with a hole in the valence band.

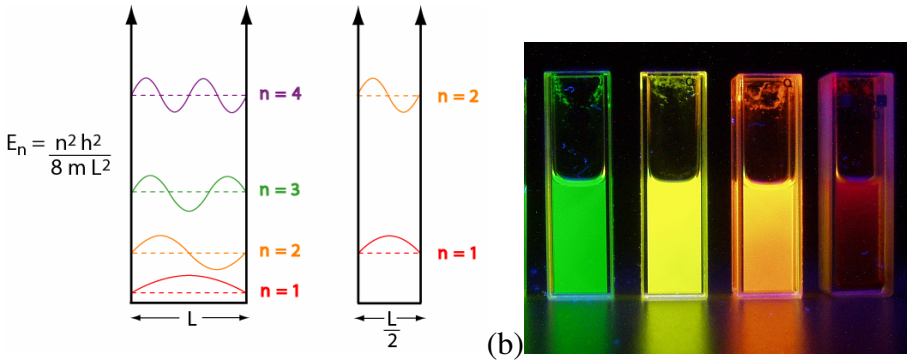

Figure 5.5. (a) Schematic depicting the difference in energy of electronic states for boxes of differing sizes, and (b) photoluminescence of CdSe QDs under 254 nm excitation. Reproduced with permission of Brian J. Landi [90].

It is also possible to dope QDs with either transition metals or rare-earth elements. Depending on the choice of dopant ion, an enhanced donor-acceptor type luminescence or a rare-earth ion luminescence may result. One novelty of a doped QD dot approach is the ability to vary the bandgap of the material in relation to the energy levels of a rare-earth dopant ion. Provided proper ionization potential matching between the valence band of the QDs and the ground state of rare-earth dopant ion, the conduction band of the QD may be varied with respect to the excited states of the rare-earth dopant atom. In Figure 5.6 the valence and conduction bands of the QDs are depicted by colored boxes while the electronic excited states of the rare-earth dopant ions are depicted by the thin lines as shown in the Dieke diagram (Figure 5.2). Figure 5.6a is representative of the inorganic nanophosphors where the bandgap is greater than the excited electron states of the dopant atoms. Excitation of the material is primary through electronic transitions within the matrix material the excited electron is then transferred to the dopant ion. Figure 5.6b depicts a situation in which highly excited states of the rare-earth ion (2-3 eV greater than the ground state) are matched in energy with the conduction band of the QD.

Electronic coupling between the QD energy levels and the dopant excited states have been investigated to achieve a greater probability of energy transition from the QD to the rare-earth dopant leading to a higher light output. The ability to tune the bandgap of QDs by varying their size makes this energy matching scheme possible.

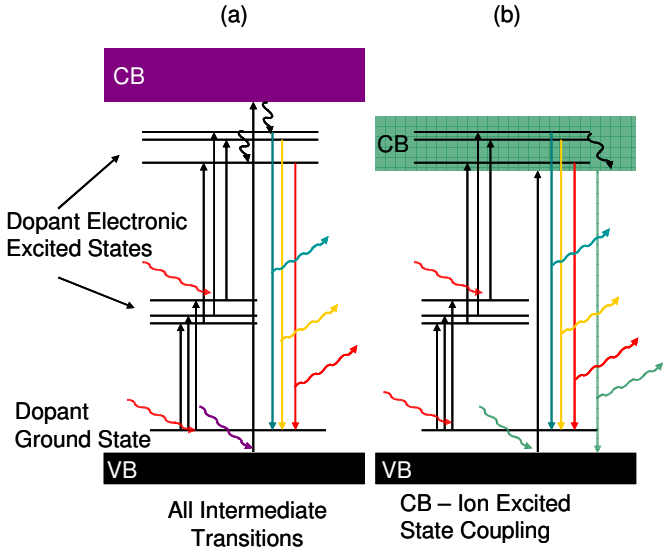

Figure 5.6. Energy level diagram depicting the possible energy level mapping schemes which may result in QDs doped with rare-earth ions. The solid arrows in the figure correspond to electronic transitions; black upward facing arrows are excitations while colored facing downward arrows are relaxations which result in photon emissions. Downward facing colored wave-like arrows are excitation photons while the upward facing arrows are emissions. Black wave-like arrows are symbolic of phonons.

In addition to developing the materials which comprise the radioluminescent QD layer, the physical properties of the thin-film will have a strong influence on the radioluminescent power output. As shown in Figure 5.7, the thickness of the thin film must be designed such that alpha-particle energy absorption is maximized and self-absorption and scattering of emitted photons by the thin-film is minimized. Since there is an optimal layer thickness, it is imperative that uniform thin-films are synthesized to ensure uniform illumination over the entire device. Coupled with these challenges is the variation in alpha-energy absorption and self-absorption/scattering which may vary with

respect to the particle size, chemical composition, packing density, and dopant concentration of the QDs within the film.

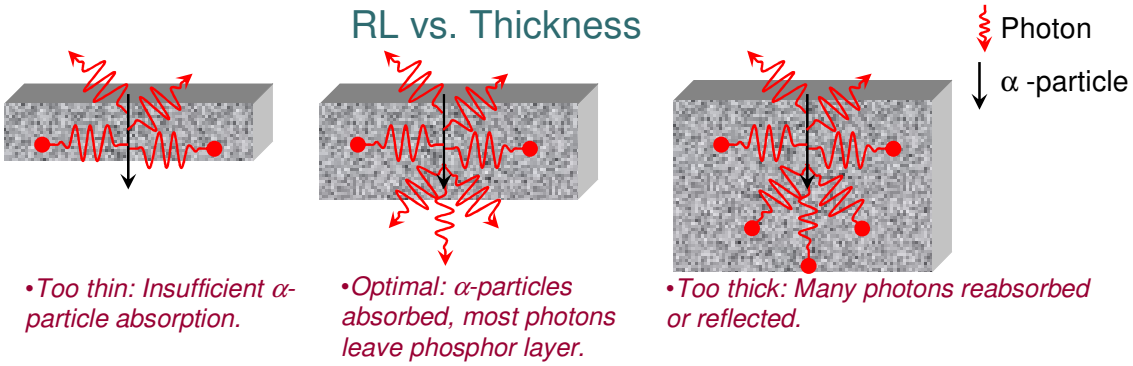

Figure 5.7. Schematic depicting affects of film thickness on alpha-particle energy absorption and self-absorption / scattering.

5.1.2 $InGaP_2$ Photovoltaic Converters

The final configuration of the indirect conversion radioisotope incorporates the radioluminescent nanophosphor deposited as a thin film over an $InGaP_2$ photovoltaic cell that is optimized for low-light conversion. $InGaP_2$ was chosen for this application because its wideband gap allows for suppression of saturation current, something that competes with power generation especially under low intensity illumination. In general, the saturation current j_o is proportional to the intrinsic carrier concentration n_i of the material, which in turn, is exponentially dependant on the material bandgap E_g. Therefore, a wide bandgap material will exhibit a lower dark current.

In addition to the properties inherent to wideband semiconductors, the lattice spacing of $InGaP_2$ is well matched to GaAs enabling $InGaP_2$ photovoltaic diodes to be epitaxially grown on GaAs substrates using organo-metallic vapor phase epitaxy (OMVPE). Advances in the OMVPE growth of this materials system, accelerated by the space photovoltaics industry, have made it possible to grow low-defect and high-efficiency $InGaP_2$ photovoltaic cells.

5.2 DEVICE FABRICATION

5.2.1 Quantum Dot / Nanophosphor Synthesis

Rare-earth doped Y_2O_3 (yttria) is a model phosphor system known for both high efficiency and radiation tolerance [87]. This has been the primary material system investigated in this research. To synthesize Y_2O_3 doped with various rare-earth elements, an ethylenediaminetetraacetic acid (EDTA) assisted UREA precipitation technique was employed. Typical synthetic procedures are as follows. Ten grams of of Y_2O_3 and a stoichiometric amount of a rare-earth element in oxide form (RE_2O_3) are dissolved in 19 mL of concentrated nitric acid and 81 mL deionized H_2O resulting in an aqueous solution of $Y_{2-x}RE_x(NO_3)_3$ with a pH of ~1. Twelve mL of this stock solution is then diluted 25x in deionized H_2O and 15 g of UREA is added. Depending on the desired crystal size, 0-1.0 g of EDTA is added to the solution, after which the solution is stirred and refluxed for 1 hour. The solution is then filtered using a 0.02 μm anodisc alumina filter, rinsed 3x with H_2O, and dried in vacuo at 80° C. After drying, a fine white powder results, which is crushed with a mortal-and-pestle and fired at 1100° C in air. Figure 5.8 contains SEM images of Y_2O_3 doped with Er^{3+}; the size of the particles was controlled by the amount of EDTA used during synthesis, more EDTA results in smaller particles.

(a) 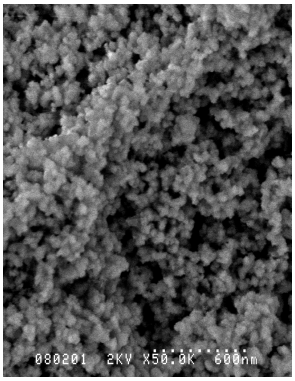

(b) 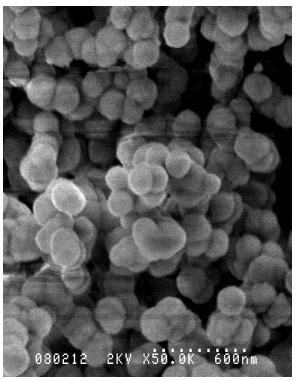

(c) 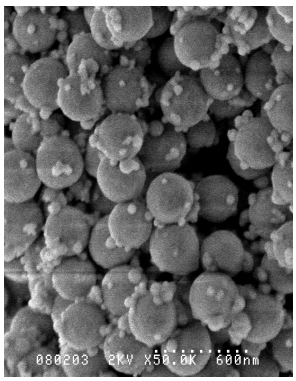

Figure 5.8. SEM images of $Y_2O_3:Er^{3+}$ synthesized by the UREA precipitation technique. Variable sizes were obtained by varying the EDTA concentration during synthesis; the smallest particles had the largest concentration.

A high-temperature processing procedure was used to synthesize rare-earth doped yttria aluminum garnet (YAG), $Y_3Al_2(AlO_4)_3$, nanophosphors. Five grams of YAG nanocrystals (Sigma-Aldrich, 20-30 nm analyzed by BET) was physically mixed with a stoichiometric amount of a nanocrystalline rare-earth oxide, RE_2O_3 (Sigma-Aldrich, 20-30 nm analyzed by BET), where RE= Ce^{3+}, Tb^{3+}, Eu^{3+}, and 20% w/w barium fluoride (BaF_2) as a flux. This mixture was then fired for 5 hours at 1200° C. To remove excess BaF_2, the resultant powder was stirred in 100 mL of a 1 M nitric acid solution for 30 min. The powder was filtered, rinsed, and dried as described above. This process was repeated (except that no additional RE_2O_3 was added) until the peak radioluminescence intensity reached a steady value.

Laser synthesis of bulk and nanocrystalline materials was invested as a means to further reduce the material size. Targets of the desired material were prepared via mechanical pressing at 15,000 psi. The targets were then placed in the center zone of a three stage tube furnace. The surface of the target was rastered by a pulsed alexandrite laser resulting in a deposit of nanocrystalline material along the inner wall of the quartz tube. A digital image of the laser synthesis reactor is provided below.

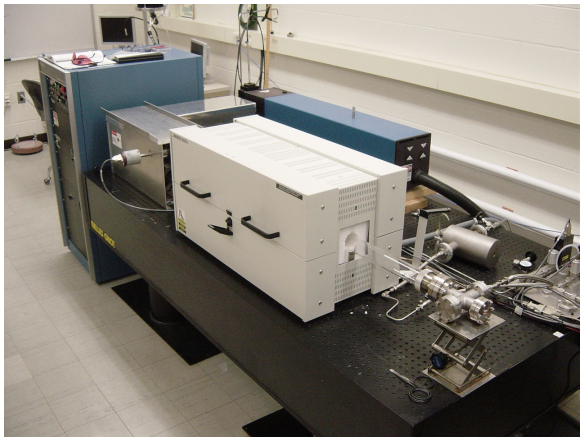

Figure 5.9. Alexandrite laser deposition reactor.

Synthesis of various moieties of QDs have been reported in the literature [91-95], many of which were synthesized as a part of this research. The synthesis of CdSe colloidal nanocrystals is based on the previous work using cadmium oxide (CdO) instead of dimethyl cadium as the cadmium source. The procedure is performed on a standard shlenk line under argon, whereby CdO is dissolved in a mixture of stearic acid and octadecene (ODE) at 200 °C, producing a solution of cadmium stearate. The solution is cooled to room temperature and a mixture of octadecylamine and trioctylphosphine oxide (TOPO) are added to control growth, enable selective solubility, and for QD surface passivation. The reaction solution is re-heated to 280 °C and a solution of selenium dissolved in trioctylphosphine and ODE is injected and reacted for a select time period. Typically, these reactions produce CdSe QDs with nanocrystal diameters of ~ 3 – 4 nm. The reaction time and cooling rate (rapid quench vs. a slow cool down) can drastically affect the size and quality of the nanocrystals. Purification of the as-synthesized CdSe QDs is required to remove excess ligands and reaction by-products. The chemical extraction that was reported to be most efficient for this reaction scheme used a mixture of methanol and hexanes [85]. The polarity of the methanol preferentially removes the impurities, while the nonpolar hexanes solubilizes the TOPO-capped QDs.

Many QD samples comprised of group III – group V (III-V) semiconductors were also synthesized throughout the development of an indirect conversion radioisotope battery. InP photodiodes has been shown to be extremely radiation tolerant because of its ability to self-anneal at room temperature [17]. Additionally, the primary valence state of most rare-earth ions is 3^+, making the prospect of doping III-V QDs more feasible than II-VI semiconductors. The synthesis procedure that was employed to synthesize InP and rare-earth doped InP QDs is a reverse micellular approach (which is applicable for synthesis of GaP, InAs, and GaAs). Synthesis is initiated by preparing an indium (cation) precursor solution containing 0.1 mM of indium (III) acetate, 68 mg of myristic acid, and 3 mL of octadecene (ODE) in a triple neck flask. This solution is evacuated and heated to 110°C for 2 hours to remove any O_2 or H_2O from the reaction. Following this step, the solution is pumped and purged (Ar) 3x and heated to the injection temperature (between 250-300°C). In an inert glove box, the phosphorus (anion) precursor solution containing 0.05 mM of tris trimethylsilyl phosphine $P(TMS)_3$ mixed in 2 mL of ODE is prepared and added to an injection syringe. Once the indium solution reaches the desired injection temperature, the $P(TMS)_3$ solution is removed from the gloved box and quickly injected. Upon injection the clear solution quickly changes color, first becoming yellow and quickly changing to a deep red. The solution is stirred for 1-30 min at approximately 270° C. To purify the material and remove the excess myristic acid, ODE, and In^{3+} ions, the solution is transferred to a separatory funnel where the QDs are repeatedly crashed out of solution using methanol and acetone, and re-suspended using hexanes. To dope the nanocrystals, a stoichiometric amount of RE(III) nitrate is introduced into the indium (cation) precursor solution during synthesis.

The radioluminescent output of the synthesized intermediate absorber (either nanophosphor or doped colloidal QDs) deposited onto the $InGaP_2$ photodiode requires precise thickness control and repeatability. Deposition techniques that have been investigated include drop casting, centrifugation, electrophoretic deposition, spin coating, and spray deposition. The spray deposition technique consists of dispersing a nanophosphor material in a low boiling point solvent and spraying it using an air gun directly onto the device. To enhance adhesion and robustness of the thin-film, polymethylmethacrylate (PMMA) 1-5% w/w is also dissolved in the spray solution. To enable thin-film characterization, (*e.g.*, radioluminescence spectroscopy, optical transmission spectroscopy, and contact profilometry) the spay depositions were performed on glass/quartz slides.

5.2.2 $InGaP_2$ Photovoltaic Converters

$InGaP_2$ devices were epitaxially grown using a Veeco D125LDM OMVPE system. Trimethyl gallium, trimethyl indium, and phosphine were used for the primary constituents, while disilane and diethyl zinc were used for the n-type and p-type dopants, respectively. The ratio of column V elements to column III elements was 60, and the devices were grown on p-type (Zn doped) GaAs substrates oriented (100) and off-cut 6° toward the <111> direction. The reactor vessel was held at 620° C and a growth rate of 5 Å s^{-1} was used.

Post growth processing was initiated by spin coating a 3 μm layer of Microposit® SC-1827 photoresist onto the epitaxy layer for chemical passivation. Any incidental OMVPE-deposited material was removed from the back side of the wafers via alternating 30 second etches in concentrated HCl and a solution of hydrogen peroxide, phosphoric

acid, and water (4:3:1 by volume), and repeated (3x). After the chemical etch, ohmic contacts were deposited on the exposed p-type substrate by thermal evaporation of 200 Å Au, 200 Å Zn, and 2 µm Au, using a CHA Industries thermal evaporator at a base pressure < 5×10-6 torr. Four layers of LOR 5A (Lift-Off-Resist Microposit®) was spun onto the front side and hardened by heating for 5 min at 170° C. An additional layer of photo-active resist SC-1813 was then spun on top, patterned using a Karl Suss contact exposure tool, and subsequently developed using DC-26 developer. To LOR is non-photoactive and is isotropically etched by DC-26 thereby forming an under-cut in the patterned resist as shown in Figure 5.10a. The undercut creates a break in the thermally deposited metal contact layer making the photoresist accessible to the lift-off solution. Following a 5 second HCl etch, the front side metal-ohmic contacts were deposited by evaporating 200 Å Ge, and 1 µm Au (see Figure 5.10b). Photoresist lift-off was performed by etching the LOR layer with nanoRemover PG (~ 3 hr). The final contact anneal was performed at 400 °C for 5 minutes in Ar.

(a)

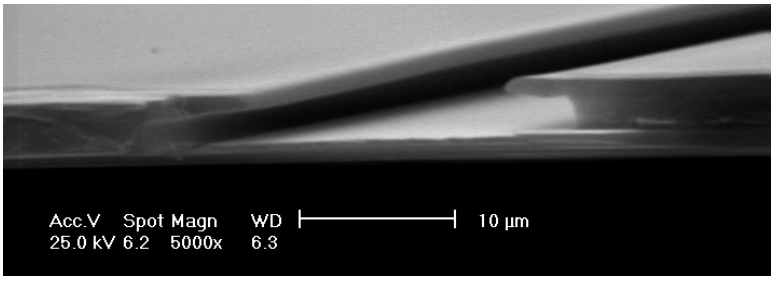

(b)

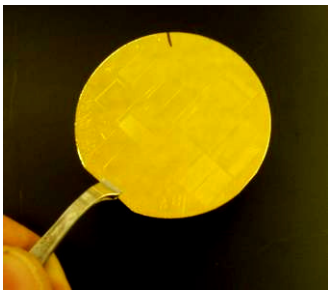

Figure 5.10. (a) Cross-sectional SEM image illustrating the undercutting obtained by using LOR coated with SC-1813, and (b), digital image of a patterned 2-inch $InGaP_2$/GaAs wafer after thermal deposition of top contact metal.

5.3 RESULTS

5.3.1 Radioluminescent Thin-Films

A variety of characterization and spectroscopic measurements were performed on the as-produced QDs and QD thin-films, alike. The luminescent power output of the materials under both photo excitation and alpha-particle irradiation were performed. Transmission spectroscopy and photoluminescence spectroscopy of the materials were performed using a Perkin Elmer lambda 900 spectrometer, and a Jobin Yvon LabRAM Olympus BX41 spectrum analyzer, respectively. To measure the uniformity and the thickness of the intermediate absorber layers, contact profilometry was employed and correlated to the transmission spectroscopy data. Additionally, scanning electron microscopy (SEM) of the materials was performed to determine the approximate particle size (see Figure 5.8) of the nanoparticles.

To measure the radioluminescence intensity of an intermediate absorber layer under excitation by an alpha (beta)-particle source, the test configuration fixture shown in Figure 5.11 was used. In this configuration, the alpha-particle source is held 4 mm from the radioluminescent phosphor which is shown as a thin light blue rectangle in the figure. The phosphor emission is fiber coupled to a high resolution 2048 diode array spectral radiometer (Ocean Optics). Calibration of the spectral radiometer is accomplished via a NIST traceable halogen lamp. To eliminate the variance associated with the temperature dependant sensitivity of the diode array, the radiometer is operated within a refrigerator maintained at ~1° C. Radiation degradation measurements of the thin-films were also performed using this fixture wherein periodic measurements were obtained on a thin-film which is held under constant alpha-particle irradiation.

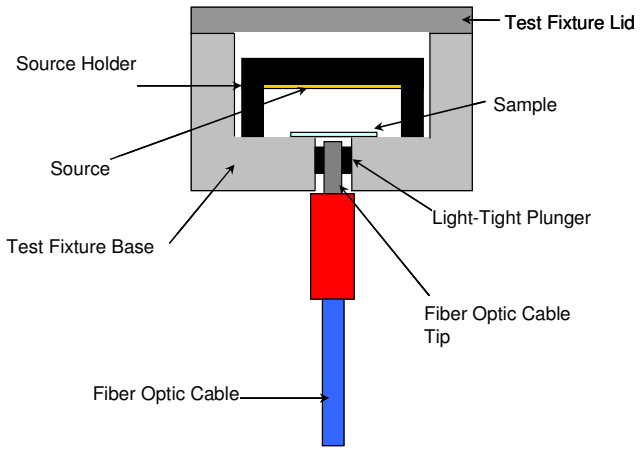

Figure 5.11. Test fixture/configuration for measuring the radioluminescent power output of the thin-film intermediate absorber layers deposited on quartz.

5.3.2 CdSe QDs

Characterization using optical absorption spectroscopy is commonly employed to evaluate the QD diameter distribution based on the first excitonic peak. The progressive shift in absorption as a function of QD size is consistent with the theoretical work on quantum confinement in nanoparticles [96, 97]. Shown in Figure 5.12 is an overlay of four CdSe QD samples with diameters ranging from ~2.5 – 4.2 nm, based on empirical calculations [85]. The absorption wavelength is shown to experimentally shift within a 75 nm "window" with < 2 nm particle size variation.

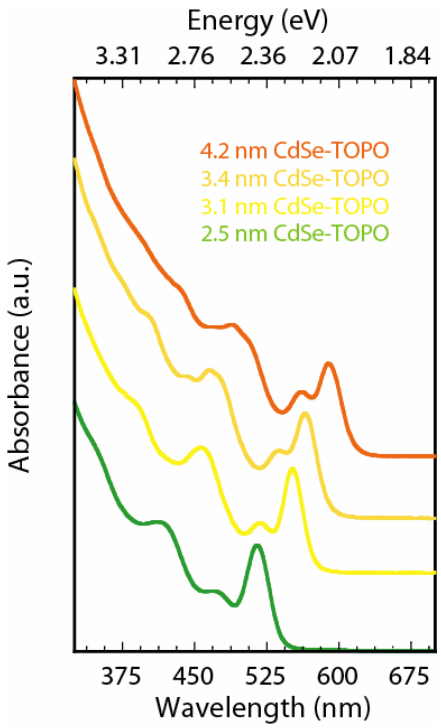

Figure 5.12. Optical absorption spectra for four different size distributions of CdSe-TOPO QDs in a hexanes solution. Reprinted with permission by Brian J. Landi [90].

In addition to absorption, CdSe QDs have a very pronounced fluorescence emission. The simplest visualization of this effect can be observed when QD samples are illuminated by a UV light source. Figure 5.13 shows three CdSe QD samples (diameters of 2.5, 3.1, and 4.2 nm) under (a) ambient room light and (b) 254 nm illumination with a UV lamp. The bright emission of each sample is characteristic of the optical bandgap for the QDs, which directly relates to their diameter. Figure 5.13c contains the fluorescence spectra for the three samples illustrating the spectral shift with emission color.

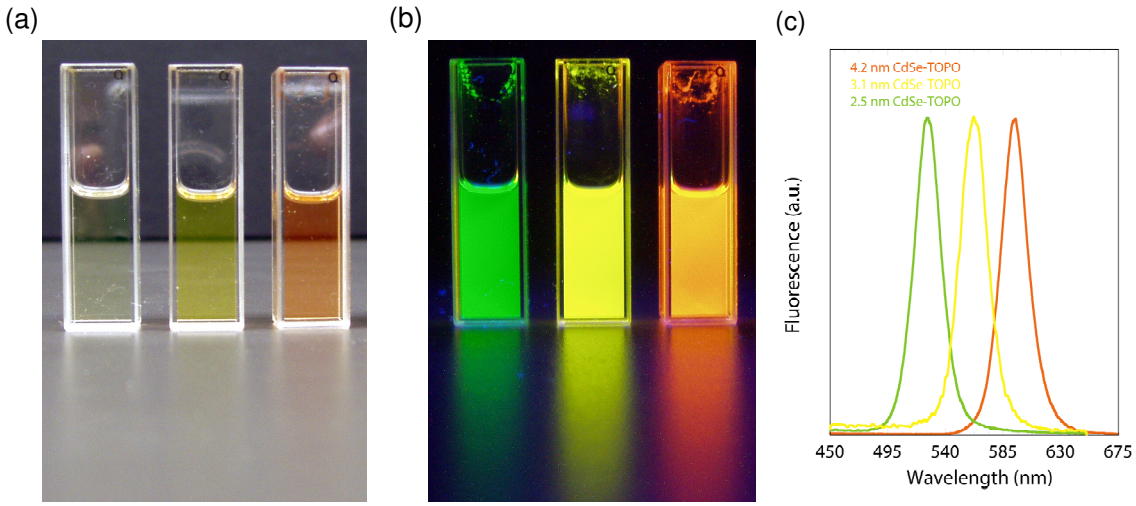

Figure 5.13. Images of CdSe QDs under (a) ambient room light and (b) 254 nm illumination with a UV lamp. (c) Fluorescence spectra for CdSe-TOPO QD samples in hexanes showing the size-dependent optical bandgap. Reprinted with permission of Brian J. Landi [90].

Radioluminescence spectroscopy was performed on CdSe thin-films comprised of the materials shown above, using a ~1 mCi ^{210}Po alpha-particle source emitting 4.2 MeV alpha-particles. Samples were prepared by spray deposition from solutions of hexanes and chloroform; no PMMA was required for adhesion. CdSe QDs are highly air sensitive and clearly oxidized after being deposited onto the quartz slides. Oxidation could be visibly observed by a pronounced color change, from bright red to rusty-brown in hue (*i.e.*, the color of CdO), shortly after the films were deposited. Additionally, the fluorescence signature from the thin-films (under 254 nm optical excitation) was quenched after preparing the thin-film. As a result, no measurable radioluminescence (RL) was observed from any of the CdSe samples prepared.

5.3.3 InP QDs

Characterization, including optical absorption, fluorescence spectroscopy, and radioluminescence spectroscopy for the InP QDs synthesized in this research followed in

the same manner as that of the CdSe QDs. Figure 5.14 contains an overlay of the optical absorption and fluorescence for an InP QD sample. The resolved 1st excitonic peak is indicative of strong quantum confinement, while the bimodal fluorescence spectra is a result of band-to-band emission (λ = 619 nm) and surface defect emission (λ=674 nm) which has also been observed in the literature [95]. The effect of reaction time and temperature was investigated through a series of reactions in an effort to optimize the InP QD optical properties. Qualitatively, temperature had the largest impact on the resultant fluorescence peak maximum (QD size), whereas the time of the reaction had a large impact on the FWHM (QD monodispersity) and reduction of the second fluorescence peak (QD defects). The spectra shown in the figure below represent the highest quality QDs synthesized and are consistent with data presented in the literature [95].

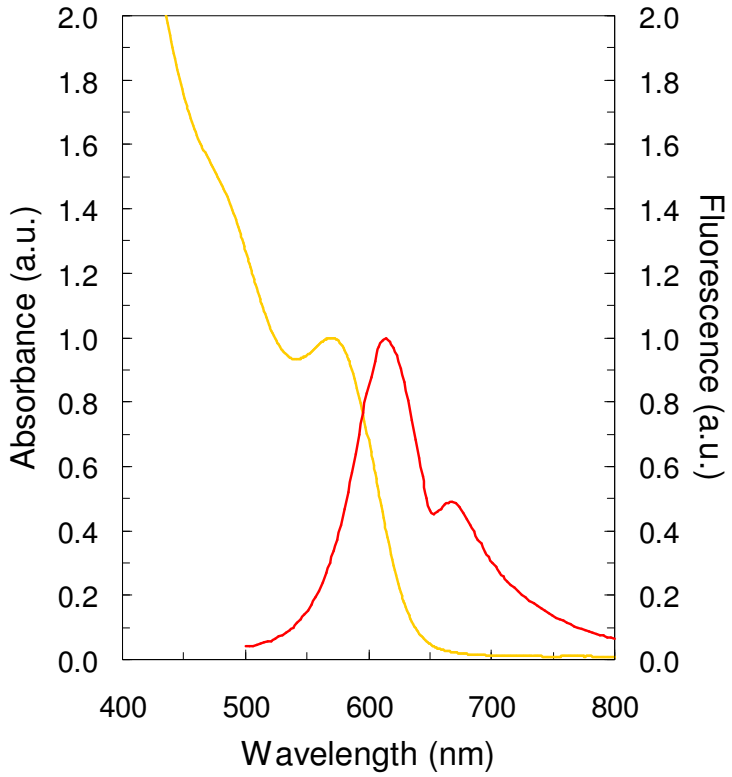

Figure 5.14. Overlay of optical absorption and fluorescence spectra for the InP-myristic acid sample in hexanes. Reproduced with permission of Annick Anctil [98].

Doping of the InP QDs with Eu^{3+}, Er^{3+}, and Tb^{3+} were performed by incorporating a stoichiometric amount of the rare-earth-nitrate in the cation precursor solution. A representative fluorescence contour map of a 5% Tb^{3+} doped InP sample is provided in Figure 5.15. The y-axis is the excitation wavelength, the x-axis is the emission wavelength, and the color indicates the intensity of emission (in a.u.) at each point. In the figure, the InP emissions occur at ~619 nm and ~674 nm. This is consistent with Figure 5.14 wherein the maximum absorption (1st excitonic absorption) occurs at ~619 nm. The 5% Tb^{3+} (molar) included in the precursor does not appear to be participating optically, but its introduction into the solution did not affect the growth process. The Tb^{3+} ions may not be situated in lattice sites which allow for optical emission, or were unsuccessfully incorporated into the QDs. Similar results were observed for InP samples doped with Eu^{3+} and Er^{3+}. The use of rare-earth ions coordinated with ligands (instead of nitrate) when incorporated into the precursor solution may be more effective at introducing them into the InP crystal. No measurable RL was observed from either the doped or un-doped samples. The lack of RL signature is attributed to a coating of the QDs with ODE and myristic acid which absorbs the alpha-particle energy. When these capping ligands were removed the exposure to the oxygen environment resulted in a visible color change (this time from red to brown) and a complete quenching of the visible luminescence (under UV excitation).

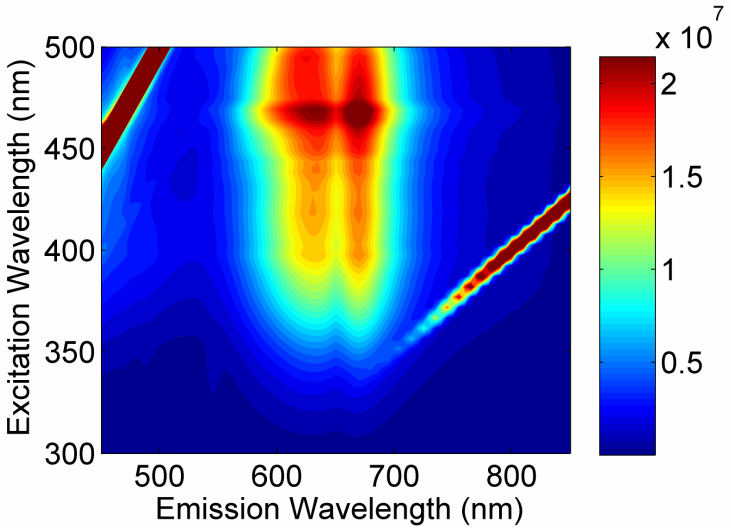

Figure 5.15. Fluorescence contour map (excitation vs. emission) of a 5% Tb^{3+} doped InP (Myristic Acid-capped) QD sample synthesized at 270° C. The maroon lines are the result of the first order (slope = 1) and second order (slope = 2) reflections of the excitation source from the quartz cuvette.

5.3.4 Y_2O_3 nanophosphors

Strong radioluminescence was observed in Y_2O_3 samples comprised of various dopants (and co-dopants), dopant concentrations, and particle sizes. Much of the development of the Y_2O_3:Eu^{3+} and Y_2O_3:Tb^{3+} nanophosphor material systems can be found in ref. [99]. The remainder of this section consists of an overview of the development of co-dopant Y_2O_3 nanophosphor material. Additionally, the results pertaining to the optimization of Y_2O_3:RE^{3+}thin-films for maximum radioluminescence emission are discussed. The radiation tolerance of many materials are also discussed and compared to commercially available materials.

One of the most promising co-dopant systems for increased radioluminescence efficiency is Y_2O_3:Eu^{3+},Ce^{3+}. Figure 5.16 contains photoluminescence (PL) spectra of the pre- and post-anneal 8% Eu^{3+}, 2% Ce^{3+} co-doped Y_2O_3 nanophosphor under 488 nm laser excitation. No PL or RL emission lines are observed from the Ce^{3+} ion in either spectrum; however enhanced PL and RL is observed which is indicative of an energy

transfer mechanism from the cerium ion to the europium ion. Clearly the annealing stage enhances the PL which is indicative of more crystalline material. To analyze the PL and RL of the nanophosphor, thin-films (1 cm^2) were spray deposited onto a microscope slide (following the optimized procedure / film thickness discussed below). Digital images of a representative film under ambient lighting (a), and under 254 nm optical excitation (b), are provided in Figure 5.17. The red emission color is consistent with the PL spectrum shown in Figure 5.16. Additionally, even though the excitation power under the ^{210}Po source is <2 $\mu W\ cm^{-2}$ the RL emission is clearly visible with the naked eye.

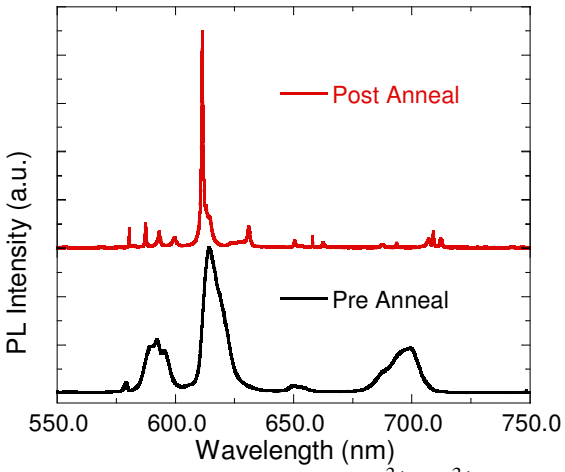

Figure 5.16. Photoluminescence spectra for $Y_2O_3:Eu^{3+},Ce^{3+}$ nanophosphor pre- and post-anneal. The excitation wavelength was 488 nm.

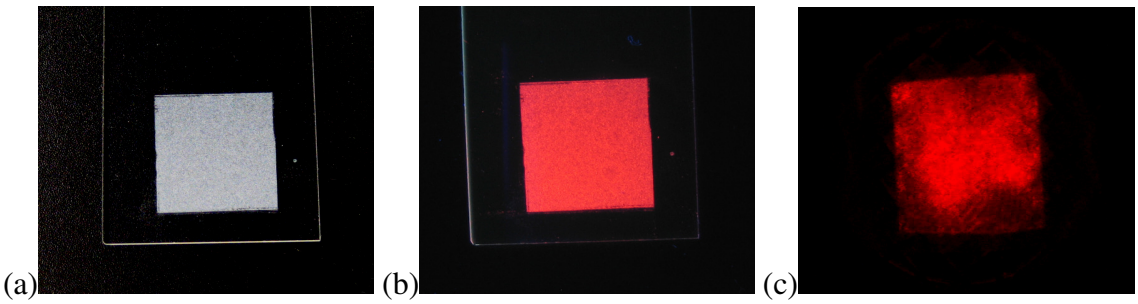

Figure 5.17. Digital images of Y2O3:Eu3+, Ce3+ under (a) room light, (b) 254 nm excitation, and (c) irradiation by a ^{210}Po α-particle source.

The RL spectrum of the $Y_2O_3:Eu^{3+},Ce^{3+}$ nanophosphor was compared to the spectral responsivity of an $InGaP_2$ photodiode and is provided in Figure 5.18. The RL

spectrum was measured as detailed above. The emission from the nanophosphor is well tuned to the spectral responsivity of the photodiode. Additionally, the narrow emission spectrum of the nanophosphor will enable the use of distributed Bragg reflectors (DBR) below the base of the photodiode to reflect light, which was transmitted through the photovoltaic device, towards the junction region. Devices with a DBR can be grown with a thinner base layer to enhance their low-light photoconversion efficiency by reducing the base layer dark current.

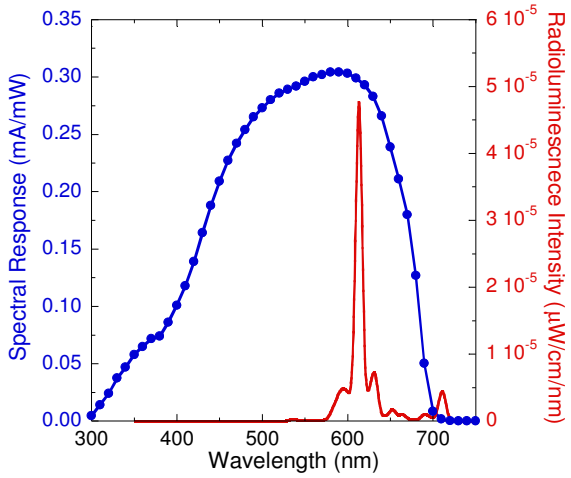

Figure 5.18. Overlay depicting the spectral responsivity of an $InGaP_2$ PV device and the radioluminescence spectrum of a Y_2O_3:Eu^{3+}, Ce^{3+} nanophosphor thin-film irradiated by a 1 mCi ^{210}Po alpha-particle source.

To illustrate the vast improvement obtained by using a co-dopant material system, the RL spectrum of a thin-film comprised of 8% Eu^{3+} doped Y_2O_3 is overlaid with the RL spectrum of the 2% Ce^{3+} / 8% Eu^{3+} co-doped Y_2O_3 thin-film shown above (see Figure 5.19). The co-doped material shows an order of magnitude increase in power output (integrated over 500 nm – 700 nm range), and is approaching the photon output of a commercial ZnS:Ag^{2+} thin-film which is optimized for alpha-particle detection.

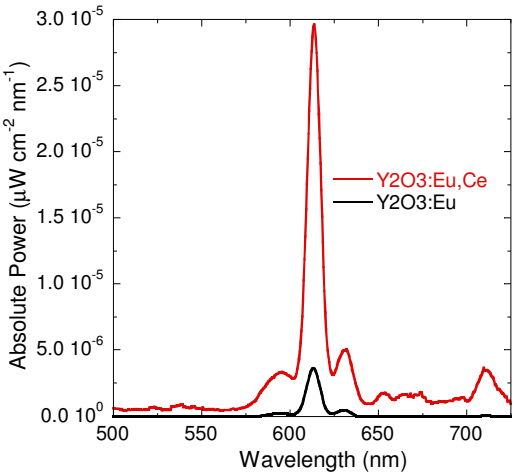

Figure 5.19. Y_2O_3:Eu^{3+} and Y_2O_3:Eu^{3+},Ce^{3+} radioluminescence emission spectra under excitation by a 1 mCi ^{210}Po alpha-particle source.

Y_2O_3:Eu^{3+} co-doped with Er^{3+} was also investigated in this research. In particular, the RL spectrum of a Y_2O_3 nanophosphor doped with 2.5% Er^{3+} and 2.5% Eu^{3+} in Y_2O_3 is provided in Figure 5.20. In the Y_2O_3: Eu^{3+},Er^{3+} spectrum, both the Eu^{3+} (611 nm) and Er^{3+} (550-575 nm and 650-670 nm) emission lines are present, yet the total intensity of the emission is much lower than its singly doped 8% Eu^{3+} counterpart. The Er^{3+} emission is much stronger than previously observed for singly doped Y_2O_3:Er^{3+}, which suggests an energy transfer from the Eu^{3+} ion to the Er^{3+} ion, resulting in a diminished Eu^{+3} emission at 611 nm.

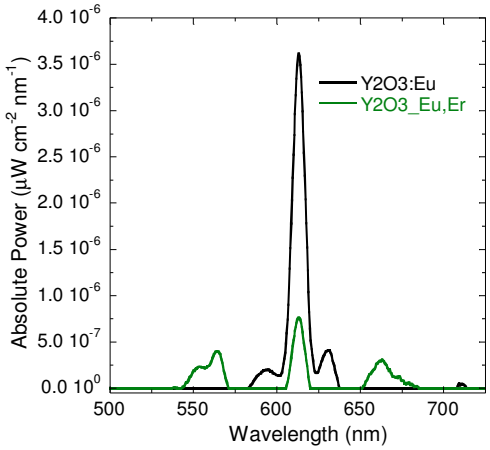

Figure 5.20. Y_2O_3:Eu^{3+} and Y_2O_3:Eu^{3+},Er^{3+} RL emission spectra under excitation by a 1 mCi ^{210}Po alpha-particle source.

The thickness and uniformity of the nanophosphor film largely affects the radioluminescence efficiency measured from a given sample under excitation by alpha-particles. The short range of the alpha-particles (<20 μm), along with the isotropic emission of the source both contribute to this issue. Consequently, the properties of the thin-film deposition technique play a key role in the overall efficiency of the device. To achieve a thin, uniform nanophosphor film, a spay deposition of the $Y_2O_3:RE^{3+}$ material was used. Figure 5.21a contains a digital image of the spray coating apparatus used to deposit the thin-films. Spray deposition was accomplished by suspending the nanophosphors in acetone with a 1-5% PMMA binder to assist in suspending the materials and to promote adhesion to the substrate. The nanophosphors used in the thickness optimization were $Y_2O_3:Eu^{3+}$ and $Y_2O_3:Tb^{3+}$. The normalized radioluminescence of the two materials has been overlaid with the spectral responsivity of an $InGaP_2$ PV device in Figure 5.21b. This overlay demonstrates the monochromacity and matching of the emissions to that of the $InGaP_2$ PV spectral responsivity.

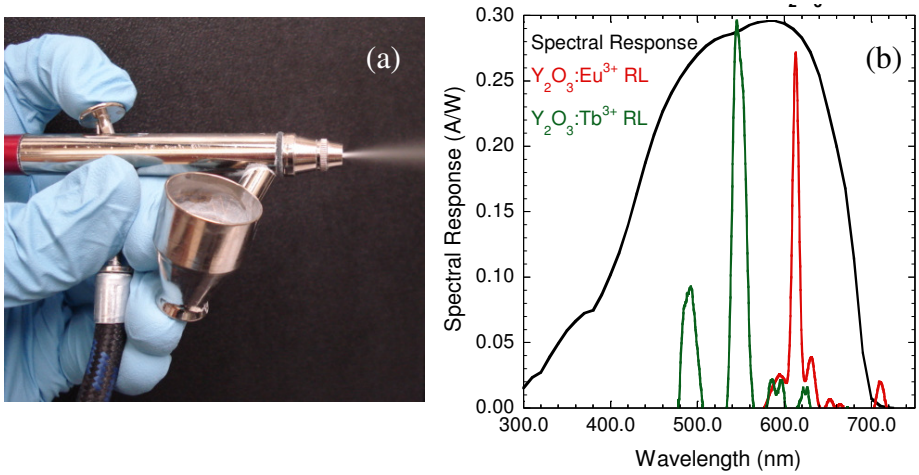

Figure 5.21. (a) Digital image of spray deposition apparatus, and (b) $InGaP_2$ PV spectral responsivity with respect to wavelength overlaid with the normalized radioluminescence of $Y_2O_3:Eu^{3+}$ (red curve) and $Y_2O_3:Tb^{3+}$ (green curve) QD phosphors.

To optimize the radioluminesce emission from a QD phosphor thin-film, seven Y_2O_3:Tb^{3+} (1% Tb^{3+}) films were spray deposited with increasing thickness. The thicknesses of the films were measured the using profilometry and transmission spectroscopy. A representative profile of a QD thin-film, measured with a Tencor contact profilometer is provided in Figure 5.22. This measurement technique provides a method for determining the thickness of the deposited QD thin-film. Additionally, the uniformity of the profile over a linear cross section of the material can be obtained.

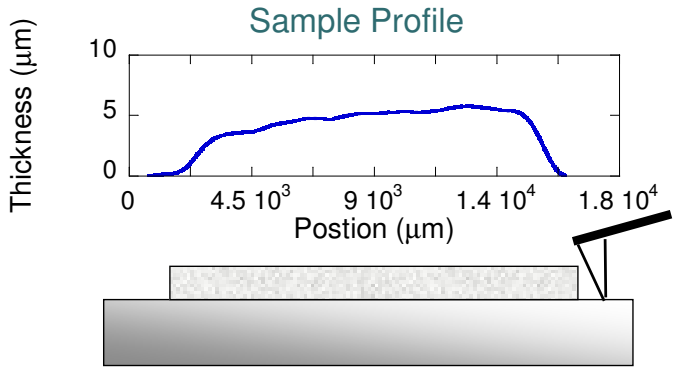

Figure 5.22. Representative thin-film QD phosphor profile measured using a Tencor Profilometer.

The average film thickness of the phosphors was evaluated using transmission spectroscopy. The transmittance verses wavelength for the series of samples was measured and plotted in Figure 5.23a. In Figure 5.23b the transmittance at 700 nm (chosen since there are no distinctive emissions at this wavelength) is plotted with respect to film transmittance. Based on this plot an exponential relationship between the transmittance and thin-film thickness can be observed. The equation for the exponential trend line is provided in the figure.

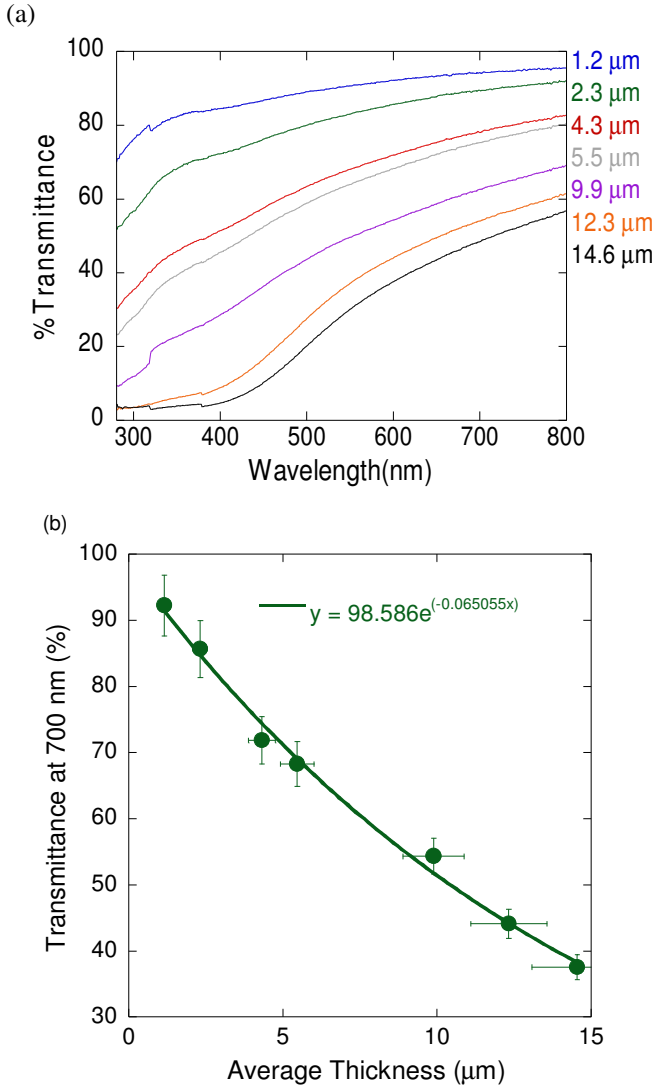

Figure 5.23. (a) Transmittance verses wavelength, and (b) transmittance at 700 nm verses average thickness, for the series of Y_2O_3:Tb^{3+} (1% Tb^{3+}) thin-films of varying thickness.

The radioluminescence of the thin-films under alpha-particle irradiation were measured to determine the optimal film-thickness. The peak (550 nm) radioluminescence intensity of the seven films was plotted with respect to film thickness and displayed in the figure below. As expected, a unimodal distribution is obtained. The RL intensity initially increases with increased film thickness because a greater amount of the alpha-particle energy is absorbed. Once the film thickness exceeds ~11 µm, the intensity drops

because the additional alpha-particle energy that is absorbed does not exceed the additional reflection, scattering, and self absorption of the emitted light due to the increased Y_2O_3 film thickness. Peak RL intensity can be obtained for a film with a thickness ranging between 7 μm and 12 μm. This experiment was also performed for the Y_2O_3:Eu^{3+} (5%) films and the range of optimal film thickness agreed with the results presented here.

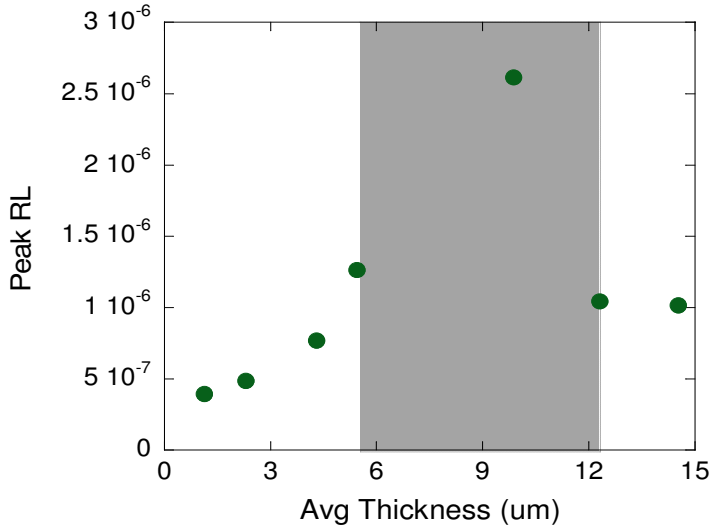

Figure 5.24. Peak radioluminescence emission from Y_2O_3:Tb^{3+} QD thin-films (550 nm) plotted with respect to the film thickness.

The main thrust of this research is to investigate the effect of particle size on the radioluminescence efficiency and radiation tolerance of the radioluminescent thin-film. To that end, four Y_2O_3:Eu^{3+} (5%) samples with particles sizes in the ranges of: 20-50 nm, 50-150 nm, 250-400 nm, and 500-1000 nm were synthesized. For each particle size range, 3-4 thin-films of increasing thickness were prepared to determine whether the same relationship for thickness verses transmission at 750 nm was observed. For the samples prepared in the 50-150 nm range, the slope and intercept were the same as in Figure 5.23b, within measurement error, which was expected because the material used

to generate that figure had a similar distribution. For the samples with a smaller size distribution, the x-intercept was approximately the same (i.e., the transmission of the quartz slide ~96%), yet the magnitude of the slope was much greater (more negative) indicating an increased scattering rate. The converse was true for the samples with particle distributions larger than 50-150 nm. Intuitively, a greater packing density is expected for smaller particles resulting in more particles (and therefore, more scattering planes) for a given thickness. This variability in scattering rate with respect to particle size makes it difficult to accurately compare the impact particle size has on RL intensity since the measured differences were very low. Consequently, the difference in RL intensity for the samples measured is below the detectable limit.

The radiation tolerance of the materials should be independent of film thickness, provided the film thickness is close to the optimal. A "close to optimal" nanophosphor film was obtained for each of the particle sizes by taking the film thickness which had the greatest RL for each particle size. Each sample was affixed to a ^{210}Po alpha-particle source and the RL intensity was measured at periodic intervals throughout the course of three weeks. The RL intensity with respect to alpha-particle fluence for the four samples is provided in Figure 5.25 along with linear curve-fits. This data has not been corrected for the reduction in the ^{210}Po activity which, at the time of the last measurement, had reduced to ~65% of its initial activity. Therefore, less than 20% reduction in RL intensity after a fluence of 2.6×10^{13} α/cm^2, was observed. In a previous report [13], a degradation of 50% for a $Y_2O_3:Eu^{3+}$ sample was observed after a dose of 1.4×10^6 Gy under (^{238}Pu alpha-particles). In the present study, the dose was approximately 2.4×10^6 Gy. The radiation tolerance appears to be similar for the three largest particle sizes

measured, while the smallest material system has an additional ~25% greater tolerant (based on the linear curve fit slope).

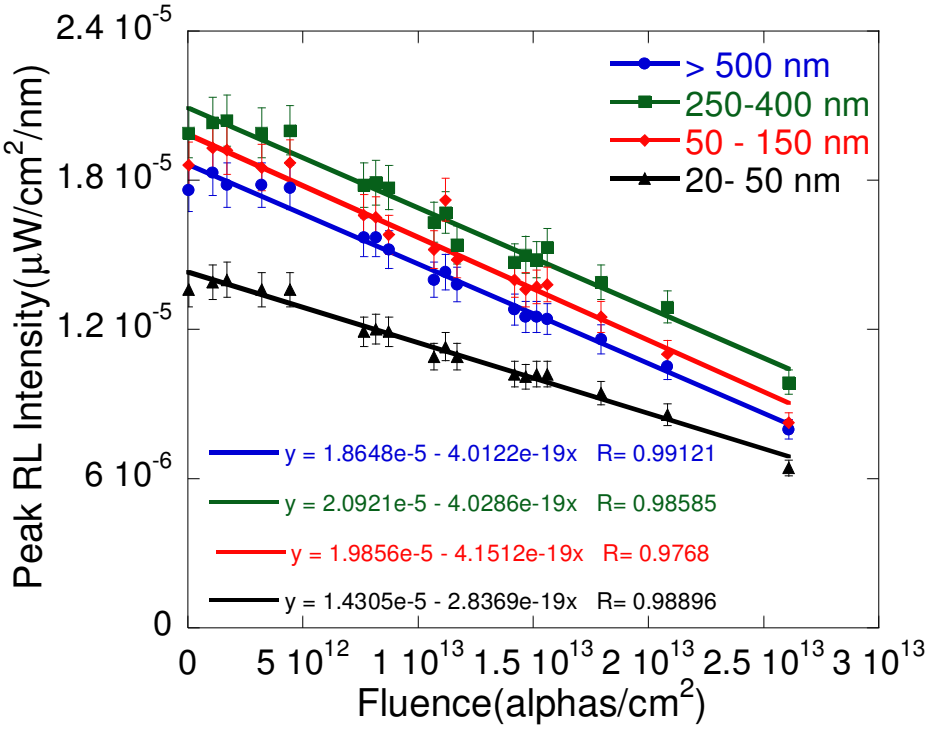

Figure 5.25. Normalized peak radioluminescence with respect to 4.2 MeV alpha-particle fluence for $Y_2O_3:Eu^{3+}$ (5%) with various particle sizes: 20-50 nm, 50-150 nm, 250-400 nm, and >500 nm. Solid lines represent linear curve fits and their corresponding equations (correspond by color) are below the curves.

Characterization of the radiation tolerance was also performed by comparing the normalized RL as a function of alpha particle fluence for a 5% $Y_2O_3:Eu^{3+}$ film to that of a $ZnS:Ag^{2+}$ commercial phosphor thin-film. This comparison is shown in Figure 5.26 and illustrates that the $Y_2O_3:Eu^{3+}$ nanophosphor material withstands a fluence of over 10^{13} alpha-particles/cm^2 before degrading by 20%. This represents an improvement by over an order of magnitude over that of the $ZnS:Ag^{2+}$ material. Additionally, the $ZnS:Ag^{2+}$ material is well known to have one of the highest radioluminescence efficiencies, however, after ~8×10^{12} alpha particles/cm^2 the absolute power emitted by the $Y_2O_3:Eu^{3+}$ exceeded that of the $ZnS:Ag^{2+}$ material.

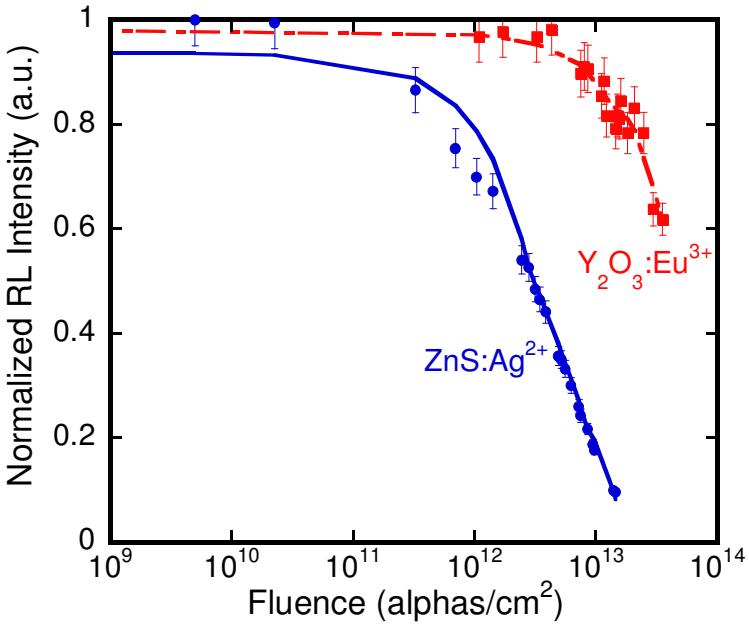

Figure 5.26. Normalized radioluminescence intensity as a function of alpha-particle fluence for ZnS:Ag^{2+} and Y_2O_3:Eu^{3+}.

5.3.5 Additional nanophosphors

The radioluminescence of rare-earth doped YAG and silver doped ZnS nanophosphors were also investigated in this research. The use of thermal processing to synthesize the YAG:RE^{3+} phosphors made size control difficult since the size of the particles increased with successive thermal anneals (in air). To further reduce the size of the YAG:RE particle size and to synthesize nanocrystalline ZnS:Ag^{2+}, targets of the as produced YAG:RE nanophosphors and bulk ZnS:Ag^{2+} phosphors were pressed and ablated using the laser vaporization reactor. Thin-films of these materials were deposed onto quartz slides, which were subsequently placed under ^{210}Po alpha-particle sources and the RL was measured. The RL efficiency of the resultant material was lower than that of the Y_2O_3:RE^{3+} materials. Figure 5.27 contains the RL spectra of YAG:Eu^{3+} and YAG:Tb^{3+} nanophosphors. The RL spectrum obtained for the Tb^{3+} doped YAG is nearly identical to the Y_2O_3:Tb^{3+} spectrum which results from the Tb^{3+} ion having identical site

point group symmetry in both materials. The emission spectrum is slightly different for the Eu^{3+} ion in YAG (as compared to Y_2O_3) which indicates the emission is from an ion situated in a crystal site with differing group symmetry, or perhaps a different oxidation state of the europium ion (e.g., Eu^{2+}).

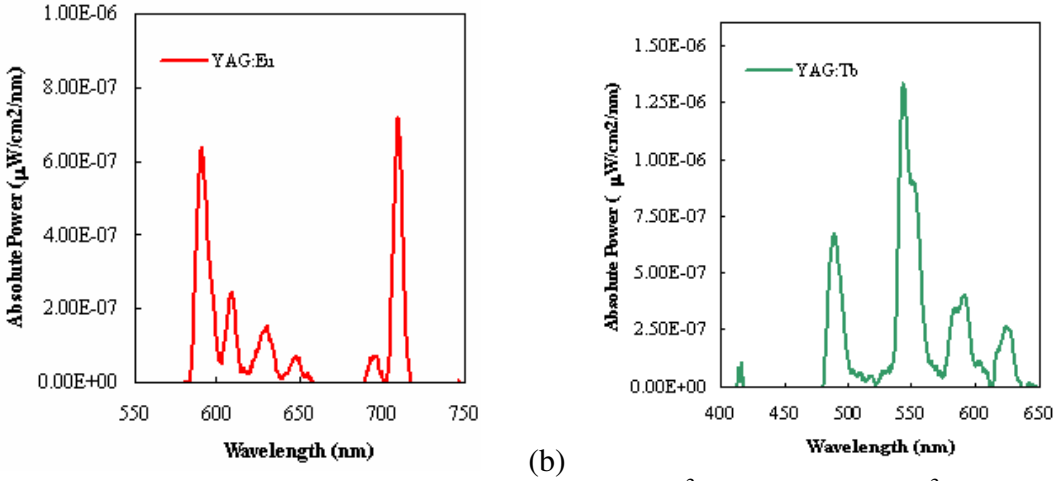

(a) (b)

Figure 5.27. Radioluminescence spectra of (a) YAG:Eu^{3+} and (b) YAG:Tb^{3+} under excitation by a ~1 mCi ^{210}Po alpha-particle source.

5.4 *ADEP* MODELING OF THE PHOSPHOR FILMS

The alpha-particle energy deposition profiling procedure can be applied to phosphors just as it was used to investigate the energy deposition within III-V semiconductor devices. However, to use this model to simulate the *ADEP* in a porous thin-film with a density much less than the material density of 5.5 g/cm^3 (*i.e.,* the density of Y_2O_3), the effective density must be used (3 g/cm^3 was calculated based on material deposited, area, and mass increase). Such an assumption is valid because of the simulation technique employed by the SRIM-2003 software. It does not treat the energy loss of each particle continuously through the film. It uses random number generators to determine a "hop" distance traveled as well as the energy lost during that "hop" distance, then it simply spreads the energy loss equivalently over the material traveled [11].

The resultant alpha-particle energy deposition profile (*ADEP*) for a Y_2O_3 thin-film phosphor with a density of 3 g/cm^3 is provided in Figure 5.28. For the simulation, the source device distance was assumed to be 4 mm like that employed during testing. This figure contains a contour plot of the cross section of the thin-film with the y-axis depicting the depth of alpha-particle penetration and the x-axis corresponds to the horizontal displacement from the center of the film. The contours represent the percent of the total alpha-particle energy, normalized to the peak deposition rate within the film, which is deposited throughout the film. The energy deposition for this source-sample configuration is shown to peak at approximately 4.5 μm into the film, and dropping to ~10% at the base of the film. Additionally, the normalized ionization rate remains greater than 50% from the film surface to a depth of ~11 μm, at which point a steep gradient in normalized intensity is observed. This result may be somewhat counterintuitive since the range of 4.2 MeV alpha particles in Y_2O_3 with a density of 3 g/cm^3 is over 20 μm. However, the result of the model is consistent with the experimental data comparing the peak RL of Y_2O_3:Tb^{3+} (1%) with respect to film thickness (see Figure 5.24); this data indicated the optimal film thickness to fall within the 7-12 μm range. The peak in ionization energy is a result of the isotropic emission of the source, and the non-linear energy deposition rate of each alpha particle (*i.e.*, more energy is lost towards the end of the range).

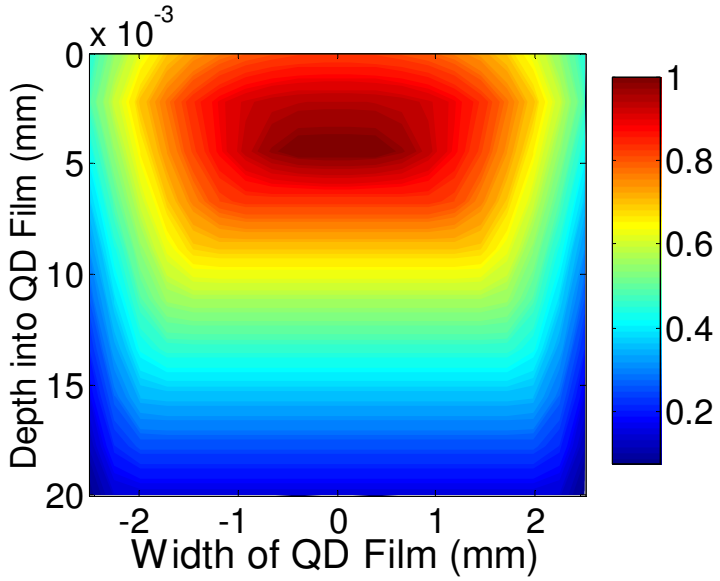

Figure 5.28. Normalized contour plot for a cross sectional *ADEP* within a QD film comprised of nanocrystalline Y_2O_3 with a density of 3 g/cm^3.

5.5 PHOTOVOLTAIC CONVERTER CHARACTERIZATION

The use of well established OMVPE growth techniques enabled the successful growth of high quality $InGaP_2$ photovoltaic cells. In particular, a thin, heavily doped n-type emitter on a p-type base was the structure used (see Table 5.1). The heavily doped emitter causes the depletion region to primarily extend into the base. This approach was used because it reduces the length holes in the emitter have to travel before reaching the junction, making the device dependent on the much longer diffusing length of electrons within the base. The top and back windows, comprised of AlInP (E_g >1.95 eV), create potential barriers at the interface which are effective at reducing the surface recombination velocity. Figure 5.29 contains a digital image of two $InGaP_2$ photovoltaic devices.

Table 5.1. $InGaP_2$ photovoltaic cell structure and chemical composition.

Layer	Material	Thickness
Electrode	Au/Ge	**2 Microns**
Contact	n GaAs	**500 Angstroms**
Top Window	n AlInP	**500 Angstroms**
Emitter	n $InGaP_2$	**500 Angstroms**
Base	p $InGaP_2$	**3000 Angstroms**
Back Window	p AlInP	**500 Angstroms**
Substrate	p GaAs	**350 Microns**
Cathode	**Au/Zn**	**2 Microns**

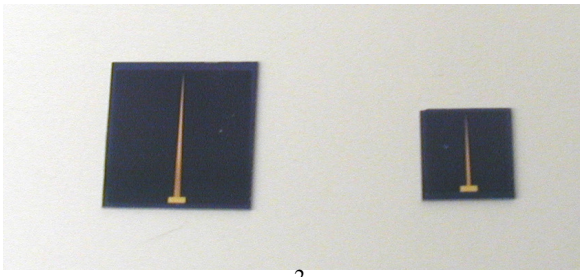

Figure 5.29. Digital photographs of a 1.0 cm^2 $InGaP_2$ PV cell (left), and a 0.25 cm^2 $InGaP_2$ PV cell (right) both have grid contacts with a center spike providing a 4% light shadowing.

Representative AM0 I-V characteristics and spectral responsivity of the OMVPE grown $InGaP_2$ photovoltaic cells is provided in Figure 5.30. The open circuit voltage and short circuit current of the photodiode were 1.19 V and 10.9 mA/cm^2, respectively, corresponding to an AM0 efficiency of ~ 7%. This efficiency is relative to the AM0 spectrum, which the band gap of an $InGaP_2$ photovoltaic cell is not well tuned to. In comparison, the quantum efficiency of the cell reached 63% ($QE = SR \times hc/\lambda$) for 611 nm light (see Figure 5.30b).

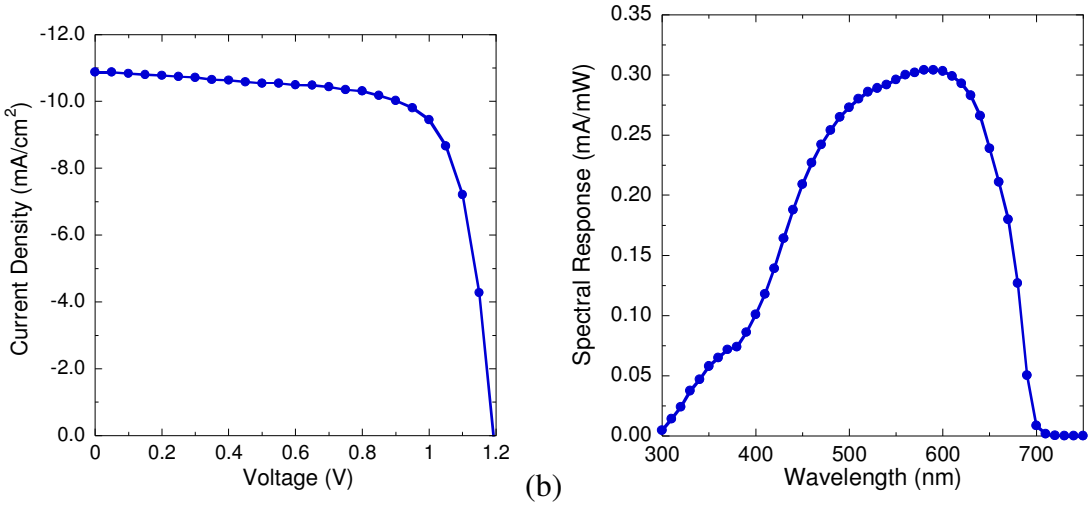

(a) (b)

Figure 5.30. (a) I-V response under simulated AM0 illumination and (b) spectral responsivity for a representative $InGaP_2$ photovoltaic cell.

5.6 RADIOISOTOPE BATTERY PROTOTYPE

Prototype QD radioisotope batteries were fabricated by spray depositing the nanophosphor over the surface of the $InGaP_2$ PV cell. The favorable spectral matching between the $Y_2O_3:Eu^{3+},Ce^{+3}$ nanophosphors and the spectral responsivity of the $InGaP_2$ PV cell is illustrated in Figure 5.18 above. Additionally, the I-V characteristics of a radioisotope battery comprised of a thin-film of $Y_2O_2:Eu^{3+}$ (5% Eu^{3+}) nanophosphor and an $InGaP_2$ photovoltaic cell similar to that shown in Figure 5.18 is provided in Figure 5.31. The short circuit obtained was 0.064 mA/cm^2 and the open circuit voltage obtained was 0.48 V. The maximum power achieved was 18.7 nW/cm^2. However, from calculations based on Equation (3.3), the total alpha-particle power incident with the phosphor layer is 795.0 nW/cm^2 which leads to a conversion efficiency η_{semi} = 2.4% in this prototype stack configuration. A voltage of only 0.48 V was achieved since the intensity of the ^{210}Po source was quite low (~0.5 mCi). Assuming a photovoltaic conversion efficiency of 16% (*i.e.*, 31 mA/mW @ 0.5 V), the nuclear-to-light efficiency of the $Y_2O_3:Eu^{3+}$ reached approximately 15%. However, by using a film with a thickness

in the optimal range, 7-12 μm, it is possible that a small percentage of alpha particles penetrated through the phosphor into the diode and contributed to the power generation.

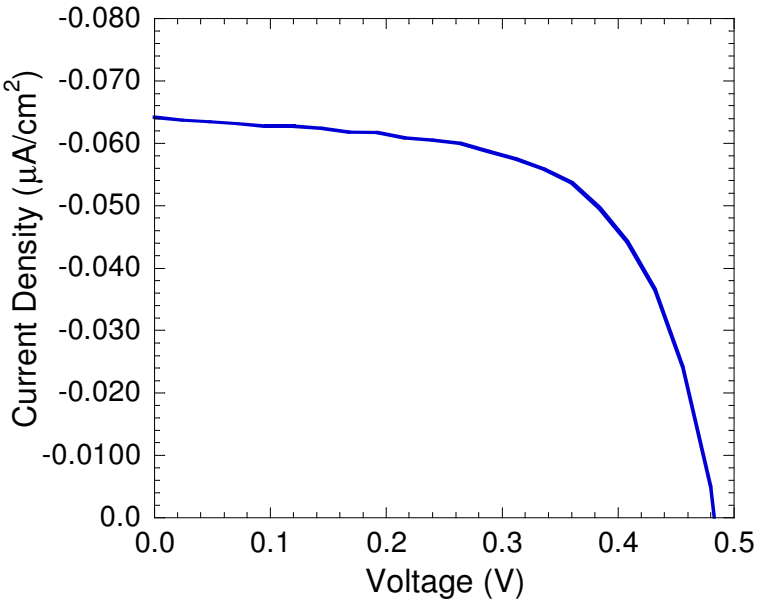

Figure 5.31. Current density vs voltage plot for a prototype QD radioisotope battery comprised of Y_2O_3:Eu^{3+} and an $InGaP_2$ PV cell.

The device performance shown above represents only a single QD radioisotope stack corresponding to ~0.06 cm^3 (assuming a source thickness of 100 μm). Consequently, 15 additional stacks can be assembled together to increase the power output 15 fold. Additionally, by increasing the activity by a factor of 10, a 20 fold increase in power output can be achieved provided the V_{oc} of the diode increases to 1.0 V. The power output of such a device would reach 5.61 μW/cm^3 with a nuclear-to-electrical conversion efficiency of ~5%. Although 0.5 mCi was required to achieve the performance shown above, the effective activity required to achieve the same performance if the source is in direct contact with the QD layer is 0.05 mCi. Consequently, a 5.61 μW/cm^3 power output would require only 7.5 mCi. This activity is

consistent with the activity used to monitor the radiation tolerance of the $Y_2O_3:Eu^{3+}$ phosphor which ~5% degradation after a dose of 1.1×10^6 Gy.

CHAPTER 6. RADIATION AND THERMAL EFFECTS IN NANOSTRUCTURED III-V SOLAR CELLS

6.1 QUANTUM DOT SOLAR CELLS (QDSC)

The state-of-the-art (SOA) in space solar cells utilizes epitaxially grown III-V materials to form series-connected multijunction devices. SOA latticed matched triple-junction space solar cells now exceed the 30% efficiency barrier under 1 sun AM0 illumination [100]. The maximum efficiency of such devices is limited by the bandgap of the available III-V materials as a result of the lattice-matching constraint. Theoretical calculations have shown that efficiency improvements are possible if the spectral bandwidth of the GaAs (or middle junction cell) of a conventional triple junction cell (grown on Ge) could be extended to longer wavelengths [48]. Many recent investigations have considered the use of self-organized InAs quantum dots (QD) to provide such additional sub-GaAs energy bandgap ("subgap") photocurrent generation in an attempt to increase the total current output of the device [48-50, 101-103]. QDs may be incorporated within the intrinsic region of a p-type / intrinsic / n-type (*pin*) GaAs cell structure using a Stranski-Krastanov organometallic vapor phase epitaxy (OMVPE) growth mode forming a sequentially stacked structure comprised of alternating layers of InAs QDs, and intrinsic GaAs barriers. Evidence of subgap photovoltaic conversion has been demonstrated in such a structure wherein InAs QDs [49, 50, 103] or GaSb QDs [102] were introduced.

The thermal behavior and radiation tolerance of QD solar cells (QDSC) are important characteristics that must be evaluated to determine the suitability of these devices for space applications. Furthermore, investigations of these characteristics may

reveal information that assists in understanding the behavior of the QDs within the structure. Individually, OMVPE grown InAs quantum dots are known to demonstrate size dependent electronic properties consisting of discrete-like electronic states [104]. When incorporated into an array, overlapping of the individual QD electronic wavefunctions causes delocalization of the electrons which may lead to the formation of isolated mini-bands [104]. Temperature dependent optoelectronic and photovoltaic measurements are favorable techniques for investigating the role of QDs in QDSC since the electronic delocalization is strongly dependent on temperature. There have been many demonstrations of enhanced radiation tolerance of QD arrays and QD lasers in comparison to their multiple quantum well and bulk counterparts [51-55]. Alpha-particle irradiation of QDSC will determine if such trends continue when the QDs are located within the intrinsic region of a *pin* device.

6.1.1 Experimental

GaAs *pin* devices (1×1 cm^2) containing 1- and 5-layers of InAs QDs and a reference *pin* device were grown using OMVPE which has been reported elsewhere [50]. The temperature dependent dark and illuminated current density vs. voltage (*J-V*) characteristics and spectral responsivity (SR) were measured using an Oxford Instruments cryostage affixed with a quartz window. The temperature was varied in 20°C increments over the temperature range of 80 K – 420 K. Full illumination of the devices was used in the measurements and the band pass of the quartz window was ~90% over the wavelength range of 350-2200 nm.

Irradiation of the devices was accomplished by placing them ~2 mm from a ^{210}Po alpha-particle source with an activity of ~ 1 mCi and a circular area of ~2.5 cm^2. Upon

reaching the device the alpha-particles have an average energy of ~4.2 MeV which results in a range ~12 μm [11]. The irradiation took place in air under ambient conditions. The *J-V* characteristics and the *SR* of the devices were measured after incremental dose of alpha-particles up to a total fluence of ~6×10^{12} alpha-particles / cm^2.

6.1.2 Results and Discussion

6.1.2.1 THERMAL DEPENDENT DEVICE OPERATION

The dark diode response of the QDSC containing 1-layer of InAs QDs (1QD) and the QDSC containing 5-layers of InAs QDs (5QD) over the temperature range of 100 K – 400 K are depicted in Figure 6.1a and b, respectively. The strong temperature dependence observed in the 1QD device is characteristic of an injection or space charge region recombination dominated forward bias current. Both mechanisms have a Boltzmann-type thermal dependence wherein the injection current and space charge region recombination current vary in relation to the intrinsic carrier concentration n_i as $n_i^2 \propto \exp(-qE_g/kT)$ and $n_i \propto \exp(-qE_g/2kT)$, respectively [105]. The 5QD device appears to be is dominated by a temperature independent tunneling current mechanism at low temperatures which transitions to temperature dependent injection or space charge region recombination current once the temperature exceeds ~260 K. At low temperatures, it has been shown that the electrons in the InAs QD become confined to their ground state [104]. Consequently, the temperature independence observed in the 5QD device at low temperatures may result from a hopping like conduction mechanism through the QD array located in the center of the intrinsic region.

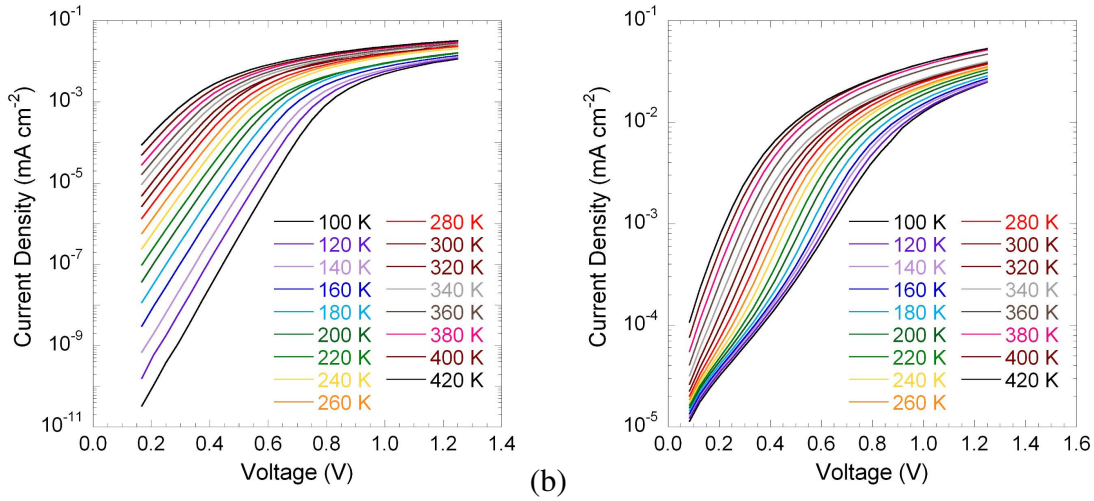

Figure 6.1. Dark diode current density vs. voltage for (a) 1QD and (b) 5QD, measured over the temperature range of 100 – 400 K.

Figure 6.2a,b contain the spectral responsivity of the two QD devices measured at incremental temperatures. The spectral responsivity of the devices is characteristic of GaAs-based solar cells with the 1QD device having a slightly greater responsivity than that of the 5QD device. The reduced responsivity may be related to defects in the emitter or intrinsic region causing the minority carrier diffusion length to be reduced. Defects may result from the strain caused by introducing 5 layers of InAs QDs within the intrinsic region of the device [106]. The use of strain compensation layers, grown between each InAs QD layer, to eliminate this effect will be the topic of the following section [50]. In these devices, the spectral bandwidth widening afforded by incorporating the InAs QDs is observed in the subgap responsivity of the 1QD device and more pronounced in the 5QD device (*i.e.,* in the 880-940 nm range).

The thermal dependence of the SR in the two devices is characterized by a shifting of the band-edge absorption to lower energy. This shift results from bandgap narrowing due to thermal expansion and is well documented in the literature [107]. In

addition, increases in the SR beginning at ~660 nm are observed with increasing temperature. Such an increase may be related to an improved minority carrier diffusion length. The thermal dependence of the minority carrier diffusion varies with the diffusion coefficient as $\sim T^{1}$, the minority carrier lifetime as $\sim T^{1/2}$, and the minority carrier mobility as $\sim T^{-3/2}$ for mobility dominated by acoustic phonon scattering or as $\sim T^{3/2}/N$ (where N-doping concentration) for mobility dominated by ionized impurity scattering [105].

In Figure 6.2(c) the thermal dependent spectral responsivity of the 5QD device is plotted over the wavelength range of 800 – 1100 nm to better illustrate the InAs QD photoresponse. The shoulder observed at ~ 850 nm in the 100 K SR curve and shifting towards longer wavelengths with increasing temperature may be attributed to an excited state transition within the InAs QD array. A second shoulder observed at ~ 960 nm in the 100 K curve follows a similar trend. Both transitions display a strong thermal dependence which is suggestive of electrons in the excited states of the InAs QDs being thermalized into the GaAs barrier. Two additional peaks are observed in the SR at ~1040 nm and ~1080 nm, which are nearly temperature independent. This temperature independent behavior suggests a photon extraction mechanism from the InAs QD to the GaAs barrier. Such a process requires a two-photon absorption mechanism [103], one to excite a carrier in the QD, the second exciting the carrier to the energy of GaAs conduction band edge. A measurement of the dependence on excitation power of the SR at these wavelengths could be used to verify this mechanism since the responsivity should increase with excitation power if it has a multi-photon dependence.

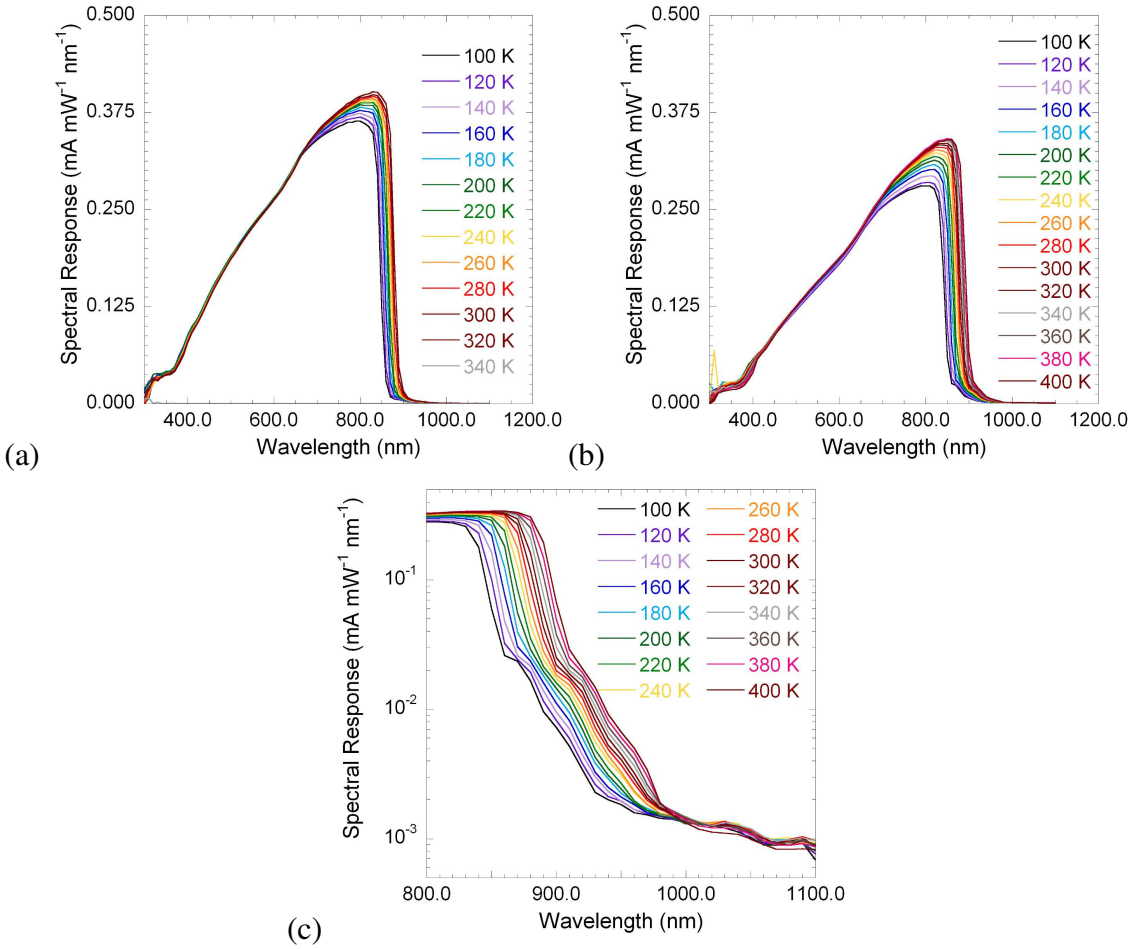

Figure 6.2. Spectral responsivity verses wavelength of over the temperature range of (a) 100 – 340 K for the 1QD device, and (b) 100 – 400 K for the 5QD device. In (c), the spectral responsivity of the 5QD device is plotted on a log-scale over the wavelength range of 800-1100 nm to better illustrate the InAs QD photogenerated current.

The open circuit voltage, short circuit density (J_{sc}), fill factor, and efficiency of the 1QD and the 5QD devices under AM0 illumination are plotted with respect to temperature in Figure 6.3. Also included in the plots are linear trendlines, the slopes of which indicate the temperature coefficients of the various parameters. The V_{oc} dependence on temperature (Figure 6.3(a)) is 1.17 mV/°C and 1.32 mV/°C, for the 1QD and 5QD devices, respectively. The V_{oc} temperature dependence of GaAs-based devices typically decreases linearly with temperature and is primarily due to dark current increases [105]. The dark current temperature dependence is derived from the injection

current and depletion region recombination current components. Tunneling is also a dark current component but is largely temperature independent. Typical values of GaAs-based solar cell V_{oc} temperature dependences range from 1.9-2.2 mV/°C, which is consistent with the two QD devices [105].

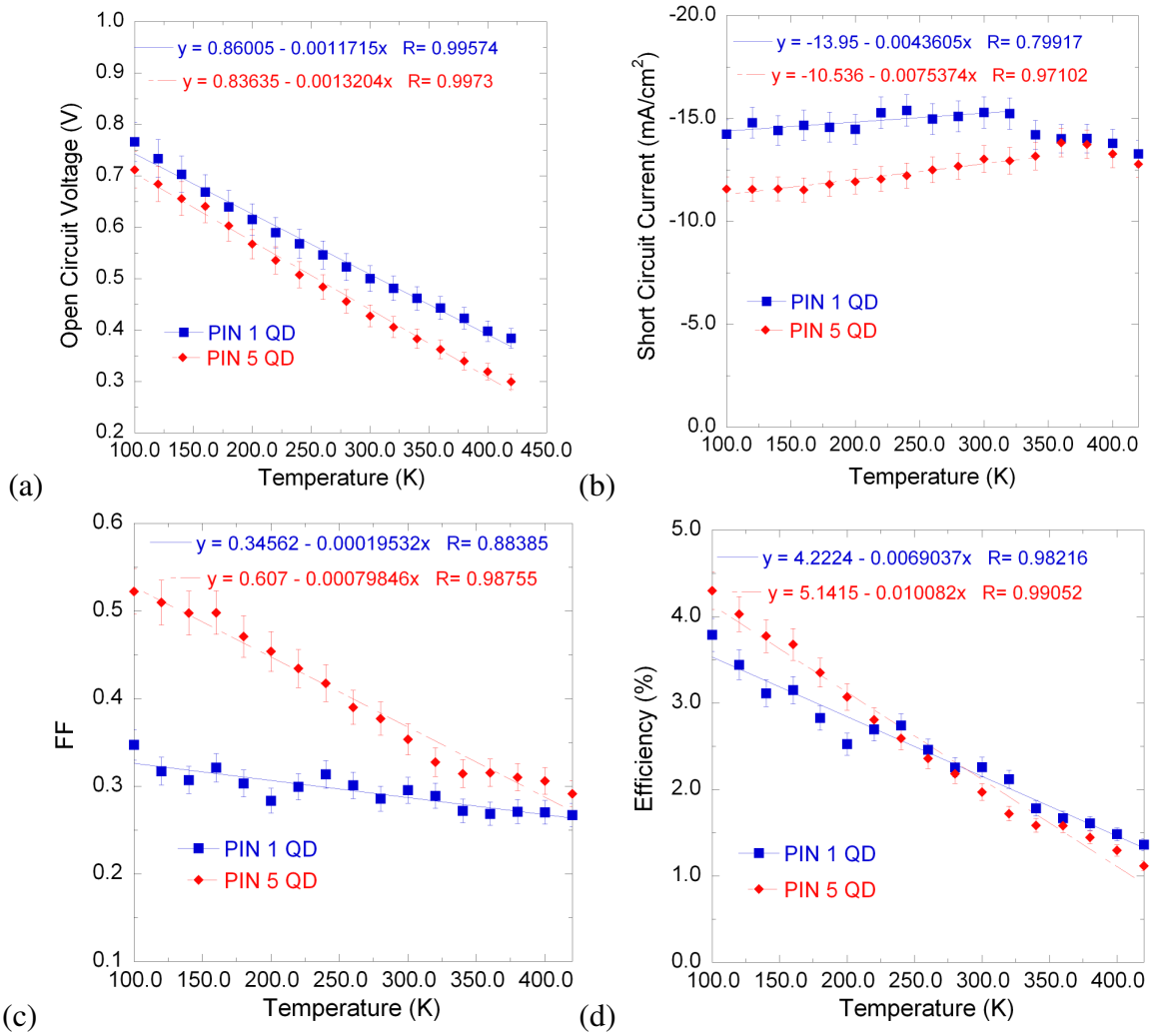

Figure 6.3. The (a) open circuit voltage, (b) short circuit density, (c) fill factor, and (d) efficiency of the QDSC containing 1-layer of InAs QDs (QD1) and the QDSC containing 5-layers of InAs QDs (QD5) as a function of temperature. The lines in the figures are linear curve fits, the equations of which are included in the figures.

A positive temperature coefficient is commonly observed in the J_{sc} of GaAs-based solar cells which is observed in the data depicted in Figure 6.3(b) for the temperature range of 100 K – 340 K. The increase in photocurrent with temperature may result from

improved minority carrier diffusion lengths in addition to the absorption edge moving to longer wavelengths. Reductions in *FF* with temperature, as shown in Figure 6.3(c), have been observed in GaAs-based devices in the past [105]. Although the J_{sc} increases with temperature, the decreased V_{oc} and *FF* offset its effect yielding a negative efficiency temperature coefficient. Typical values of $\Delta\eta/\Delta T$ for GaAs-based solar cells range from -0.02 to -0.03 %/°C [105]. These values are slightly greater than those obtained for the devices investigated here which are -0.0069 %/°C, and -0.010 %/°C for the 1QD, and 5QD devices, respectively.

6.1.2.2 RADIATION EFFECTS ON DEVICE OPERATION

The spectral responsivity of the two devices, along with a reference *pin* device (referred to as PIN) are overlaid in Figure 6.4a. This figure provides a comparison of the responsivity of the three devices; the PIN having a similar responsivity to that of the 1QD device. The 5QD device has a slightly reduced responsivity over the wavelength range corresponding to photon energies greater than the GaAs bandgap while subgap responsivity is observable. In the spectral responsivity of the three devices post 6.7×10^{11} alpha-particles/cm^2 (Figure 6.4b) similar rates of degradation in the responsivity of the devices are observed. However, the subgap responsivity of the 5QD device is more apparent in the Figure 6.4b indicating a lower rate of degradation in the InAs QD photocurrent generation in relation to the GaAs bulk.

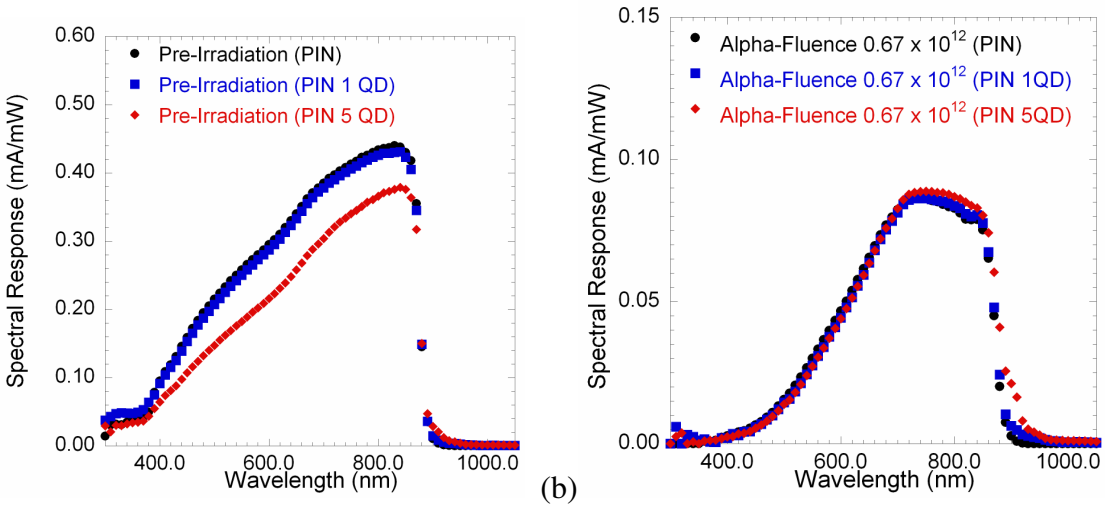

Figure 6.4. (a) Overlay of the pre-irradiated room temperature spectral responsivity of the PIN (black circles), 1QD (blue squares), 5QD (red diamonds), with respect to wavelength. In (b), the spectral responsivity of the three devices post 6.7×10^{11} alphas-particles/cm^2 is plotted with respect to wavelength.

The variation in the spectral responsivity at 830 nm, corresponding to the GaAs bulk responsivity, and at 900 nm corresponding to the InAs QDs are plotted as a function of alpha-particle fluence in Figure 6.5(a) and (b), respectively. The variations in the SR at 830 nm are similar in all three devices, all of which degrade by over 70% after the first alpha-particle dose. The 5QD device has the smallest relative SR change in reference to its beginning-of-life value. In comparison, the SR at 900 nm degraded by ~40% after the first dose in the 1QD device and by ~20% in the 5QD device when compared to their beginning-of-life values. This indicates a significant enhancement in the radiation tolerance associated with the InAs QDs as compared to the bulk GaAs responsivity. Furthermore, the InAs QD photogeneration is inherently linked to the bulk GaAs responsivity, since carriers in the QDs must traverse the junction in order to be collected [108]. Therefore, the reduction in the 900 nm InAs QD responsivity that is observed at high fluences may result from the junction degradation and not solely due to damage incurred in the QDs [108].

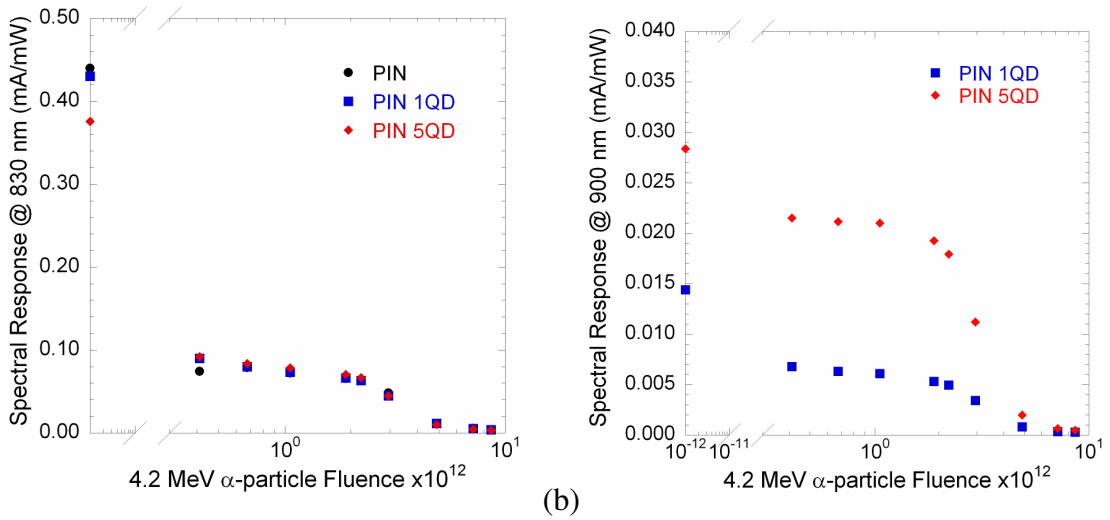

Figure 6.5. (a) The spectral responsivity at 830 nm as a function of alpha-particle fluence for the PIN device (black circles), 1QD device (blue squares), and 5QD device (red diamonds), which corresponds to the GaAs bulk responsivity. (b) The spectral responsivity at 900 nm as a function of alpha-particle fluence for the 1QD device (blue squares) and the 5QD device (red diamonds) which corresponds to the InAs QD responsivity.

The thermal dependent *J-V* and SR of GaAs-based InAs QDSC were measured. The dark current thermal dependence of the 1QD device displayed a typical GaAs solar cell thermal dependence over all the total range of temperature measured. In contrast, the 5QD device dark current transitioned from a tunneling dominated forward current mechanism to an injection or depletion region recombination current mechanism once the temperature increased beyond ~ 260 K. The *J-V* temperature coefficients under AM0 illumination were obtained for the QDSC which were found to be comparable to those reported previously for GaAs-based solar cells. The temperature dependent SR of the 5QD device indicated four peaks related to the InAs QD photogeneration. Two of the peaks showed a strong thermal dependence which indicates a thermal-assisted extraction process. Two other peaks, at slightly lower energy, were independent of temperature and suggest a 2-photon extraction process.

The variation in SR with alpha-particle irradiation was monitored in the devices. A comparison between the SR at wavelengths above and below the GaAs bandgap (*i.e.,* 830 nm, and 900 nm) allow the responsivity of bulk GaAs and InAs QDs, respectively, to be independently investigated. The SR at 830 nm degraded comparably in all three devices while the SR at 900 nm displayed a much slower rate of degradation. The slower rate of degradation observed in the subgap responsivity indicates an enhanced resilience of InAs QDs to alpha-particle irradiation.

6.2 STRAIN-COMPENSATED QDSC

The radiation and thermal dependence of strain compensated InAs QD / GaAs solar cells are now investigated. Strain compensation is a key step in realizing high-efficiency quantum dots solar cells (QDSC). InAs quantum dots (QDs) are grown using the Stranski-Krastanow growth mode which relies on a strain field, resulting from the mismatch between the InAs and the GaAs lattice parameters, to initiate three-dimensional growth. This three-dimensional growth, and subsequent QD generation does reduce the local strain within the QDs and surrounding GaAs material, but it is not completely eliminated. Therefore, as additional layers of InAs QDs are grown a significant tensile strain is built-up. During solar cell growth, this strain is naturally relieved by forming misfit boundaries and threading dislocations, which can damage the depletion region of the device. Strain relief is accomplished by growing the proper thickness of a compressively strained layer of GaP, between each successive QD array. The strain localized at the InAs QD / GaAs interface is still present, allowing for QD growth but the net strain on the stack becomes zero, mitigating defect generation. Figure 6.6a contains a schematic of the baseline GaAs *pin* device and the strain compensated InAs QD / GaAs

solar cell that were investigated. In Figure 6.6b, a schematic illustrating the electronic levels of the various materials in the strain compensated device, along with the possible charge carrier excitation mechanisms are depicted. The dashed colored lines represent the potential mini-band states that may be present in the device due to the overlap of the bound InAs QD states. A primary photon is required to populate these states followed by either photon assisted (secondary photon excites carriers out of wells) or thermal assisted electron extraction. The narrow spike between each well (quantum dot) corresponds to the wide bandgap GaP layer.

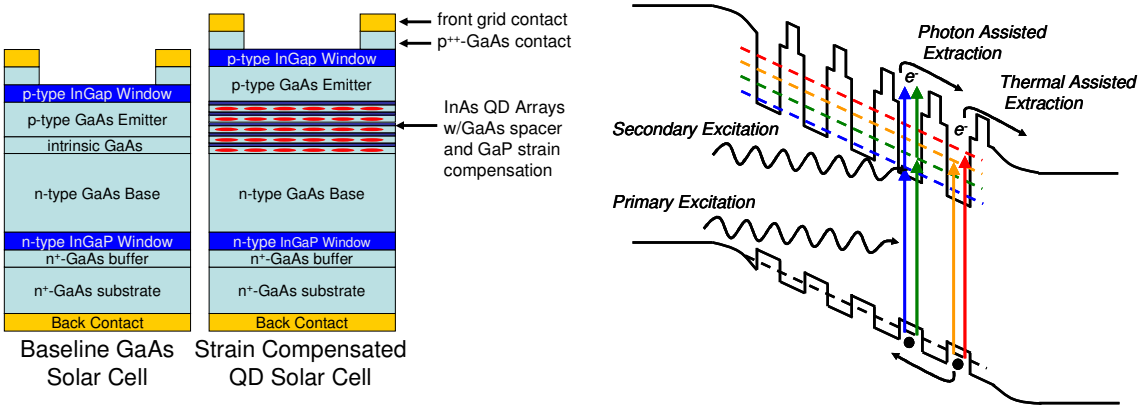

Figure 6.6. (a) Diagram depicting the baseline GaAs solar cell and the strain compensated QD solar cell structures. (b) Schematic depicting the energy bands of the strain compensated QD solar cell.

The thermal dependence of the QDSC, in relation to the baseline GaAs device, was as done above by monitoring both the AM0 current-voltage characteristics and SR over the range of 80 K – 400 K. It is important to note that the QDSC presented here has a room temperature AM0 efficiency in excess of 11% without anti-reflection coating.

The saturation current and ideality parameters were extracted from the dark current measurements assuming an ideal diode relationship. The dark current data for the two devices in addition to the variation in ideality and saturation current with temperature

are plotted in Figure 6.7a-d. This figure clearly illustrates that the thermal behavior of the QDSC is comparable to that of the baseline device response. Although the idealities parameters are slightly different (which could have been caused by cleaving the cells, poor contacts within the cryostat, etc.), the variation of this parameter with temperature is nearly identical for both devices. Furthermore, the saturation currents follow similar trends which can almost entirely be attributed to the temperature dependence of the GaAs bandgap narrowing. There is a slightly larger variation with temperature in the saturation current of the QDSC device but this is very minor. Furthermore, the very low saturation current observed at <150 K may be related to the wide-bandgap GaP layers which could reduce the carrier thermalization within the junction and hinder the transport of thermalized carriers through the junction.

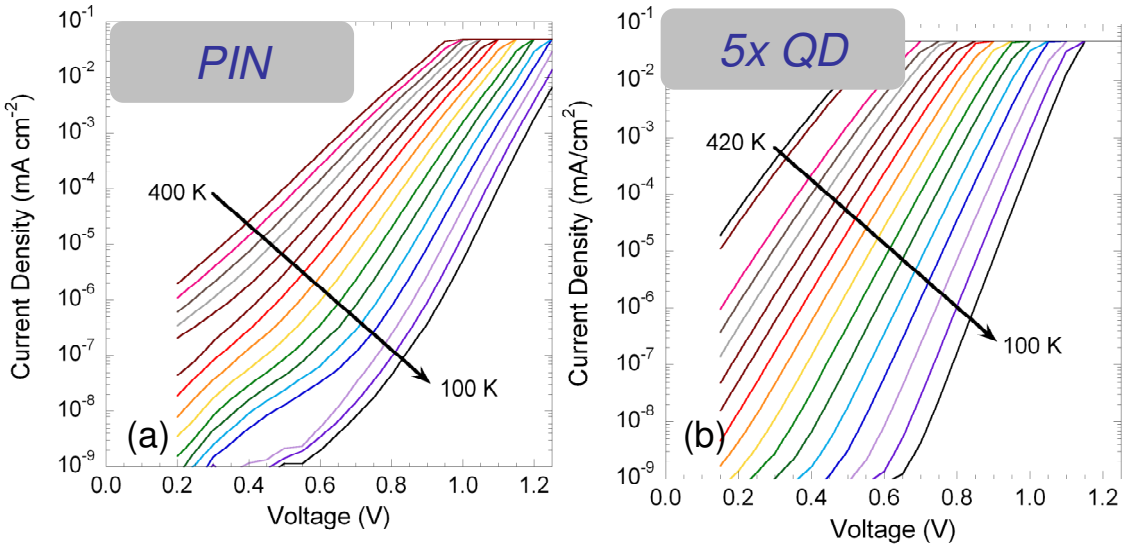

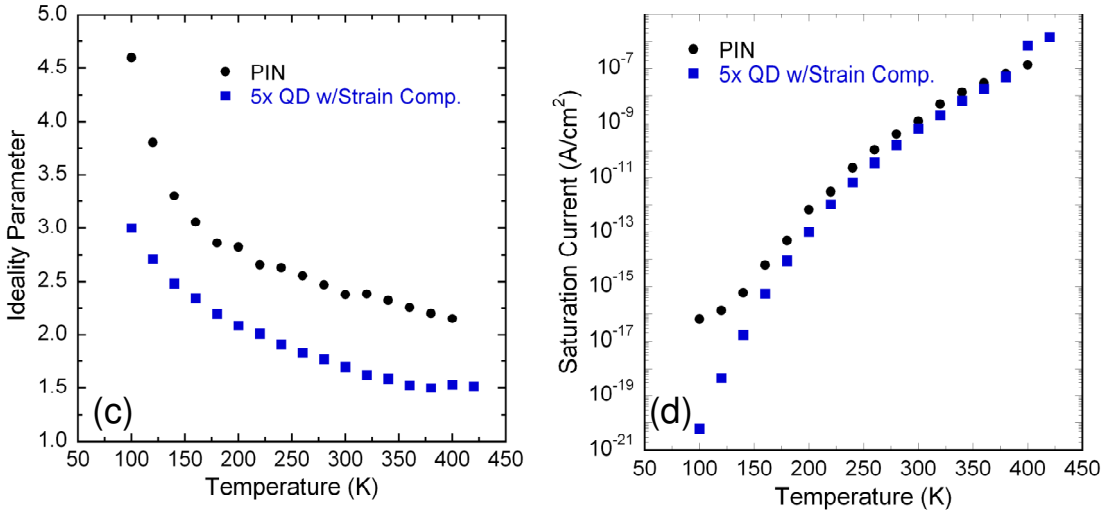

Figure 6.7. (a) Dark current-voltage response of baseline device and (b) the QDSC device over the temperature range of 100 – 400 K.(c) and (d) Extracted ideality and saturation currents as a function of temperature for the baseline device and the QDSC device, respectively.

The AM0 illuminated current-voltage response of the two devices is depicted in Figure 6.8a-b. These two devices again demonstrate similar temperature dependences, the main difference being the lower open circuit voltage observed in the QDSC device. There is a slightly greater slope in the V_{oc} of this device which is the result of the slightly greater saturation current temperature dependence observed in the dark characteristics of the device. As expected, the spectral responsivity of the devices showed nearly identical responses in the region of the spectrum which corresponds to phonons with energy greater than the GaAs bandgap (not shown).

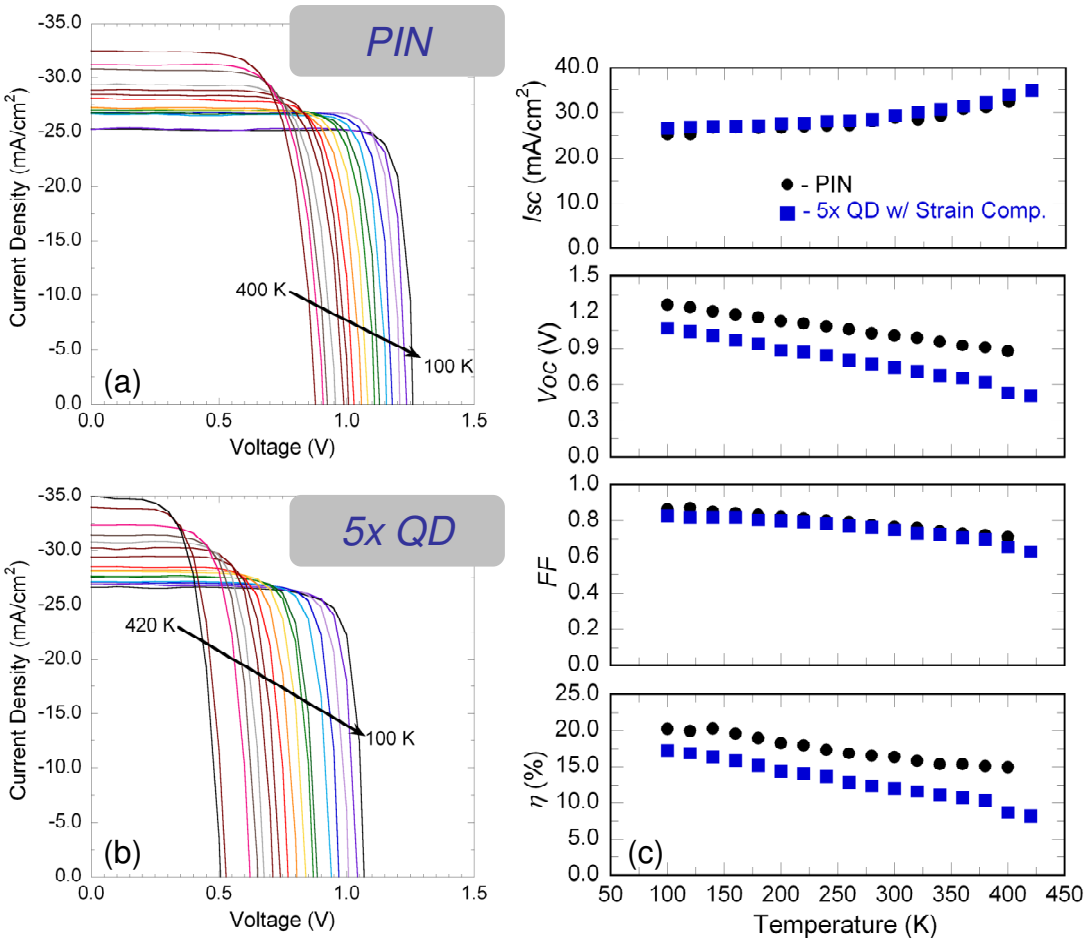

Figure 6.8. (a) and (b) contain the current-voltage response of the baseline GaAs device and the QDSC device, under simulated AM0 illumination, over the temperature range of 100 – 400 K, respectively. The summary data for these measurements are provided in part (c).

The InAs QD spectral responsivity variation with temperature is observable in the sub-gap responsivity of the QDSC as illustrated in Figure 6.9a. Also included in this figure is the sub-gap responsivity of the baseline device at 100 K and 420 K, which envelop the QDSC device responsivity at shorter wavelengths. At longer wavelengths the InAs QD photoconversion can be observed and in particular, multiple peaks are present (labeled E1-E3) which result from the excited QD states or mini-band states within the InAs QD 5-layer stack. The electroluminescence, in Figure 6.9b illustrates the variation in the ground state, E1, of the InAs QD array with temperature. This emission

is the result of injecting carriers into the junction of the device, a total current of 200 mA/cm^2 was applied. The alignment of the electroluminescence with that of the spectral responsivity of the device confirms that the responsivity observed at these wavelengths is the result of the QDs. Interestingly, the intensity of the electroluminescence greatly reduces as the temperature is increased (over 4 orders of magnitude in going from 100 K – 420 K) meaning carriers are able to transit the junction without recombining, or other recombination mechanisms dominate their lifetimes. Based on the observed reduction in electroluminescence, one may expect an increase in the spectral responsivity at the same wavelengths if the carriers are being extracted through thermalization. Such an increase is not observed in the spectral responsivity of the QDSC device as temperature rises, which suggests that carrier thermalization is not the primary mechanism of carrier extraction.

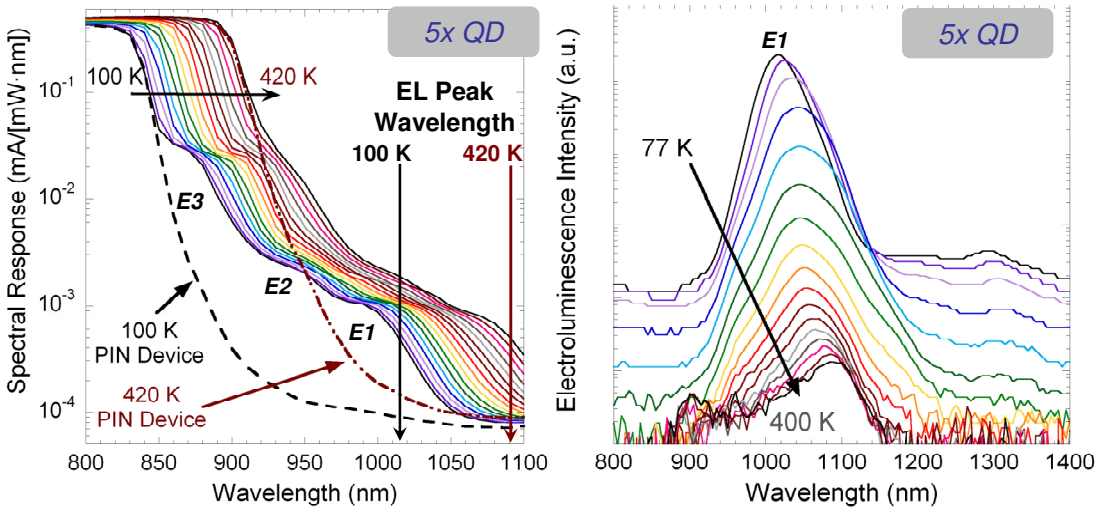

Figure 6.9. (a) Spectral responsivity of the QDSC over the sub-GaAs bandgap range depicting the variation in the InAs QD responsivity with temperature. For comparison, the 100 K and 420 K spectral responsivity of the baseline GaAs device have been overlaid as dashed and dot-dash lines and the location of the electroluminescence peak emission are included. (b) The variation in the electroluminescence spectrum of the QDSC over the temperature ranging from 77 – 400 K.

The radiation response of the two devices was investigated by measuring the room temperature spectral responsivity and the current-voltage characteristics (AM0 illumination) as a function of alpha-particle irradiation. The irradiation source was a 1 mCi ^{210}Po alpha-particle emitter with an area of ~2.5 cm^2. The variation of the two devices in the visible region is very similar, wherein a greater rate of reduction is observed in the longer-wavelength region of the spectra (see Figure 6.10a,b). This suggests that the lifetime (and diffusion length) of holes in the base is reduced by the radiation induced defects making it less probable for them to diffuse to the junction when generated deep within the base.

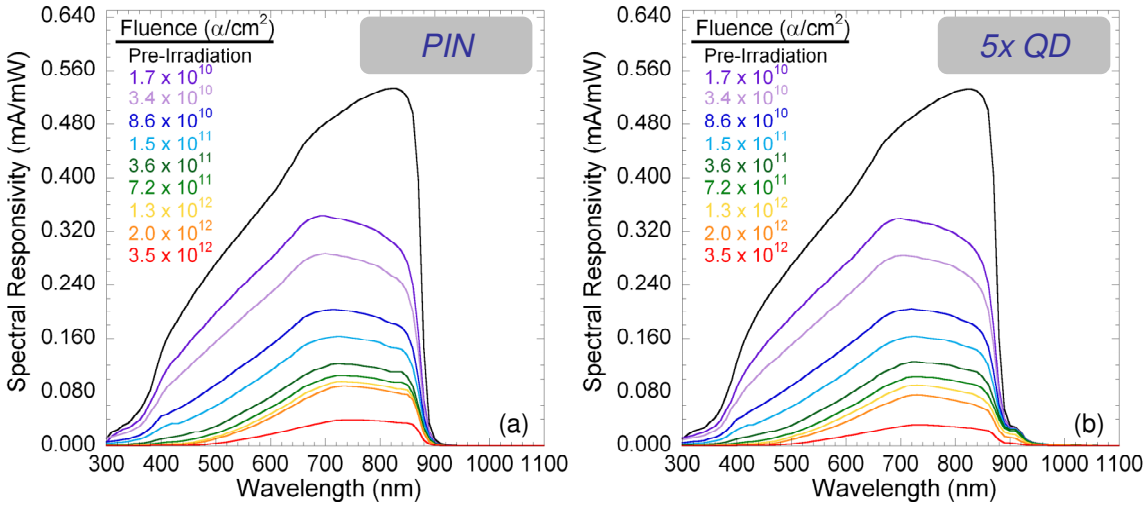

Figure 6.10. Spectral responsivity spectra for (a) the baseline device and (b) the QDSC device for various levels of alpha-particle fluence.

The sub-gap region of the QDSC spectral responsivity for increasing levels of fluence are depicted in Figure 6.11a, along with the pre-irradiation and post 3.5×10^{12} alpha-particles / cm^2 spectral responsivity curves for the baseline device. Pre-irradiation, the two devices demonstrate very similar spectral responsivities up to ~880 nm at which point the responsivity of the baseline device drops towards zero, while the responsivity of the QDSC is maintained as a result of the InAs QDs. For low-levels of fluence, the peak

InAs QD responsivity peak shows little variation, but at very high fluences, it does decline significantly. Although the InAs QDs can be damaged by the alpha-particles, generation of defects within the GaAs barriers and the subsequent junction degradation will inherently contribute to the degradation observed in the measured spectral responsivity data. Even with these combined effects, the InAs QD degradation rate is much lower than that of the bulk GaAs. This may be the result of the strain within the InAs QDs, which will be discussed in the following section.

The increased V_{oc} observed in the strain compensated QDSC, over that of the non-compensated QDSC device previously investigated, suggests that the concentration of defects within the junction has been significantly reduced by the strain compensation layers. It was originally suggested that the presence of such defects could reduce the rate of degradation in the device. Based on the current device performance, it appears that the defects were not the main contributor to the radiation tolerance observed in that device. Figure 6.11b contains the spectral responsivity as a function of fluence measured at 830 nm for both devices and at 910 nm for the QDSC, which further illustrates the high tolerance observed in the InAs QD portion of the spectra.

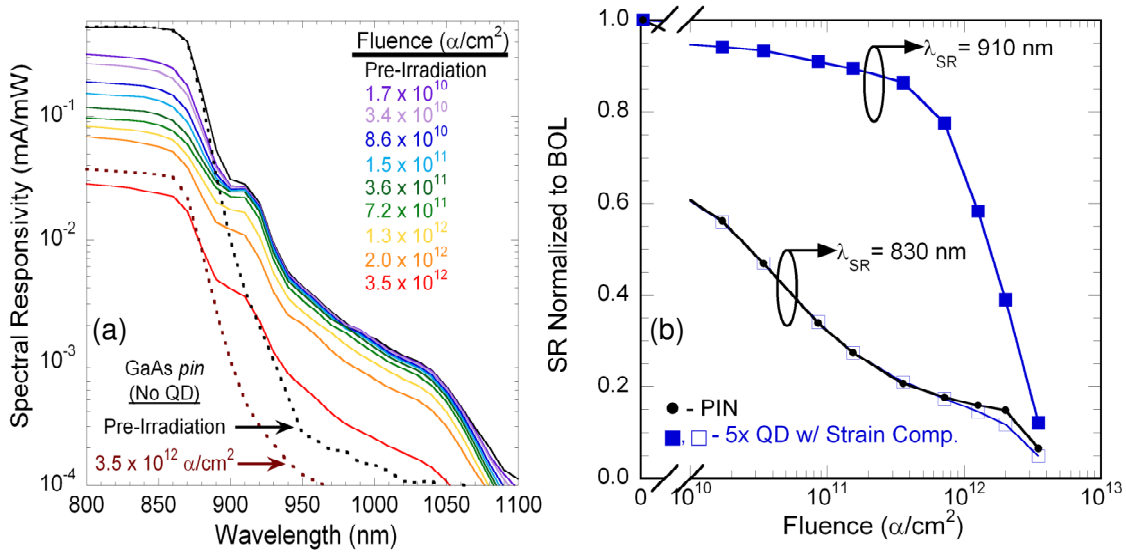

Figure 6.11. (a) Spectral responsivity of the QDSC at incremental levels of alpha-particle fluence; the pre-irradiation and post 3.5 x 10^{12} alpha-particle/cm^2 responsivity spectra of the baseline device are overlaid for comparison. (b) The spectral responsivity as a function of fluence measured at 830 nm for both devices and at 910 nm for the QDSC.

The variations in the normalized I_{sc}, V_{oc}, FF, and Efficiency with fluence are provided in Figure 6.12, for the baseline and the QDSC devices. The QDSC maintains a much greater normalized V_{oc} as compared to the baseline devices which suggests that the QDs are improving the tolerance of the overall device not just in the sub-gap spectral responsivity. This improved V_{oc} leads to a greater normalized efficiency than that of the baseline device until a fluence of ~1 x 10^{12} alpha-particles/cm^2, at which point both devices have degraded to less than 5% of their beginning-of-life efficiency. The noticeable difference observed in the two devices is the decreased normalized fill factor observed in the QDSC device. The fundamental cause of this is still under investigation.

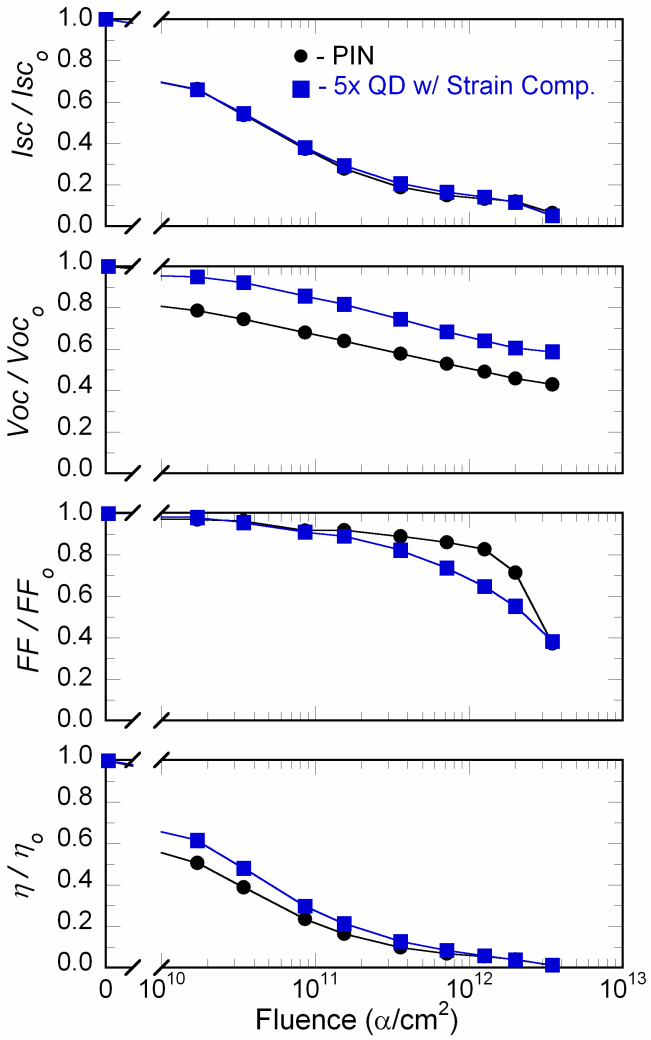

Figure 6.12. Normalized short circuit current, open circuit voltage, fill factor, and efficiency with alpha-particle fluence for the baseline and the QDSC devices.

In conclusion, the thermal and radiation dependence of a strain compensated InAs QD / GaAs solar cells have been invested in reference to a baseline GaAs device. The thermal dependence of the two devices is nearly identical and certainly within the sample-to-sample variation. Increased resilience in the V_{oc} and the sub-GaAs responsivity of the QDSC was observed in the experimental results of the InAs QD /GaAs solar cell exposed to alpha-particle irradiation.

6.3 STRAIN EFFECTS ON THRESHOLD ENERGY

As discussed in Chapter 3, the threshold energy for atomic displacement E_{th} dictates the level of non-ionizing damage that will be incurred by a semiconductor under irradiation. Just a small increase in E_{th} has a large effect on the total number of defects generated by a particle because the energy lost by the particle to the PKO and all subsequent collision events the PKO has with neighboring atoms requires more energy to create a defect. For instance, increasing the E_{th} of In and As atoms from 4.0 eV to 4.5 eV in a SRIM simulation of 5 MeV alpha-particles in InAs reduces the number of vacancies per alpha-particle from ~1800 to ~1650 [11, 57]. This corresponds to a reduction in vacancy generation by over 8%. The observed enhancement in radiation tolerance of the InAs QDs within the GaAs solar cells, therefore, suggests that there may be some physical property that is increasing the E_{th} within this material system. Besides the smaller size, the main property associated with these materials is the large compressive strain field which exists within the QDs [45, 49, 50]. With the use of the Tersoff interatomic potentials, the effect that a compressive strain field has on E_{th} is investigated.

This investigation is initiated by populating an InAs lattice with In and As atoms situated at their equilibrium positions, corresponding to a lattice parameter of 6.058 Å (see Figure 6.13a) [75]. An In or As atom is chosen as the PKO situated at the (0,0,0) lattice position and the cohesive energy of the atom situated at this site is calculated by summing over the neighboring bonds as defined by the Tersoff potential model. A value of -3.107 eV is obtained which is consistent with the literature values [75-77]. As depicted in Figure 6.13b-f, the atom is then stepped throughout the lattice and at each point the cohesive energy of the atom is re-calculated. Initially, the goal is to determine

the location of the interstitial sites, and the energy associated with those sites. An interstitial site may be defined as a local potential energy minimum, and can be found by plotting equi-potential surfaces with increasing energy. As depicted in Figure 6.14 the interstitial sites surround the basis atom situated at the (a/4, a/4, a/4) lattice position. In this figure the interstitial sites for an As atom in the InAs lattice are depicted. A similar result is obtained for In although the energy and location of the sites are different. Differences arise because the In-In and As-As bonding have different energies associated with them.

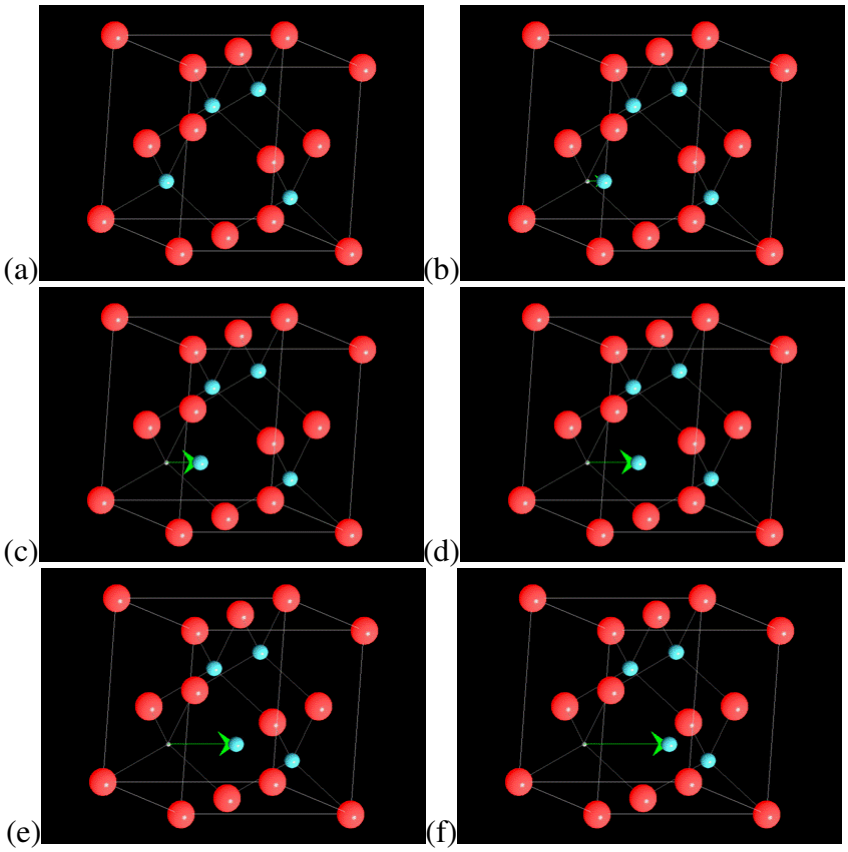

Figure 6.13. (a) Zinc blend bonding structure of InAs, where In and As atoms are represented by blue and red spheres, respectively. (b)-(f) Depictions of the simulation process where an In (As) is displaced from its equilibrium bonding sight into points locations within the lattice. At each displacement, the potential energy of the atom is calculated.

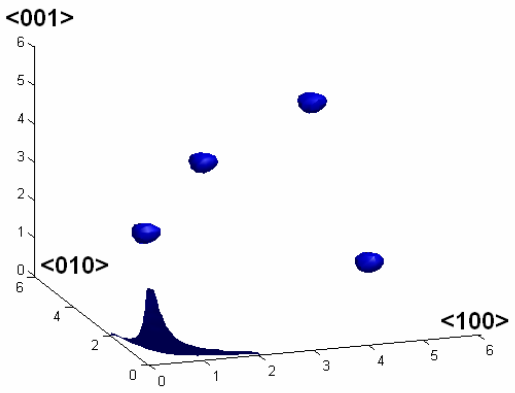

Figure 6.14. Equi-potential surfaces indicating the locations of local minima for As within the InAs lattice. Moving from left to right, the four blue spheres correspond approximately with the following crystal locations (x,y,z) = (a/4,3a/4,a/4), (a/4,a/4,3a/4), (3a/4,3a/4,3a/4), and (3a/4,a/4,a/4). The surface near (0,0,0) corresponds to the top of the well (in energy) that the atom sits when in its equilibrium position. An In atom is located at (a/4,a/4,a/4) and therefore these four interstitial sites surround that atom.

The threshold for displacement for a given direction, $E_{th,\boldsymbol{r}}$, where $\boldsymbol{r}$ is the displacement vector, is now defined as the maximum energy encountered along $\boldsymbol{r}$ before reaching a local minimum. For example, the black trace in Figure 6.15 depicts the potential energy of an In atom as it is displaced along the (201) direction towards an interstitial site near (a,0,a/2). Along this path, the atom approaches the face atom on the (100) plane, this causes the energy of the atom to peak at a displacement of ~ 4.2 Å before reaching the interstitial site. The difference between the peak energy and the energy of the atom at the equilibrium bonding site corresponds to the $E_{th,\boldsymbol{r}}$ for this particular value of $\boldsymbol{r}$.

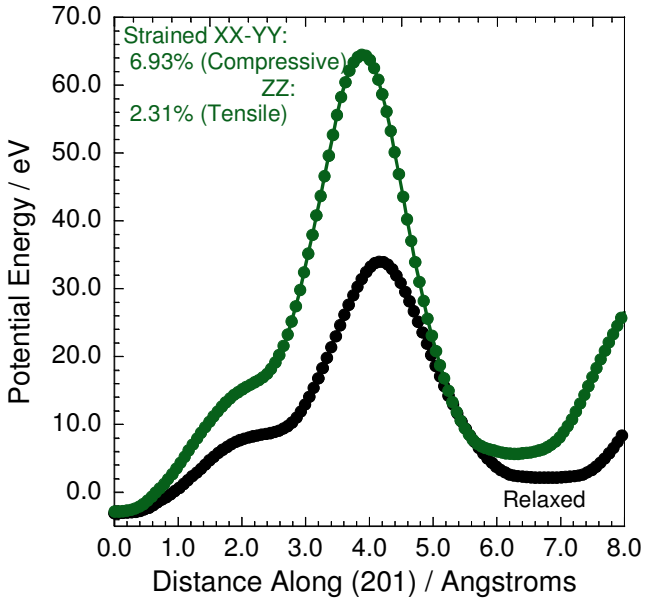

Figure 6.15. Potential energy of an Indium PKO along $\boldsymbol{r}$ = (201) for a relaxed InAs lattice (black trace) and a strained lattice (green trace).

Figure 6.15 also contains a trace depicting the effect of strain on the potential energy encountered by the atom along the same path. To simulate a strained InAs lattice, a compressive strain of ~7% in the x and y directions was assumed based on the difference in lattice parameters between InAs and GaAs. Additionally, the compressive strain in the x and y directions will cause the lattice to expand in the z-direction and for that a Poisson's ratio of 1/3 was assumed yielding a tensile strain of ~2.3 % in the z-direction. Strain has a profound effect on the $E_{th,\boldsymbol{r}}$, along this direction. It is increased by over a factor of 2, and the energy of the interstitial site is also increased.

The above example illustrates the large affect that strain has on the threshold energy for displacement. However, the strain in quantum dots is not constant; theoretical calculations have predicted the strain to range from a maximum of ~7% compressive at the base of the quantum dot and slowly relax becoming slightly tensile at the peak (this was predicted for pyramidal InAs QDs on GaAs [45]). The effect of strain on the cohesive (potential) energy of the atom occupying its equilibrium site is depicted in

Figure 6.16. As expected, the equilibrium energy increases with increasing strain indicating that the lattice is no longer arranged in the minimum energy configuration.

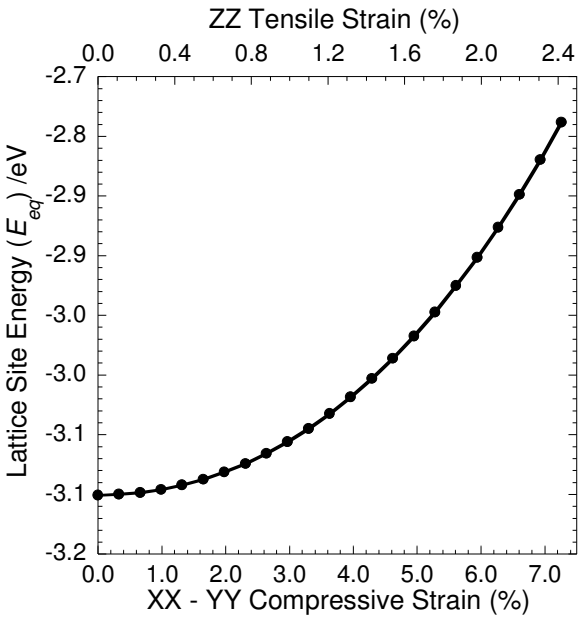

Figure 6.16. Effect of strain on the equilibrium lattice cohesive energy of the atom.

Furthermore, the effect of varying the strain on the knock-out energy lower bound for In and As PKOs reaching the specified interstitial site are depicted in Figure 6.17a and b, respectfully. In both cases increasing strain results in a slightly non-linear increase in the lower bound on the $E_{th,\boldsymbol{r}}$ which is defined as the difference between the interstitial site energy and the equilibrium bonding site energy. This means the energy associated with the atoms occupying interstitial sites increases a greater rate than that of the (0,0,0) site energy depicted above. This is considered the lower bound on the $E_{th,\boldsymbol{r}}$ because it is the minimum amount of energy required to force the PKO into the interstitial location while still conserving energy.

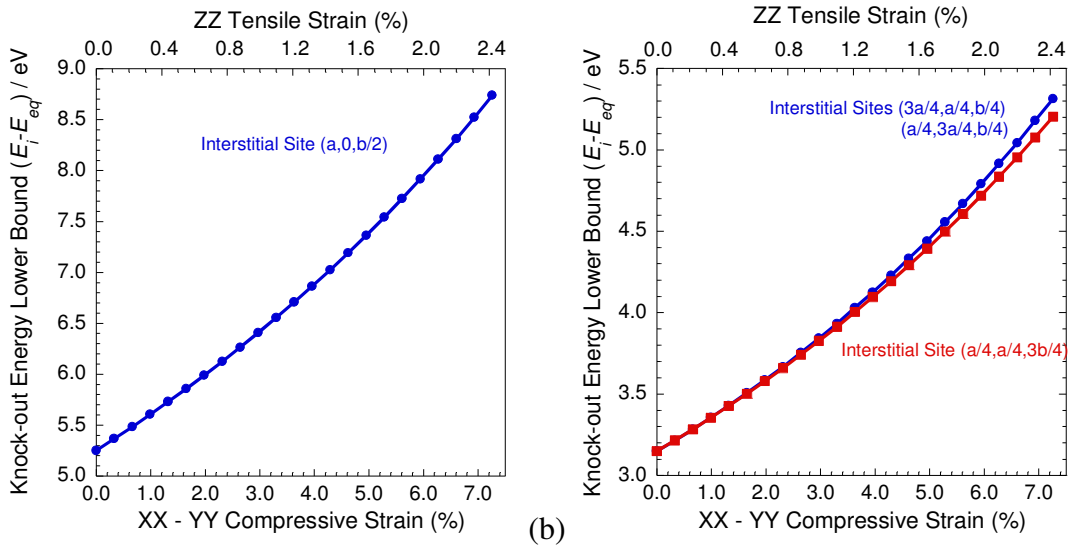

Figure 6.17. Effect of strain on the minimum knock-out energy required to reach the labeled interstitial sites for (a) In and (b) As as the PKO.

The above results have provided convincing arguments that strain has a large impact on the minimum energy to displace an atom. However, to determine the actual E_{th}, which is the minimum of all $E_{th,r}$, the peak energy encountered by a PKO along all possible directions must be considered. A methodology for performing this calculation is described here. To begin, a spherical coordinate system (r, ϕ, θ) is employed for the displacement of the atoms within the lattice. This allows all unique directions in the lattice to be investigated simply by varying ϕ and θ over π and π /2, respectively. For each set of ϕ and θ, the PKO is translated linearly along r. To determine the $E_{th,r}$ a criteria can then be defined. For illustrative purposes, the following criteria have been chosen. First, the atom must be at a location which is beyond one interatomic spacing distance from the (0,0,0) site. This eliminates the possibility that un-stable defects (local minima) near the (0,0,0) are chosen. Secondly, the peak energy is then defined as the maximum energy encountered prior to a reduction in potential energy after reaching one interatomic distance from the (0,0,0) site. Many different criteria may be chosen in this

methodology depending on the type of irradiating particle and the expected amount of energy imparted to the PKO.

An example of the results which can be obtained from this methodology is depicted in Figure 6.18. This figure contains a contour plot of the log of the minimum displacement energy ($E_{th,r}$) as a function of ϕ and θ direction for an In PKO in InAs. Also listed on the plot are the typical lattice directions which correspond to single points on this figure. For example, the [100] corresponds to the point $\phi = 0$ and $\theta = 90$ point. Along this direction there is an atom situated one bond-length away and therefore the figure is red in this directing indicating that a large potential energy is required to cause a displacement. A similar trend is observed for all traditional lattice directions, wherein a red region indicates the presence of an atom along that path (at least within the first lattice cell). Also apparent in the figure is a drastically different potential energy profile encountered depending on whether the PKO is directed towards the positive or negative y-direction (*i.e.,* positive or negative ϕ). In the positive ϕ direction the basis atom of the PKO is nearby, situated at the (a/4,a/4,a/4) lattice site. This atom greatly limits the ability of the PKO to be displaced into this octant of the lattice, except for displacements surrounding this atom. This is consistent with the results depicted in Figure 6.14 above, where the locations of the interstitial sites surround this basis atom. In the negative ϕ direction the situation is reversed. The atom can easily be displaced in the [1 $\bar{1}$ 1] but encounters neighboring atoms surrounding those directions. These results provide theoretical evidence confirming the experimentally observed anisotropic defect introduction in GaAs in which it was shown that there is an "easy" and a "hard" [111] direction for displacement of Ga and As within GaAs [109]. The abrupt variation in the

threshold energy that is observed when crossing from the negative to positive ϕ region of the contour plots is a consequence of the interstitial sites in these locations being at different radial distances from the equilibrium position.

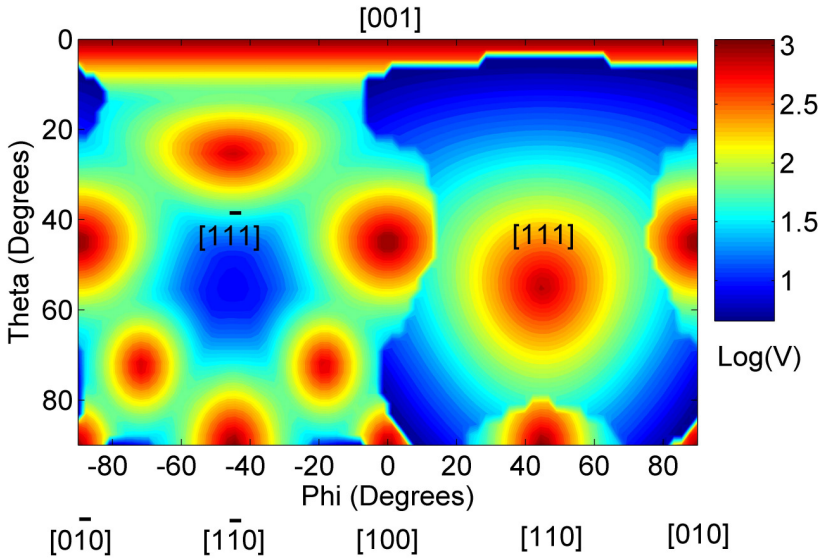

Figure 6.18. Contour map depicting the log of the minimum energy for displacement along direction (ϕ, θ) for an In PKO in relaxed InAs.

The effects of strain on minimum energy displacement for In in an InAs lattice under ~7% in-plane compressive strain along with the associated z-directed 2.3% tensile strain is depicted in Figure 6.19. The tensile strain in the z-direction is immediately evidenced by the larger blue region directed above the [111]. Furthermore, the shape of the minimum energy direction near the [1 $\bar{1}$ 1] appears to be deformed, resembling a slight rotation, and the exact locations of the red regions "atoms" have shifted from their corresponding location on the relaxed contour plot.

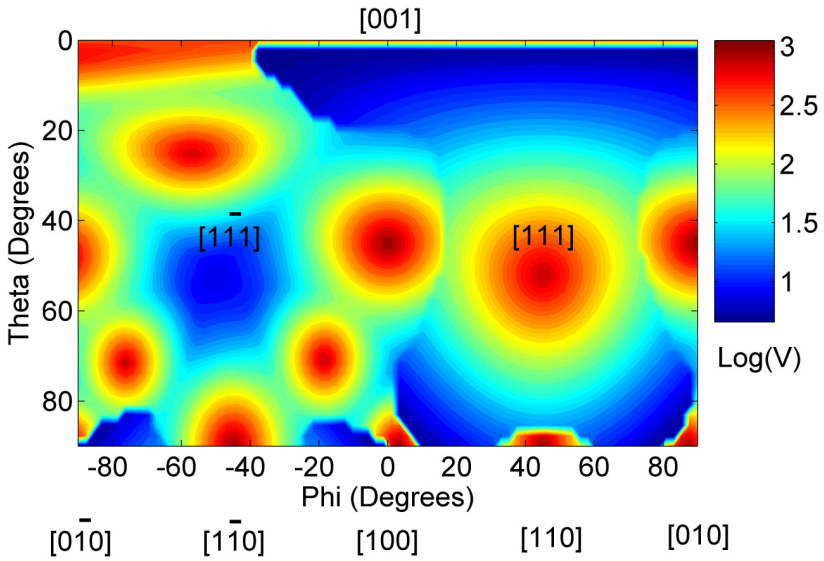

Figure 6.19. Contour map depicting the log of the minimum energy for displacement along direction (ϕ, θ) for an In PKO in InAs under ~7% xx-yy compressive strain and ~2.3% zz tensile strain.

Besides structural information, data regarding the E_{th} can also be ascertained from this methodology. Taking the minimum energy of all points associated with each of the above two figures yields E_{th} values of 3.75 eV and 4.53 eV, respectively. This corresponds to an increase in over 0.75 eV per vacancy generation which corresponds to a reduction in vacancies generated by irradiation alpha particles more than 10%. Similar results are obtained for As when comparing the strained and relaxed lattices. Simulations in which the criteria was set to find the maximum energy encountered along a translation of 10.5 Å yielded E_{th} values of 16.48 eV and 19.12 eV for the relaxed and strained InAs cases, respectively. These result support the conjecture that the increased radiation tolerance observed in InAs QDs grown on GaAs is fundamentally linked to strain induced increases in E_{th} for In and As PKOs.

6.4 VALIDATION OF D^3P MODEL

In Chapter 3 it was noted that main utility of the displacement damage dose D_d methodology is the independence of the D_d on the particle type. This means that the effects of non-ionizing radiation caused by one particle type could be used to estimate the damage caused by other particles provided the *NIEL* of the two particles were known. It also implies that the performance degradation caused by two different irradiation particles can be normalized based on D_d and yield similar degradation results. To that end, the effects of proton irradiation on the performance of QD solar cells have been compared to those observed under irradiation from an isotropic alpha particle radioisotope source on comparable devices as described above.

Proton irradiation on baseline and QD devices with the same structure as that depicted in Figure 6.6a were performed at International Photonics Consultants. For these measurements, five baseline and QD solar cells were characterized prior to proton irradiation and subsequently irradiated with 4.5 MeV protons at a dose of ~ 1×10^9 to 1×10^{14} protons / cm^2. Each cell was irradiated with a different dose, and subsequently re-characterized. Characterization consisted of standard current vs. voltage measurements under simulated AM0 illumination.

Determination of the displacement damage dose imparted by a collimated proton beam consists of multiplying the proton fluence with the average non-ionizing energy loss *NIEL* of the particle within the active region of the device. The average *NIEL* can be used as long as the particle energy remains nearly constant while traversing through the device. The value of *NIEL* calculated for 4.5 MeV protons in GaAs was 1.85×10^{-2} $MeVcm^2/g$, and is consistent with that reported in the literature [15]. Determining the

displacement damage dose from an isotope alpha particle source is slightly more complex since the alpha particles traverse the active region of the devices with deferent energies. To do so, Equation 3.15 was used to determine the D^3P. This generates the spatial profile depicting the location of the *NIEL* within the top 20 µm of the device provided in Figure 6.20. The region of the D^3P profile which corresponds to the active volume of the device (roughly the top 2.5 µm) is subsequently integrated to determine the total D_d imparted into the device for each incremental alpha-particle dose.

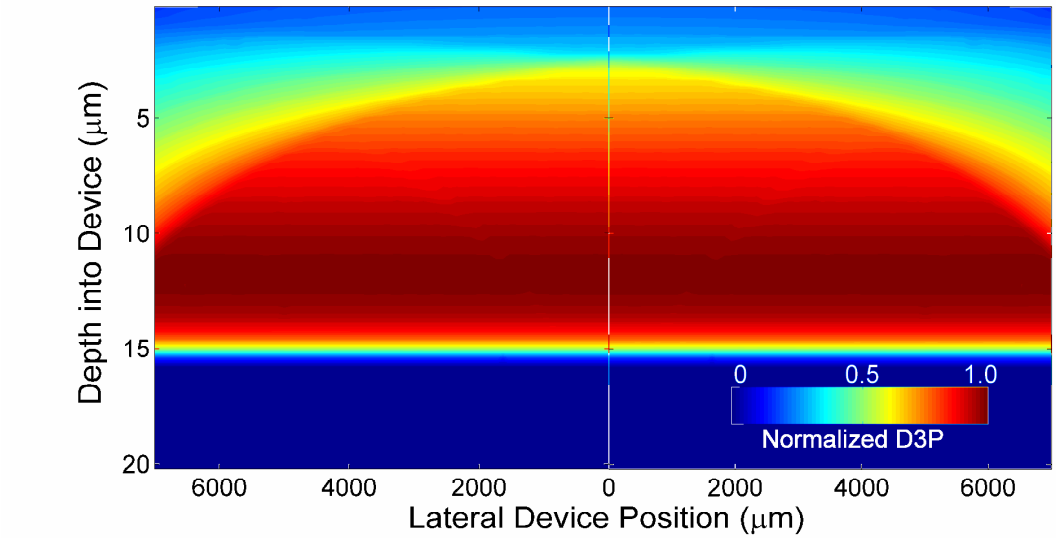

Figure 6.20. D^3P of alpha-particles in the top 20 µm of a GaAs solar cell. The intensity of the profile has been normalized to allow for rapid comparison of regions.

Figure 6.21a below depicts the variation in open circuit voltage of the quantum dot devices under proton (red circle) and alpha-particle (green triangles) irradiation in reference to their corresponding baseline devices (black square and blue triangle), respectively. As shown above in Figure 6.12, the V_{oc} in the 5x QD devices is much more resilient to displacement damage and results in a 10x reduction in the rate of V_{oc} degradation. This effect is observed in these devices under both proton and alpha particle irradiation. Such strong correlation between these values implies that the methodology

employed for calculating the D_d induced by alpha-particles is valid. This strong correlation between the two methodologies is again observed in the variation in short circuit current when normalized to D_d in Figure 6.21b.

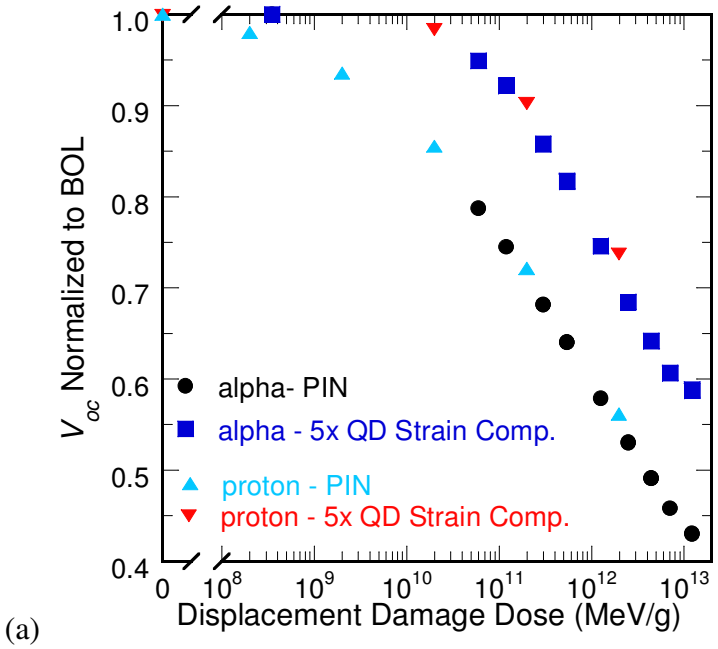

(a)

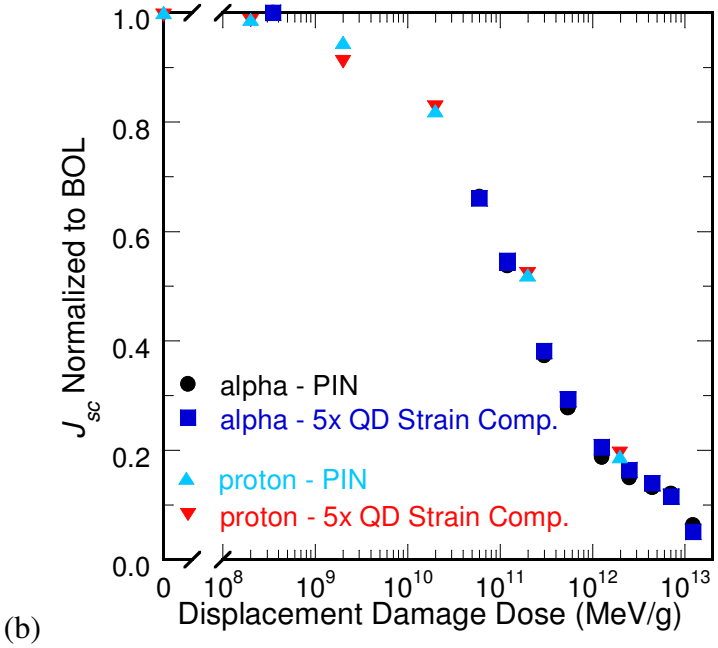

(b)

Figure 6.21. (a) Degradation in open circuit voltage, and (b) short circuit current with increasing displacement damage dose for the 5x quantum dot devices and baseline devices under both proton and alpha particle irradiation.

The above results again confirm the enhanced radiation tolerance observed in InAs QD / GaAs solar cells. Furthermore, the strong correlation between the proton and alpha-particle irradiation data, when normalized to D_d, validate the D^3P solar cell damage modeling approach for isotropic alpha-particle irradiation.

CHAPTER 7. CONCLUSION

Devices based on III-V semiconductors and nanomaterials are expected to be critical components of future microsystems as the demand for greater functionality, range of application, and robustness continue to increase. In particular, the superior optoelectronic properties and radiation tolerance of these materials make them ideal for use in power generation devices including radioisotope batteries and solar cells, both of which capitalize on their unique characteristics. The research presented here has addressed these needs both experimentally and theoretically, focusing on the fundamental aspects associated with the ionizing and non-ionizing effects of high energy particle irradiation on III-V semiconductors devices and nanomaterials.

Chapter 2 provided the background for this research. The fundamental radiation – matter interactions were reviewed, with an emphasis on alpha, beta, and gamma radiation. A review of all published direct and indirect conversion radioisotope batteries based on solid state devices was provided. This review captured the state of the field for this type of miniature power generation device and also provided insight regarding the critical issues with this technology. In particular, the key aspects of the solid state converter necessary to achieve high efficiency devices include high shunt resistance, low dark current, high tolerance to ionizing radiation, and a large nuclear absorption cross section. Many of these needs can be addressed simply by using devices fabricated with wide energy bandgap semiconductors. Chapter 2 also provided a summary of nanomaterials, and a solid-state device in which nanomaterials can be incorporated to improve the device performance. Nanomaterials have unique optoelectronic properties

resulting from quantum confinement and their small scale also suggests additional benefits including improved thermal behavior and high radiation tolerance.

The theoretical aspects associated with this research were presented in Chapter 3. A model used to determine the ionizing (*ADEP*) and non-ionizing (D^3P) energy loss imparted to a III-V semiconductor device from an isotropically emitting alpha-particle source was developed. These models are critical tools for designing radioisotope batteries as they determine the spatial distribution of energy deposited within the semiconductor device emitted from an isotropic source. These models where primarily applied to $InGaP_2$ diodes throughout the dissertation; however, the methodology is completely general and can be used to design devices comprised of a plurality of semiconductor and metallic layers. This modeling approach utilizes Monte Carlo software to generate a characteristic rate of ionizing and non-ionizing energy loss of alpha-particles in a material of choice. The spatial energy deposition within a material emitted from an isotropic source is subsequently calculated numerically. This approach greatly reduces the time required to model these devices since only 20,000 simulated particles are needed in contrast to the 10^6 to 10^7 simulated particles needed to determine the spatial energy deposition profile using simulation alone.

The D^3P modeling approach is an extension of the *ADEP* model and applies to the non-ionizing energy loss imparted to a semiconductor diode. This modeling approach is an extension to the Naval Research Laboratory's (NRL) displacement damage dose methodology as the D^3P determines the spatial distribution of the defect-generating energy imparted to the semiconductor; the NRL methodology does not provide any spatial information. Used in conjunction, the *ADEP* and D^3P are the necessary modeling

tools for designing and analyzing the performance of radioisotope batteries and will be critical for designing next generation devices comprised of various absorbers and three-dimensional layered structures.

Chapter 4 detailed the development of a novel *nipi* structured radioisotope battery designed to capture the necessary aspects of an ideal solid state power conversion device, including a wide bandgap semiconductor, the use of drift fields to improve carrier extraction, and a wide nuclear absorption cross section to improve power output and efficiency. Initial results were obtained using single junction $InGaP_2$ *nip* devices. An η_{semi} of 3.2% was achieved by an $InGaP_2$ diode excited by an 1 mCi ^{210}Po source which was the second highest conversion efficiency reported at that time. Through a series of measurements on this device (each within increasing source / device distance), the *ADEP* modeling approach was validated by verifying that the output short circuit current was directly proportional to the calculated (via *ADEP* model) input power. The proportionality constant was defined as the alpha-response and is analogous to the spectral response of photodiodes under monochromatic excitation. The *ADEP* model results were subsequently used as input parameters for a lump parameter equivalent circuit model which simulates the current voltage characteristics of *nipi*-diodes. The equivalent circuit model consists of many *nip* and *pin* devices connected in parallel and excited by a constant current source determined from the *ADEP* model. The results indicate that for an $InGaP_2$ *nipi*-diode 14 junctions yield the maximum conversion efficiency and under a 300 mCi/cm^2 alpha particle flux, a power output of 2 mW/cm^2 is achievable given a 4π geometry is employed.

The lessons learned from the experimental results on single junction devices, and from the theoretical modeling were applied to prototyping a *nipi*-diode based on the GaAs III-V semiconductor material system. The development of this device included mask set design (5 lithographic layers), V-groove etching studies, and a smart metallization process. A *nipi*-diode solar cell, consisting of a triple junction GaAs device, was successfully fabricated and demonstrated 3.2 % conversion efficiency under simulated AM0 illumination. In the best device, a short circuit current density of 20.7 mA/cm^2 and an open circuit voltage of 0.35 V was obtained. This is the first demonstration of a *nipi*-diode photovoltaic device and shows promise for this device structure as a radioisotope battery and as a solar cell. The device suffered from a lower open circuit voltage than that common among GaAs solar cells (1.03 V is typical under 1-sun AM0 illumination) and may suggest leakage at the metal contacts. Future development in this area may include ion implantation or re-growth in the contact regions to improve the rectification thereby increasing the V_{oc}.

Chapter 5 focused on the nanophosphor development for use as an intermediate absorber layer in an indirect conversion radioisotope battery. Colloidal quantum dots (CdSe, InP) were synthesized and tested under alpha-particle flux to investigate their light output. The rapid degradation upon exposure to air (after crashing from solution and casting onto a quartz slide) prohibited the measurement of radioluminesce output. The use of cladding layers may reduce the air sensitivity although such rapid degradation makes these materials unlikely candidates for radioisotope batteries. A procedure for doping the colloidal quantum dots with rare-earth elements was also explored but did not improve the radioluminescence output. Nanophosphors comprised of $Y_2O_3:Eu^{3+}$ (and

also Ce, Tb, and Er) were developed and showed strong radioluminescence under alpha-particle irradiation in addition to improved radiation resilience as compared to a commercially obtained ZnS:Ag^{2+} phosphor material. Co-doping the Y_2O_3 material system was shown to yield a material system with improved radioluminescence efficiency. A prototype radioisotope battery consisting of a Y_2O_3:Eu^{3+} phosphor and an $InGaP_2$ diode was investigated. Nearly ideal matching between the phosphor emission and the peak spectral responsivity of the $InGaP_2$ diode was observed. Under irradiation by an alpha-particle source a power output of approximately 19 nW/cm^2 was demonstrated with a conversion efficiency of ~2.4% (it should be noted that some alpha-particles may have penetrated the phosphor and thus contributed to the power output). The increased radiation tolerance observed in the phosphors over that of the $InGaP_2$ diodes has the potential of increasing the lifetime of the indirect conversion radioisotope batteries by a factor of 10 over comparable direct conversion devices. However the use of alpha-particle emitting radioisotopes greatly limits the operation lifetime of the devices regardless of the conversion scheme employed.

The research presented in this dissertation has identified many successful methods for both increasing the efficiency and longevity of radioisotope microbatteries. The functional integration with microsystems will, however, require a number of technical and practical considerations to first be addressed. Naturally, the power output of the device must be matched to that required by the microsystem; more power can be achieved by increasing the size or by coupling it with a capacitor to allow for pulsed operation. An additional technical consideration consists of properly shielding the device to ensure trace-level radiation emission does not cause single event errors in nearby

integrated circuits. A major consideration for future radioisotope microbatteries is the choice of radioisotope source. The rate of damage which it causes in the device needs to be balanced with the half-life and maximum power it can deliver. A practical consideration concerns the cost and availability of the radioisotope sources. Many radioisotopes may meet the power and lifetime requirements but excessive cost may make them infeasible. In most cases, the potential environmental or health issues associated with radioisotopes will be mitigated prior to deployment, since low-level emissions are very detrimental to the operation of integrated circuits. However, social skepticism will remain as a major impediment, limiting the wide-scale commercialization of these devices. Instead, the primary niche that radioisotope microbatteries can fulfill is one which requires long-term operation, in excess of 2 years. As such, it is expected that radioisotope batteries will first be adopted for military or space applications where long-life and small size are required, and cost is less of a concern. As conversion efficiencies of the radioisotope converters (either solid-state or others) increase and the necessary radioisotope sources become available, applications requiring a long-term power supply will welcome their arrival.

In Chapter 6, the focus of the research shifted towards understanding the thermal dependence and radiation tolerance of epitaxially grown InAs QDs and GaAs-based InAs QD solar cells. These properties were measured in QD solar cells with and without strain compensation layers. In both instances, the thermal dependence of the QD devices was shown to be consistent with the dependence observed in the baseline devices. In contrast, the QD solar cells demonstrated improved radiation tolerance over that of the baseline devices, characterized primarily by a more resilient open circuit voltage. Spectral

responsivity measurements were used to independently investigate the effects of alpha-particle irradiation on the lifetime of the GaAs and InAs QD related photocurrent generation. These measurements revealed a profound enhancement in the radiation tolerance of InAs QDs as the rate of degradation in the sub-GaAs bandgap photogenerated current degraded less rapidly. A methodology employing the Tersoff potential energy model was developed to investigate the effects of strain on the minimum knockout energy of In and As atoms within an InAs lattice. The results indicate that the inherent strain within InAs QDs grown using the Stranski-Krastanow growth mode significantly increases the minimum energy required to create a lattice defect. The minimum required to displace an indium atom by 10.5 Å from its equilibrium site location increased from 16.5 eV to 19.1 eV when the InAs lattice was under a 7% compress xx-yy strain and a 3.5% tensile zz strain. An increase in the minimum displacement energy was shown to reduce the number of defects generated by each incident alpha particle and therefore is directly related to the increased radiation tolerance observed in the experimental results. The natural extension of this work is to convert the Tersoff potential energy model into a full molecular dynamics simulation. Such a model could provide full collision cascade information and may also be used to observe the mobility of defects (vacancies, interstitials, and antisite) to determine if the variable strain field with the quantum dots leads to an enhanced rate of defect healing or segregation of defects at crystal grain boundaries.

The experimental and theoretical results presented here may potentially lead to new fields of research. Engineering of strained semiconductor devices, through the incorporation of InAs QDs or other compressively strained materials, may be effective at

increasing the radiation tolerance of a variety of devices thereby making them applicable for harsh radiation environments. Furthermore, with the increased tolerance being related to a reduction in defect generation within the material, strain engineering through the incorporation of nanomaterials may lead to improved device reliability and increased lifetime under high power operation. The inhibition of the dark-line defect formation in strained InGaAs/AlGaAs quantum well lasers may be evidence of these potential benefits (for example see: R. G. Waters, *et al.*, *IEEE Photon. Tech. Lett*., 2(8), 1990, 531-533). The D^3P modeling approach developed provides spatial information regarding the defect generation within devices. Such information can lead to a better understanding of radiation damage within semiconductor devices, leading to additional enhancements to be achieved.

REFERENCES

[1] J. W. Gardner, V. K. Varadan, and O. O. Awadelkarim, *Microsensors MEMS and Smart Devices*. Chichester: John Wiley & Sons, LTD, 2001, pp. 503.

[2] B. S. Blanchard and W. J. Fabrycky, *Systems engineering and analysis. Third edition*. United States: Prentice Hall, Inc., Upper Saddle River, NJ (United States), 1998, pp. 752.

[3] D. F. Lemmerhirt and K. D. Wise, "Chip-Scale Integration of Data-Gathering Microsystems," *Proceedings of the IEEE*, 2006, 22.

[4] D. Streit, *III-Vs Review*, vol. 17(8), pp. 22, 2004.

[5] C.-m. Wang, S.-C. Huang, W.-K. Huang, and Y.-m. Hsin, *Solid-State Electron.*, vol. 52, pp. 49-52, 2008.

[6] R. R. King, D. C. Law, K. M. Edmondson, C. M. Fetzer, G. S. Kinsey, H. Yoon, R. A. Sherif, and N. H. Karam, *Applied Physics Letters*, vol. 90(18), pp. 183516, 2007.

[7] M. Shubhrangshu, B. Koushik, G. Siddhartha, P. Elena, R. Jean Baptiste, K. Sanjay, and G. Christoph, *Applied Physics Letters*, vol. 91(24), pp. 241111, 2007.

[8] F. Faccio and G. Cervelli, *IEEE Trans. Nucl. Sci.*, vol. 52(6), pp. 2413-2420, 2005.

[9] R. L. Pease, A. H. Johnston, and J. L. Azarewicz, "Radiation Testing of Semiconductor Devices for Space Electronics," *Proceedings of IEEE*, 1988, 1510-1526.

[10] K. S. Krane, *Introductory Nuclear Physics*. New York: John Wiley & Sons, 1988, pp. 845.

[11] J. F. Ziegler, J. P. Biersack, and U. Littmark, *The Stopping and Range of Ions in Solids*, vol. 1. New York: Pergamon Press, 1985.

[12] B. Liu, D. Alvarez-Ossa, N. P. Kherani, S. Zukotynski, and K. P. Chen, *Sensors Journal, IEEE*, vol. 7(6), pp. 917, 2007.

[13] K. E. Bower, Y. A. Barbanel, Y. G. Shreter, and G. W. Bohnert, "Polymers, Phosphors, and Voltaics for Radioisotope Microbatteries," vol. 1. Boca Raton: CRC Press, 2002.

[14] R. J. Walters, M. A. Xapsos, H. L. Cotal, S. R. Messenger, G. P. Summers, P. R. Sharps, and M. L. Timmons, *Solid-State Electron.*, vol. 42(9), pp. 1747-1756, 1998.

[15] R. J. Walters, G. P. Summers, and S. R. Messenger, *28th PVSC*, pp. 1092 - 1097, 2000.

[16] R. J. Walters, S. R. Messenger, G. P. Summers, M. J. Romero, M. M. Al-Jassim, D. Araujo, and R. Garcia, *J. Appl. Phys.*, vol. 90(7), pp. 3558-3565, 2001.

[17] R. J. Walters, S. R. Messenger, H. L. Cotal, and G. P. Summers, *J. Appl. Phys.*, vol. 80(8), pp. 4315-4321, 1996.

[18] R. P. Raffaelle, C. D. Cress, D. M. Wilt, and S. G. Bailey, "Radiation Degradation of Nanomaterials," *Proceedings of Fall 2005 MRS Research Symposium*, 2006, 147-157.

[19] H. J. Möller, *Semiconductors for Solar Cells*. Boston: Artech House, Inc., 1993.

[20] L. M. Unger and D. K. Trubey, "Specific Gamma-Ray Dose Constants for Nuclides Important to Dosimetry and Radiological Assessment," U. S. D. O. Energy, Ed.: Oak Ridge National Laboratory, 1982.
[21] W. Ehrenberg, C.-S. Lang, and R. West, *Proc. Phys. Soc. A*, vol. 64, pp. 424, 1951.
[22] K. G. McKay, *Physical Review*, vol. 84(4), pp. 829, 1951.
[23] P. Rappaport, *Physical Review*, vol. 93(1), pp. 246, 1954.
[24] W. G. Pfann and W. v. Roosbroeck, *J. Appl. Phys.*, vol. 25(11), pp. 1422-1434, 1954.
[25] L. D. Posey, "Alpha-particle bombardment of Si and GaAs diodes: energy covnersion and radiation damage," U.S. Atomic Energy Commision, 1965.
[26] H. Flicker, J. J. Loferski, and T. S. Elleman, *IEEE Trans. Elect. Dev.*, vol. 11(1), pp. 2-8, 1964.
[27] R. H. Barnes, R. L. Ritzman, J. F. Kircher, and D. N. Sunderman, "Fabrication Studies of ^{147}Pm betavoltaic batteries," U.S. Atomic Energy Commision, 1965.
[28] L. C. Olsen, *Energy Conversion*, vol. 13(4), pp. 117-127, 1973.
[29] F. Huffman and J. C. Norman, *Chest*, vol. 65(6), pp. 667-672, 1974.
[30] R. J. Walko, R. C. Lincoln, W. E. Baca, S. H. Goods, and G. H. Negley, "Tritium Fueled Betacells," *Proceedings of 26th International Energy Conversion Engineering Conference*, 1991, 135-140.
[31] P. E. Sims, L. C. DiNetta, and A. M. Barnett, "High-efficiency GaP power conversion for betavoltaic applications," *Proceedings of XIII Space Photovoltaic Resarch and Technology Conference*, 1994, 373-382.
[32] T. Kosteski, N. P. Kherani, G. Gaspari, S. Zukotynski, and W. T. Shmayda, *J. Vac. Sci. Technol. A*, vol. 16(2), pp. 893-896, 1997.
[33] S. Deus, "Tritium-powered betavoltaic cells based on amorphous silicon," *Proceedings of the 28th IEEE Photovoltaic Specialists Conference*, 2000, 1246.
[34] V. M. Andreev, A. G. Kevetsky, V. S. Kaiinovsky, V. P. Khvostikov, V. R. Larionov, V. D. Rumyantsev, M. Z. Shvarts, E. V. Yakimova, and V. A. Ustinov, "Tritium-powered betacells based on $Al_xGa_{1-x}As$," *Proceedings of the 28th IEEE Photovoltaic Specialists Conference*, 2000, 1253.
[35] G. Rybicki, C. Vargas-Aburto, and R. Uribe, "Silicon Carbide Alphavoltaic Battery," *Proceedings of the 25th Photovoltaic Specialists Conference*, 1996, 93–96.
[36] J. P. Fleurial, G. J. Snyder, J. Patel, C. K. Huang, M. A. Ryan, R. Averback, C. Hill, and G. Chen, "Solid-state power generation and cooling micro/nanodevices for distributed system architectures," *Proceedings of Thermoelectrics, 2001. Proceedings ICT 2001. XX International Conference on*, 2001, 24.
[37] C. D. Cress, B. J. Landi, D. M. Wilt, and R. P. Raffaelle, *J. Appl. Phys.*, vol. 100, pp. 114519(1-5), 2006.
[38] C. D. Cress, B. J. Landi, and R. P. Raffaelle, *IEEE Trans. Nucl. Sci.*, vol. To Appear, 4-08, 2008.
[39] H. Guo and A. Lal, "Nanopower betavoltaic microbatteries," *Proceedings of the 12th IEEE TRANSDUCERS: International Conference on, Solid-State Sensors, Actuators and Microsystems*, 2003, 36.

[40] W. Sun, N. P. Kherani, K. D. Hirschman, L. L. Gadeken, and P. M. Fauchet, *Advanced Materials*, vol. 17(10), pp. 1230-1233, 2005.
[41] M. V. S. Chandrashekhar, C. I. Thomas, H. Li, M. G. Spencer, and A. Lal, *Appl. Phys. Lett.*, vol. 88, pp. 033506(1-3), 2006.
[42] C. J. Eiting, V. Krishnamoorthy, S. Rodgers, T. George, J. D. Robertson, and J. Brockman, *Appl. Phys. Lett.*, vol. 88, pp. 064101(1-3), 2006.
[43] G. Cao, *Nanostructures & nanomaterials: synthesis, properties & applications*. London: Imperial College Press, 2004.
[44] C. Kittel, *Introduction to Solid State Physics*, 7th ed: John Wiley & Sons, Inc., 1996, pp. 673.
[45] D. Bimberg, M. Grundmann, and N. N. Lednetsov, *Quantum Dot Heterostructures*, vol. 1. Chichester: John Wiley and Sons, 1999.
[46] A. Luque and A. Martí, *Phys. Rev. Lett.*, vol. 78(26), pp. 5014-5017, 1997.
[47] W. Shockley and H. J. Quieser, *J. Appl. Phys.*, vol. 32, pp. 510-519, 1961.
[48] R. P. Raffaelle, S. Sinharoy, J. Andersen, D. M. Wilt, and S. G. Bailey, "Multi-Junction Solar Cell Spectral Tuning with Quantum Dots," *Proceedings of World Conference on Photovoltaic Energy Conversion*, 2006, 162-166.
[49] S. M. Hubbard, D. M. Wilt, S. Bailey, D. Byrnes, and R. P. Raffaelle, "OMVPE Grown InAs Quantum Dots for Application in Nanostructured Photovoltaics," *Proceedings of Proc. of the World Conference on Photovoltaic Energy Conversion*, 2006, 118-121.
[50] S. M. Hubbard, R. P. Raffaelle, R. Robinson, C. Bailey, D. M. Wilt, D. Wolford, W. Maurer, and S. Bailey, "Growth and Characterization of InAs Quantum Dot Enhanced Photovoltaic Devices," *Proceedings of Proc. of the Materials Research Society Spring Meeting*, 2007.
[51] W. V. Schoenfeld, C.-H. Chen, P. M. Petroff, and E. L. Hu, *Appl. Phys. Lett.*, vol. 73(20), pp. 3, 1998.
[52] P. G. Piva, R. D. Goldberg, I. V. Mitchell, D. Labrie, R. Leon, S. Charbonneau, Z. R. Wasilewski, and S. Fafard, *Appl. Phys. Lett.*, vol. 77(5), pp. 3, 2000.
[53] R. Leon, G. M. Swift, B. Magness, W. A. Taylor, Y. S. Tang, K. L. Wang, P.Dowd, and Y. H. Zhang, *Appl. Phys. Lett.*, vol. 76(15), pp. 3, 2000.
[54] R. Leon, S. Marcinkevicius, J. Siegert, B. Cechavicius, B. Magness, W. Taylor, and C. Lobo, *IEEE Trans. Nuc. Sci.*, vol. 49(6), pp. 2002, 2002.
[55] F. Guffarth, R. Heitz, M. Geller, C. Kapteyn, H. Born, R. Sellin, A. Hoffmann, D. Bimberg, N. A. Sobolev, and M. C. Carmo, *Appl. Phys. Lett.*, vol. 82(12), pp. 3, 2003.
[56] C. W. Colerico, H. B. Serreze, S. R. Messenger, M. A. Xapsos, and E. A. Burke, *IEEE Trans. Nuc. Sci.*, vol. 42(6), pp. 2089-2094, 1995.
[57] J. F. Ziegler, *J. Appl. Phys. / Rev. Appl. Phys.*, vol. 85, pp. 1249-1272, 1999.
[58] http://www.srim.org/SREM.htm.
[59] H.-C. Lee, *Introduction to Color Imaging Science*. Cambridge: Cambridge University Press, 2005, pp. 716.
[60] S. R. Messenger, E. A. Burke, G. P. Summers, and M. A. Xapsos, *IEEE Trans. Nucl. Sci.*, vol. 46(6), pp. 1595-1602, 1999.
[61] E. A. Burke, *IEEE Trans. Nuc. Sci.*, vol. 33, pp. 1276, 1986.

[62] G. P. Summers, E. A. Burke, C. J. Dale, E. A. Wolicki, P. W. Marshall, and M. A. Gehlhausen, *IEEE Trans. Nucl. Sci.*, vol. 34, pp. 1134, 1987.
[63] G. P. Summers, E. A. Burke, M. A. Xapsos, C. J. Dale, P. W. Marshall, and E. L. Petersen, *IEEE Trans. Elect. Dev.*, vol. 35, pp. 1221, 1987.
[64] H. Y. Tada, J. R. CarterJr., B. E. Anspaugh, and R. G. Downing, *The Solar Cell Radiation Handbook*, 3rd ed: NASA/JPL Publ., 1982.
[65] H. Flicker, J. J. Loferski, and J. Scott-Monck, *Physical Review*, vol. 128(6), pp. 2557, 1962.
[66] J. J. Loferski and P. Rappaport, *Physical Review*, vol. 111(2), pp. 432, 1958.
[67] C. Erginsoy, G. H. Vineyard, and A. Englert, *Physical Review*, vol. 133(2A), pp. A595, 1964.
[68] C. Erginsoy, G. H. Vineyard, and A. Shimizu, *Physical Review*, vol. 139(1A), pp. A118, 1965.
[69] P. N. Keating, *Physical Review*, vol. 145(2), pp. 637, 1966.
[70] M. J. P. Musgrave and J. A. Pople, *Proc. Roy. Soc.*, vol. 474, pp. A268, 1962.
[71] F. H. Stillinger and T. A. Weber, *Physical Review B*, vol. 31(8), pp. 5262, 1985.
[72] J. Tersoff, *Physical Review Letters*, vol. 56(6), pp. 632, 1986.
[73] J. Tersoff, *Physical Review B*, vol. 37(12), pp. 6991, 1988.
[74] J. Tersoff, *Phys. Rev. B.*, vol. 39 (8), 1989.
[75] P. A. Ashu, J.H.Jefferson, A.G.Cullis, W. E. Hagston, and C. R. Whitehouse, *J. Crystal Growth*, vol. 150, pp. 176-179, 1995.
[76] M. A. Migliorato, A. G. Cullis, M. Fearn, and J. H. Jefferson, *Phys. Rev. B.*, vol. 65, pp. 115316, 2002.
[77] K. Albe, K. Nordlund, J. Nord, and A. Kuronen, *Physical Review B*, vol. 66(3), pp. 035205, 2002.
[78] W. Shockley, "Research and investigations of inverse epitaxial UHF power transistor," in *Report No. AL-TOR-64-207*: Air Force Atomic Laboratory, Wright-Patterson Air Force Base, Ohio, September, 1964.
[79] S. G. Bailey, N. S. Fatemi, G. R. Landis, D. M. Wilt, R. D. Thomas, and A. Arrison, "A V-Grooved GaAs Solar Cell," *Proceedings of the 20th IEEE Photovoltaic Specialists Conference*, Las Vegas, Nevada, 1988.
[80] R. Williams, *Modern GaAs Processing Techniques*, 2nd ed. Norwood, MA: Artech House, Inc., 1990.
[81] R. P. Raffaelle, P. Jenkins, D. Wilt, D. Scheiman, D. Chubb, and S. Castro, "Alpha voltaic batteries and methods thereof," in *U.S. Pat. Appl. Publ*. USA: US 20050231064, 2005.
[82] R. Leon, S. Marcinkevicius, J. Siegert, B. Cechavicius, B. Magness, W. Taylor, and C. Lobo, *IEEE Trans. Nuc. Sci.*, vol. 49(6), pp. 2844-2851, 2002.
[83] R. Leon, G. M. Swift, B. Magness, W. A. Taylor, Y. S. Tang, K. L. Wang, P. Dowd, and Y. H. Zhang, *Appl. Phys. Lett.*, vol. 76(15), pp. 2074-2076, 2000.
[84] P. G. Piva, R. D. Goldberg, I. V. Mitchell, D. Labrie, R. Leon, S. Charbonneau, Z. R. Wasilewski, and S. Fafard, *Appl. Phys. Lett.*, vol. 77(5), pp. 624-626, 2000.
[85] L. Ozawa and M. Itoh, *Chemical Reviews*, vol. 103(10), pp. 3836-3855, 2003.
[86] G. H. Dieke, *Spectra and Energy Levels of Rare Earth Ions in Crystals*. New York: Interscience, 1968, pp. 401.

[87] S. Shionoya and W. M. Yen, "Phosphor Handbook," vol. 1, 2 ed. Boca Raton: CRC Press, 1999.
[88] K. Krane, *Modern Physics*. New York: John Wiley & Sons, Inc., 1996, pp. 581.
[89] P. Reiss, S. Carayon, and J. Bleuse, *Physica E: Low-dim. Sys. and Nanostructures*, vol. 17, pp. 95-96, 2003.
[90] B. J. Landi,"Quantum dot-single wall carbon nanotube complexes for tunable optoelectronic microsystems sensors," Ph.D. Dissertation, *Rochester Inst. Tech.*, Rochester, NY, 2006.
[91] D. W. Lucey, D. J. MacRae, M. Furis, Y. Sahoo, A. N. Cartwright, and P. N. Prasad, *Chem. Mater*, vol. 17, pp. 3754-3762, 2005.
[92] S. Kumar, R. Thomann, and T. Nann, *J. Mater. Res.*, vol. 21(3), pp. 543-546, 2006.
[93] C. B. Murray, D. J. Norris, and M. J. Bawendi, *J. Am. Chem. Soc.*, vol. 15, pp. 8706, 1993.
[94] T. Nann and J. Riegler, *Chem Eur. J.*, vol. 8, pp. 4791, 2002.
[95] D. Battaglia and X. Peng, *Nano. Lett.*, vol. 2, pp. 1027, 2002.
[96] C. J. Murphy, *Anal. Chem.*, vol. 74, pp. 520A-526A, 2002.
[97] T. Trindade, P. O'Brien, and N. L. Pickett, *Chem. Mater.*, vol. 13, pp. 3843-3858, 2001.
[98] A. Anctil,"Nanomaterials for organic solar cells," Master's Thesis, *Rochester Inst. Tech.*, Rochester, NY, 2007.
[99] C. D. Cress, C. S. Redino, B. J. Landi, and R. P. Raffaelle, *J. Solid State Chem.*, vol. doi:10.1016/j.jssc.2008.04.024, 2008.
[100] S. Kurtz, D. Friedman, J. Geisz, and W. McMahon, *J. Crystal Growth*, vol. 298, pp. 748-753, 2007.
[101] V. Aroutiounian, S. Petrosyan, A. Khachatryan, and K. Touryan, *J. Appl. Phys.*, vol. 89(4), pp. 2268-2271, 2001.
[102] R. B. Laghumavarapu, A. Moscho, A. Khoshakhlagh, M. El-Emawy, L. F. Lester, and D. L. Huffaker, *Appl. Phys. Lett.*, vol. 90, pp. 173125, 2007.
[103] A. Marti, A. Antolin, C. R. Stanley, C. D. Farmer, N. Lopez, P. Diaz, E. Canovas, P. G. Linares, and A. Luque, *Phys. Rev. Lett.*, vol. 97(24), pp. 247701, 2006.
[104] D. Bimberg, M. Grundmann, and N. N. Ledencov, *Quantum Dot Heterostructures*: John Wiley and Sons, 1999, pp. 338.
[105] H. J. Hovel, *Solar cells*, vol. 11. New York: Academic, 1975, pp. 166-174.
[106] A. Martí, N. López, E. Antolín, E. Cánovas, A. Luque, C. R. Stanley, C. D. Farmer, and P. Díaz, *Appl. Phys. Lett.*, vol. 90, pp. 233510, 2007.
[107] S. M. Sze, *Physics of Semiconductor Devices*, 2nd ed. New York: John Wiley & Sons, Inc., 1981.
[108] C. D. Cress, S. M. Hubbard, B. J. Landi, D. M. Wilt, and R. P. Raffaelle, *Appl. Phys. Lett.*, vol. 92, pp. 183108, 2007.
[109] D. Pons and J. Bourgoin, *Physical Review Letters*, vol. 47(18), pp. 1293, 1981.